KU LEUVEN

ARENBERG DOCTORAL SCHOOL
Faculty of Engineering Science

2D and 3D high-spatial and high-temporal resolution ultrasound imaging for characterization of tendon mechanics

An image registration approach

Catarina De Brito Carvalho

Supervisor:
Prof. dr. ir. P. Suetens
Prof. dr. ir. L. Scheys

Dissertation presented in partial
fulfillment of the requirements for the
degree of Doctor of Engineering
Science (PhD): Electrical Engineering

April 2017

2D and 3D high-spatial and high-temporal resolution ultrasound imaging for characterization of tendon mechanics

An image registration approach

Catarina DE BRITO CARVALHO

Examination committee:
Prof. dr. ir. H. Neuckermans, chair
Prof. dr. ir. P. Suetens, supervisor
Prof. dr. ir. L. Scheys, supervisor
Prof. dr. ir. F Maes
Prof. dr. ir. J D'hooge
Prof. dr. K Peers
Prof. H Screen
(Queen Mary University of London)
Dr. ir. P Slagmolen
(Materialise)

Dissertation presented in partial
fulfillment of the requirements for
the degree of Doctor of Engineering
Science (PhD): Electrical Engineering

April 2017

Uitgegeven in eigen beheer, Catarina De Brito Carvalho, Herestraat 49 box 7003, B-3000, B-3001 Leuven (Belgium)

Acknowledgements

Well... I don't even know where to begin... 4 and half years ago I started my quest after a much wanted dream of a PhD. Pieter, you were one of the one who believed in me and who gave me the opportunity to work in such a great topic, with such great colleagues. You were the one I could count on for help and to discuss new ideas. The work was not always how we imagined it, but we persevere and we kept going, advancing towards the final goal. Of course, there are things that could be better... but isn't there always?! After helping me with the beginning and the course of my PhD, you now came back into my PhD road as a jury member :). Thank you for everything.

Dear Professor Suetens, I would like to thank you for the opportunity of working with you. Your help in the decisive moments made possible to finish this PhD. Dear Lennart, thank you for your help at the last stage of my PhD. I've learned many things with you during this short period of time. Dear Professor Maes, despite not being my promotor, you always tried to help me as much as you could. Your reviews improved always the level of my work. Dear Professor Jan, it was a real pleasure to work with you. I always knew that I could count on you when I had some problem or to "talk about life", as you used to say :). Dear Professor Peers, thank you so much for being such a cool person. It was great to talk to you and to always have your support with the work we were doing. Dear Professor Screen, I would also like to thank you for being such an inspiration throughout my work. Your work with tendons was always inspiring and I've used it during my PhD as a guiding light.

I would also like to thank iMinds for funding my PhD during the first two years.

Stijn Bogaerts, thank you for your help with the clinical field, and thank you for your trust in my work. Your clinical perspective and your feedback was always of great value and contributed to improve my work. Thank you for your collaboration and for keeping using the KULTeC after I'm gone.

Thijs, you were one of the colleagues that gave me the most help at the beginning.

You were always there to share your "PhD-life" experience, you were there to tell me to relax and keep going, and you always had the time to sit with me and the tell me how great my work was (even when it wasn't ;)). Although you moved to Australia, your spectrum have always been around the Louvre and it seems that you "just left" ;).

Tom, you were the first one sitting next to me. Despite that, you were one of the last "new" colleagues to talk to me :). After the bumpy beginning, you were always a very good colleague, you were the registration expert I consulted with my questions, and you were the one that procrastinated, just like me, with the Arenberg Doctoral School paperwork and bureaucracy. You made time for my countless "the other day" stories and my "funny" (or maybe not so funny) jokes. It has been a pleasure the share the PhD road with you and I hope our paths will cross someday.

Daan, you were also on my "first island". You were always working so hard, but even then, when I would ask you something, you always found the time to help me. You were one of the few book-geeks in the Louvre and I really enjoyed discussing books with you. Your love for culture was also really interesting and it was a pleasure to have met you and work with you.

David, you were the one who was always trying to keep the group together, and do things together. You were the football and frisbee master and the organized colleague. You always had a strong opinion and you knew always so much about so many things that it was impressing.

Janaki, you were always the big and the master counselor for me and for everyone else. You always tried to use your experience and your knowledge to help everyone else. You are one of the kindest people in the Louvre and I'm really thankful for getting to know you. Thank you for always taking care of everyone.

After one year, new places were re-assigned and I've moved to my new and final island. Simon, Wouter, Anke, and Louise, dear friends, you were the island inhabitants which welcomed me into my new place. Simon, dear friend and colleague of jokes and pranks. You are one of the funniest people I've met in Belgium. Always happy and always laughing. The times that we shared in the island were the greatest and the funniest. It was so nice to get to work and chat with you about the most different things. Wouter, thank you for all the nice moments we shared and all the jokes. It was great being there while you finished your PhD and getting to know you better. You always had a nice word to say, a you had always showed interested in the work of your fellow inhabitants. Dear Anke, you are a greatest doctor of all the pains and all the complaints :). You had always so much patience for my "diseases" and I got from you one of the best advice ever: "Let's wait and see". Most of my complaints turned out to be just in my head or not serious. My hypochondriac side was always relaxed knowing that, if there was something wrong with me, you would come to help:). Now that I'm far away, I still keep your advice in my mind and I'm sure if I ever think I'm ill, I'm going to text you :). Dear Louise, thank you so much for everything. You were always there when things went wrong. You always encouraged me up and together we could ramble about our dislikes and frustrations. You are a great role model, both professionally and personally. You are a successful researcher, a great mother and an awesome plant-lady :).

Sometime after my arrival, you arrived as well Philip. It was great having discussions with you during lunch time. You always had a critical opinion, always had a different view on things and that was what made our lunches so much fun and interesting.

Dzemila, Dorothy and Jiarui, you came afterwards :). Dzemila, thank you for your "Italian way". It was great to have someone thinking differently and increasing the "foreigner" ratio :). Dorothy, I'm really happy for the chance of getting to know you. Despite you not being the "talker" type, I always admired you because you always made sure your opinions were heard and you joined in our crazy discussions :). It was a pleasure to be your colleague and friend. Jiarui, although we did not share much time together in the Louvre, I want to thank you your help with the statistical analysis and wish you the best of luck with your PhD.

Markus, you were the last to complete the team and you are actually a very nice German guy. Thank you for being always so relaxed and thank you for going with the flow of my crazy/weird chats. I've been very lucky to know you and to have you as a fellow "foreigner". Keep up cooking your awesome cookies and good luck to your new adventure as well.

To the colleagues that left us in the meanwhile I would like to tell you that each time any of you left, the lab felt more empty. Ineeee. I like you so much... You are such a great girl and such a great friend. One day you wrote "Catarina, never leave... Belgium needs girls like you..." . I have to say that I think you are a bit wrong. Belgium does not need girls like me because they have girls like YOU dear Ine. You were the happy face of the Louvre, you were the enthusiastic girl and you were the girl whom everyone liked. Thank you for sharing a few years with us and thank you for being such an awesome girl. Jasmien, it was always great to have you around and it was so much fun. Thank you for all your positive attitude :). Jonatan, thank you for your positivism as well. Your entrepreneurship is impressive and your adventurous side is fascinating. Jeronimo, what a colleague you are... At the beginning, I did not like you so much... but, after getting to know you, I can see that you are a concerned and caring friend. You have always looked out for me and you have always try to show me how important my work was. You were the person I would trust if I had any problem. Your compliments and support always made me feel better because, coming from you, it validated my work. Thank you for your honesty and thank you for your care.

Dorothée, you are a colleague that left us but I'll make a special paragraph for you :). First of all, I would like to confirm that "Dorothée is always right ;)". You were one of the coolest and funniest girl I had the luck to meet in Leuven. You are quirky and a bit weird, just like me. I remember we could be having a conversation and suddenly, out of nowhere, start singing; we could laugh of things no one else thought it was funny :), and we had a great time with dinosaurs' :). I have to say that if you would have to be a fruit, you would be a "fine-apple" :). I want to truly thank you for everything and to tell you that I miss having you around. I hope I am lucky enough to find a "Dorothée II" here in Porto... Charlotte, I'll include you in this special section as well because you were also a special friend. Since the moment you sat by my side, I knew we were going to be friends. You were this shy girl, trying to mind your own business and not interfering with the "ESAT-people". Gladly, you became one of "us" and since then you were a valuable asset of our group. Although not always present, your name was always in everybody's mind. Thank you for sitting next to me and giving me the chance of getting to know you.

Stijn de Buck, thank you for your words of wisdom and for our interesting discussions, in which we always stand on opposite sides ;). Dear Babs, thank you for your help during decisive moments. Your kindness to me was always heart-warming. Dominique, I believe I owe you a big thank you :). I know I gave you some headaches but I never intended to. Thank you so much for your help during my PhD. Without your, our group wound not be the same.

Dear Sofie, I don't want to finish without thanking you too. It was great to supervise your master thesis and to work with you. You are a great and smart girl and I wish you all the good luck in the world. Dear Hanne and Karlijn, I would also like to thank you for being such friendly girls and wish you all the best with your PhD's.

Dear cardiology and radiology colleagues, it was great to share the lab with you. One of the great sides of the Louvre is its multi-cultural and multi-disciplinary nature. Bidisha, Natalia, Natasha, Brecht, Pedro, João, Jurgen, Mahdi, thank you so much for your friendship, for the interesting discussions we always had in the kitchen and for your help with the ultrasound field. Pedro, um obrigado especial a ti pela tua simpatia e por seres um rapaz tão divertido. Obrigada pela ajuda e pelas nossas conversas :). Ahmad, thank you for teaching me Farsi :).

Susana, obrigada também por tudo. Conhecer-te foi das melhores coisas que me aconteceu em Leuven e o apoio que me deste foi incomparável. Eras a pessoa a quem podia confidenciar as minhas frustrações, a pessoa com quem podia reclamar acerca do resto do mundo, e a pessoa com experiência nesta coisa do doutoramento que me aconselhava. Os nossos cafezinhos de sábado eram como religião e os nossos jantares, sempre acompanhados com um bom vinho Português, passavam a correr. Foi óptimo ter partilhado estes anos contigo em Leuven. Obrigada :).

Last but not least, I would like to thank my family and David.

Querida mãe, querido pai e querido irmão, obrigada por tudo. A pessoa que sou hoje devo-o a vocês e o sucesso que atingi é tanto meu como vosso. Sei que foi complicado eu ter partido por tanto tempo, mas pude sempre contar com o vosso apoio. Mano, obrigada por "aguentares o barco" e por estares lá quando eu não pude.

David, OBRIGADA! Obrigada por estares lá nos bons e nos maus momentos, obrigada por me defenderes sempre e obrigada por quereres proteger-me de tudo e de todos. Obrigada também pelo teu interesse no meu trabalho, por me visitares em Leuven e por correres mundo para ires ter comigo. Nunca esquecerei o que fizeste por mim. Por fim, obrigada por teres tanto orgulho em mim. A conclusão deste doutoramento não teria sido possível sem ti. És um exemplo para mim e como tu dizes, "Pior que nunca ter conseguido, é nunca ter tentado". Nós conseguimos :).

As a concluding remark, this PhD would not have been possible without the collaboration, in so many different ways, of every one of you.

Thank you!

Abstract

Achilles tendinopathy affects competitive and recreational athletes as well as inactive people. The incidence of this pathology in the general population is 1.8‰and over 80% of tendon ruptures occur during recreational sports. The etiology of tendinopathies is multifactorial, but tendon overuse is assumed to be one of the main pathological stimuli.

Recently published studies have demonstrated the need for a better characterization of the tendon, more specifically, the local tendon mechanics. By performing this characterization in an accurate and reproducible manner, it is expected to understand better the mechanical behaviour of healthy tendons and, consequently, better understand the tendinopathy pathogenesis.

Nowadays, characterization of tendon mechanics is done by estimating the global tendon strain and the local tendon tissue displacement. Conventional ultrasonography ($\leqslant$ 10MHz) is the imaging modality used for this characterization due to its ubiquitous application for tendinopathy diagnosis and easy accessibility. However, it is believed that conventional ultrasonography is limited due to its low spatial and low temporal image resolution. Furthermore, the high-variability of tendon strain estimations reported in the literature are also assumed to be dependent on the imaging system used for the characterization of the tendon mechanics.

This work presented the investigation of the implementation of a 2D high-spatial and high-temporal resolution ultrasound acquisition system for the in-vivo characterization of tendon mechanics. Due to the novelty of this type of acquisition system for tendon strain estimations, a validation step was initially designed. For this validation, 2D global strain estimations were calculated using a developed affine image registration method. Good performance was obtained for this validation step, which allowed the validation of the image registration method as well as the validation of the novel high-spatial and high-temporal resolution ultrasound acquisition system. Afterwards, a 2D deformable image registration method was developed for the in-vivo characterization of the local tendon mechanics. Local tendon mechanics was evaluated by estimating regional tendon strain and local tendon tissue displacement. The developed deformable image registration method and the calculation of the features used for the characterization of the local tendon mechanics were embedded in the KULTeC. The KULTeC is a standalone, easy and intuitive application, which is intended to allow the clinician to easily characterized the local tendon mechanics. Due to the absence of ground-truth for the in-vivo data, a psychometric approach was performed. The obtained results confirmed the reproducibility of the implemented deformable image registration method, demonstrated a convergence of the estimated results with the literature results and demonstrated the capability of the method for the discrimination between asymptomatic and medium to severe tendinopathy conditions.

After the in-vivo characterization of the local tendon mechanics, the impact of out-of-plane motion was investigated. This type of artifact, which affects every 2D imaging modality, has frequently been pointed out as tendon strain estimation errors. For this investigation, 3D high-spatial resolution ultrasound data was used, and the global strain was estimated using an affine image registration approach. The results obtained from this experiment, using in-silico data, demonstrated the theoretically added value of strain estimations using 3D data. However, with the increasing complexity of in-vitro and ex-vivo data, and the increasing complexity of the acquisition setup, the acquisition of 3D high-spatial resolution US images becomes very challenging.

In conclusion, this work demonstrates the successful implementation of 2D high-spatial and high-temporal resolution ultrasonography system for in-vivo characterization of the local tendon mechanics. The *high-spatial* and *high-temporal* resolution provided by the used acquisition system together with the developed *deformable image registration* method have the potential of allowing better and more accurate in-vivo characterization of local tendon mechanics. Furthermore, the developed KULTeC application allows an easy and intuitive use of the developed image registration method in the clinical practice. The results obtained for 3D high-spatial resolution ultrasonography for global strain estimations show that this modality has the potential for elimination of out-of-plane motion but its application to real-world conditions is still technically challenging.

Beknopte samenvatting

Tendinopathie van de achillespees treft zowel niet-sporters als sporters, hetzij op recreatief niveau, hetzij op competitief niveau. Het komt dan ook voor bij 1.8% van de bevolking waarbzij zelfs meer dan 80% van de peesrupturen het gevolg zijn van recreatiesport. De oorsprong is multifactorieel, maar peesoverbelasting wordt beschouwd als een van de belangrijkste pathologische stimuli. Recent gepubliceerde studies hebben aangetoond dat er nood is aan betere inzicht in de mechanische eigenschappen van de pees, en meer specifiek hoe deze meer lokaal variëren over de pees heen. Door deze eigenschappen op een accurate en reproduceerbare manier te gaan documenteren, wordt verwacht een beter inzicht te krijgen in het (mechanisch) gedrag van gezonde pezen en bijgevolg ook in het onstaan van tendinopathie.

Momenteel wordt om de mechanische eigenschappen in kaart te brengen voornamelijk gebruik gemaakt van een schatting van de globale peesspanning en de lokale peesverplaatsing. De beeldvormingsmodaliteit die hiervoor primair wordt gebruikt is conventionele echografie (<= 10MHz) gezien het veelvuldig gebruik voor de diagnose van tendinopathie en de grote toegankelijkheid. Conventionele echografie heeft echter een beperkte resolutie in tijd en ruimte. Bovendien zou de hoge variabiliteit van de schatting van peesspanning reeds gerapporteerd in de literatuur afhankelijk zijn van de beeldvormingsmodaliteit die werd gebruikt voor de mechanische karakterisatie van de pees.

Daarom werd in dit onderzoeksproject een tweedimensionale (2D) echografie acquisitie systeem met hoge spatiale en temporele resolutie geïmplementeerd en toegapst voor de in-vivo karakterisering van peesmechanismen. Aangezien dit type van acquisitie systeem echter nooit eerder werd gebruikt voor de schatting van peesspanning, werd in eerste fase de validiteit van de ontwikkelde setup onderzocht. Hiervoor werd een schatting gemaakt van de 2D globale spanning aan de hand van een ontwikkelde niet-vervormbare beeldregistratie. Bevredigende resultaten van deze meting toonden de validiteit van zowel de beeldregistratie methode als het nieuwe echografie acquisitie systeem aan.

Vervolgens werd een 2D, vervormbare beeldregistratie methode ontwikkeld voor de in-vivo karakterisatie van lokale mechanische eigenschappen, i.e. de regionale peesspanning en de lokale weefselverplaatsing in de pees. De ontwikkelde 2D vervormbare beeldregistratie methode en de methodologie om op basis hiervan de mechanische parameters van de pees te definiëren werden gebundeld in KULTeC. KULTeC is een op zichzelf staand, intuïtieve en toegankelijke applicatie, bedoeld om de clinicus op een eenvoudige manier de lokale mechanische parameters van een pees te in kaart te brengen Wegens de afwezigheid van een gouden standaard voor de in-vivo data, werd voor de verdere validatie van KULTeC een psychometrische benadering gebruikt. De bekomen resultaten bevestigden niet alleen de reproduceerbaarheid van de geïmplementeerde vervormbare methode voor beeldregistratie, maar tevens de overeenkomst van de geschatte resultaten met resultaten eerder gerapporteerd in de literatuur. Tenslotte werden ook de mogelijkheden van de methode om te discrimineren tussen personen zonder, met matige, of met ernstige tendinopathie in kaart gebracht.

Na de in-vivo karakterisatie van de mechanische eigenschappen werd de impact van peesbeweging weg van het beeldvormingsvlak onderzocht. Dit type artefact, dat inherent elke 2D beeldvormingsmodaliteit beïnvloedt, wordt vaak aangeduid als een belangrijke oorzaak van foutief geschatte peesspanning. Voor dit luik van het onderzoek werd gebruik gemaakt van 3D echografie data met een hoge spatiale resolutie. De globale spanning werd vervolgens opnieuw geschat aan de hand van vervormbare beeldregistratie. Uitgevoerd op in-silico data, toonde dit experiment de theoretisch toegevoegde waarde aan van het gebruik van 3D data voor de schatting van spanning. Echter, wegens de sterk toenemende complexiteit van dergelijke acquisitie in een in-vitro of ex-vivo setting, kon deze specifieke validatie niet verder worden uitgebreid.

Tot besluit kan worden gesteld dat dit werk heeft geleid tot de succesvolle implementatie van een 2D echografie systeem met hoge spatiale en temporale resolutie, waarvan bovendien werd aangetoond dat het kan worden gebruikt voor de in-vivo karakterisatie van lokale mechanische peeseigenschappen. De hoge spatiale en temporale resolutie van het gebruikte acquisitie systeem, in combinatie met de ontwikkelde vervormbare beeldregistratie methode, zullen potentieel leiden tot een betere, meer accurate in-vivo karakterisatie van deze eigenschappen. Daarenboven kan deze karakterisatie, dankzij de ontwikkelde KULTeC applicatie en de hierin geïntegreerde beeldregistratie methode, op een gemakkelijke en intuïtieve manier worden uitgevoerd in de klinische praktijk. Tenslotte, tonen schattingen aan de hand van 3D echografie met hoge spatiale resolutie van globale spanningen aan dat deze modaliteit het potentieel heeft om beweging uit het vlak te elimineren. Echter, de toepassing hiervan in dagdagelijkse klinische condities vormt tot op heden nog een grote technische uitdaging.

Abbreviations

LG	Lateral-gastrocnemius subtendon
MG	Medial-gastrocnemius subtendon
SOL	Soleus subtendon
MRI	Magnetic resonance imaging
US	Ultrasound
2D	Two-dimensional
3D	Three-dimensional
RF	Radio-frequency
HST	High-spatial and -temporal
MAE	Mean absolute error
MRE	Mean relative error
MAD	Mean absolute deviation
NSE	Normalized squared error
KULTeC	KU Leuven Tendon Characterization application
ROI	Region of interest
PAS	Passive elongation
ISO	Isometric contraction
ICC	Intraclass correlation
ROC	Receiver-operating characteristic curve

C1	Less severe tendinopathy
C2	Medium severe tendinopathy
C3	Very severe tendinopathy

Contents

List of Figures

List of Tables

Chapter 1

Introduction

Contents

The clinical questions which motivated the work here presented were: **"How can we quantify the biomechanical properties of the Achilles tendon in-vivo?"**, **"How can we improve the performance of our method, in comparison with the state-of-the-art?"** and **"Are the obtained results clinically meaningful and can these be used for tendinopathy diagnosis?"**. By answering these questions, a better understanding of the

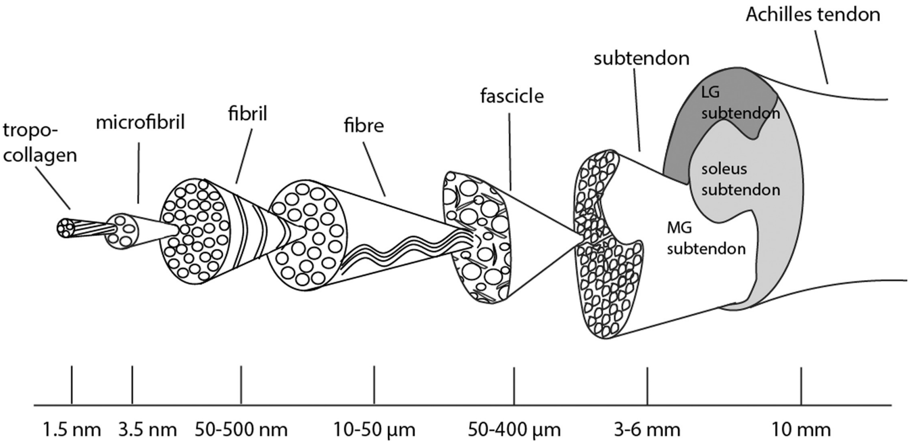

Figure 1.1: Proposed naming scheme of Achiles tendon hierarchy. MG, medial gastrocnemius; LG, lateral gastrocnemius (obtained copyright from [86]).

functional role of tendons would be gained, leading to a potential better understanding and characterization of the pathogenesis of tendons.

In this introductory chapter a description of the Achilles tendon, which was the studied specimen, is given followed by a description of the current insights and hypotheses on the motion and deformation patterns of this tendon. Afterwards, the different experimental setups and methodologies used to measure the biomechanical properties of the Achilles tendon are elaborated on, and the limitations and benefits of each approach are described. Finally, the thesis goal and the structure of the presented work are described.

1.1 Achilles tendon

Tendons are dense fibrous connective tissue and interpose muscles and bones. These structures are responsible for transmitting the force produced in the muscle to the bone allowing the joint motion [111].

The Achilles tendon is one of the most frequently injured tendons in the human body [103]. Because of the Achilles tendon's high injury risk, its large dimensions and its easy access for imaging purposes, this tendon is commonly used as study specimen for in-vivo tendon biomechanical characterization studies [225, 127, 8, 16, 137, 26, 57, 164, 196, 76, 167, 195, 81, 77, 38]. Likewise, the Achilles tendon is the studied specimen in this work.

The Achilles tendon (as well as all of the other tendons), is composed mainly of collagen and elastin molecules. By percentages, collagen accounts for 65% to 70% and elastin for approximately 2% of the dry mass of the tendon [110]. These two molecules, which are produced by the tenoblasts and tenocytes, are embedded in a proteoglycan-water matrix. Also, soluble tropocollagen (basic structural unit of collagen) molecules form cross-links that aggregate progressively in collagen fibrils [111] which are consequently organized in a complex hierarchical scheme to form the tendon.

Over the past decades, research focused on the characterization of tendon biomechanics has increased. The increased interest in tendon biomechanics characterization has led to the unraveling of the complex hierarchical structure of tendons and the possible variations of this structure to meet different functional needs. However, this increased interest has also led to the use of inconsistent nomenclature to describe identical tendon structures. Therefore, Handsfield *et al.* [86] proposed a size-based naming, rooted in the work of Kastelic *et al.* [113], for the definition of tendon hierarchies as represented in Fig. 1.1.

According to the work of Handsfield *et al.* [86], the aggregation of tropocollagen molecules makes microfibrils (with diameter around 3.5 nm), which in turn aggregate into collagen fibrils [171]. Collagen fibrils are considered the fundamental building block for different connective tissues, with diameters ranging from 50-500 nm. A group of collagen fibrils forms then *tendon fibers*, which, in turn, form *tendon fascicles*. The latter has a diameter ranging from 50-400 µm and are visible to the eye. The same work also proposes a special naming for the macro-scale hierarchical level observed in tendons that are shared between multiple muscles. For such special tendons, the term *subtendon* is suggested to represent a structure which is part of the whole tendon, but is originated and transmits force from a distinct muscle belly (e.g. medial gastrocnemius subtendon).

The Achilles tendon is an example of a multi-muscle tendon. This tendon is composed of different subtendons: the lateral-gastrocnemius (LG) subtendon, the medial-gastrocnemius (MG) subtendon and the soleus subtendon, as depicted in Fig. 1.1.

Besides the discrimination of the Achilles tendon according to the three different subtendons, this tendon can also be divided into aponeuroses and free Achilles tendon. Aponeuroses are extremely delicate, thin sheath-like structures which commonly attach muscles to bones. However, in the case of the Achilles tendon, the gastrocnemius and the soleus aponeuroses originate from the gastrocnemius and soleus muscles, respectively, and join to merge the free Achilles tendon. The free Achilles tendon is then defined between the soleus myotendinous junction (location where the soleus muscle meets the tendon), and the calcaneus. Figure

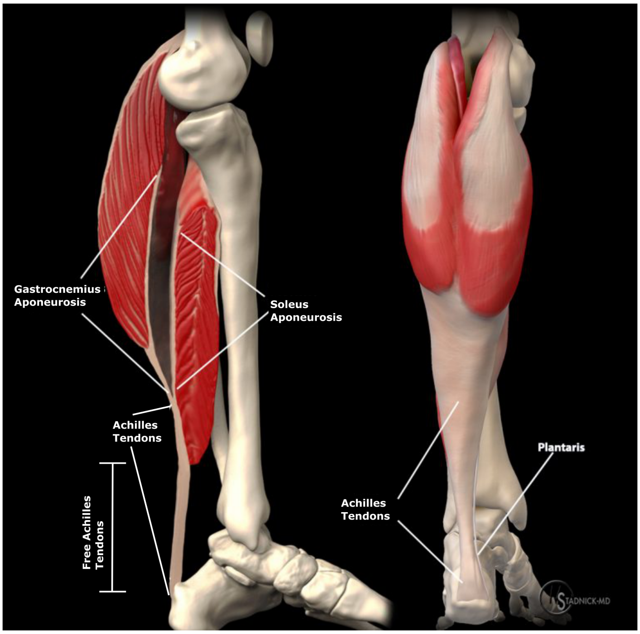

Figure 1.2: Soleus and gastrocnemius aponeurosis (flattened portions of the Achilles tendon) and free Achilles tendon. (adapted from [202]).

1.2 illustrates the two aponeurotic regions of the Achilles tendon and the free Achilles tendon.

Figure 1.2 and Fig. 1.3 show two types of aponeuroses of the Achilles tendon. The medial gastrocnemius aponeurosis, which joins the tendon at the gastrocnemius myotendinous junction (GM MTJ), and the soleus aponeurosis, which joins the tendon at the myotendinous junction of the soleus (MTJ SOL).

Structurally, it is believed that the subtendons of the Achilles tendon undergo a "twisting effect" which was primarily reported by Parson *et al.* [131] in 1894. More recently, it has been reported that although the subtendons join to form the Achilles tendon, tissue bundles originating from each of these subtendons can still be distinguished at the insertion of the free Achilles tendon in the calcaneus bone [40, 60, 207].

Considering this novel possibility for the discrimination between the three subtendons, the longitudinal rotation of the Achilles tendon has been re-examined. It has then been hypothesized that each subtendon undergoes rotation, from proximal to distal, such that the Achilles tendon of the right

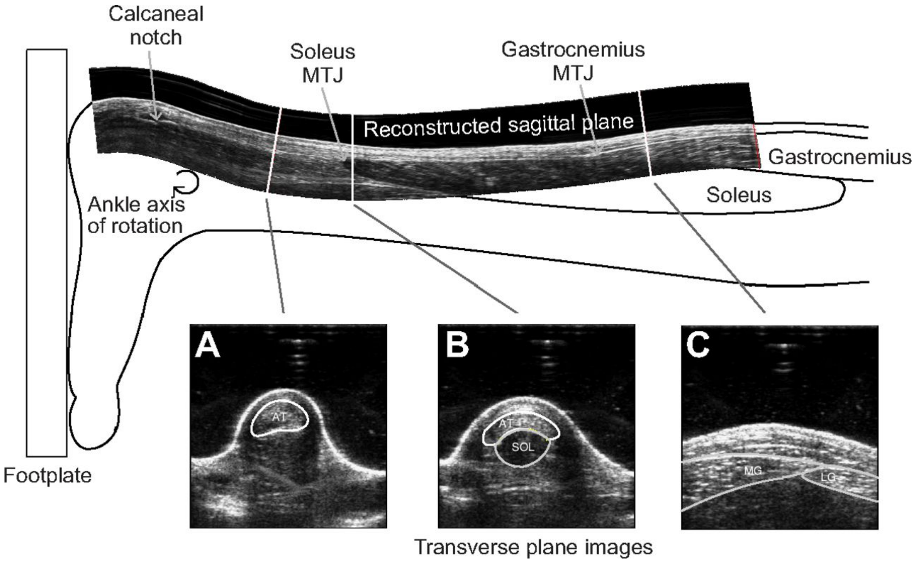

Figure 1.3: Re-constructed sagittal view of the triceps surae muscle–tendon unit. The Achilles tendon (AT) area is outlined in A and B, while the soleus (SOL), medial gastrocnemius (MG) and lateral gastrocnemius (LG) are outlined in B and C. MTJ, Muscle–tendon junction. (reproduced from Lichtwark *et al.* [140]).

leg suffers a counter clockwise rotation, while the Achilles tendon of the left leg suffers a clockwise rotation [40, 60, 207]. The degree of this rotation is difficult to quantify and large inter-individual variations have been reported. Rotation degrees between 10° and 150° have been identified [60] and depending on the degree of the rotation, the insertion of the subtendon can change both anteroposteriorly and lateromedialy. Figure 1.4 suggests a representation of the type of subtendon rotation found in 43% of 110 cadaver legs examined by Edama *et al.* [60].

The functional role of this tendon rotation remains unknown but some authors have suggested that this rotation may attribute ropelike properties to the Achilles tendon which would enhance its ability to strain and store energy [23, 132]. An alternative explanation is that a tendon that rotates is able to equalize force-length properties by optimizing contractile ability. It is then hypothesized that if this equalization of the force-length would not occur, a suboptimal force would be produced due to the differences of fiber length through the joint range of motion [54].

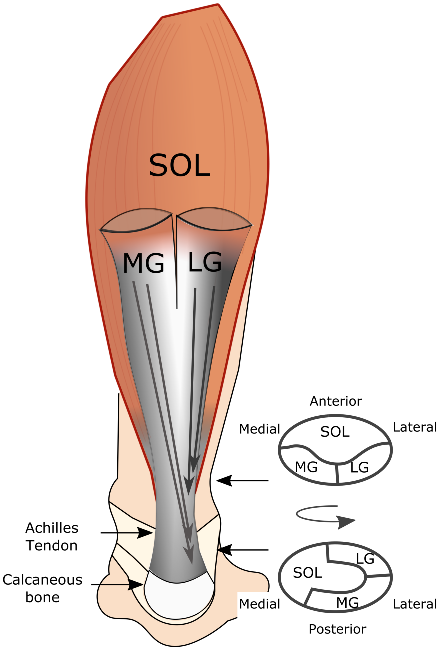

Figure 1.4: Posterior view of the right leg triceps surae muscle tendon unit and the Achilles tendon insertion on the calcaneal bone. This type of conformation was representative of 43% of the 110 examined cadaver legs [60]. Arrows demonstrate that tendon fascicles that originate from the medial gastrocnemius insert on the posterolateral side of the calcaneus, whereas fascicles from the lateral gastrocnemius insert on the lateral-anterior aspect of the tendon. The rotation arrow demonstrates the counterclockwise rotation the tendon of the right leg undergoes. Oval schemes represent two cross-sections of the free Achilles tendon at a proximal site and above the calcaneal insertion. SOL, soleus; MG, medial gastrocnemius; LG, lateral gastrocnemius (adapted from [24]).

1.2 Biomechanics of asymptomatic Achilles tendons

Tendons are responsible for the force transmission between muscle and bone, enabling in this way skeletal movement. In addition, tendons are also important for the dynamics of movement coordination as they store and release elastic energy, protect muscle fibers from damage and enhance muscle performance [4, 3, 84, 99, 190, 142, 46].

However, these structures do not behave as rigid links, but exhibit a viscoelastic behavior, which is believed to be one of the key factors for a tendon to fulfill its roles [194].

The biomechanical properties of the Achilles tendon have been investigated using different setups and quantified in either a global or local manner. In this work, global quantification of the biomechanical properties of the Achilles tendon refer to the biomechacical properties estimated in the whole tendon while local quantifications refer to the biomechanical properties of the Achilles tendon which are evaluated at subregions of the tendon.

The following subsections describe the current insights and hypotheses on tendon motion and deformation patterns according to the different setups used, and the different scales of analysis. The first subsection describes the current insight and hypothesis for the global biomechanical properties of isolated tendons, both at a macroscopic and at a microscopic scale; the second subsection describes the current insight on the global biomechanical properties of the in-vivo Achilles tendons; while the third subsection describes the main findings for the biomechanical properties of the free-Achilles tendon.

1.2.1 Biomechanical properties of isolated tendons

Traditionally, the biomechanical properties of tendons have been studied using methodologies involving stretching of isolated tendons to failure. The outcome of this type of test can then be evaluated both at macroscopical or microscopical scale.

In the next sections, the main findings of the investigation of the biomechanical properties of the Achilles tendon at macroscopical and microscopical scale are described.

Macroscopical analysis

Tensile tests are commonly used to investigate the biomechanical properties of tendons. Stress-strain curves, as the one presented in Fig. 1.5, are tools commonly used to evaluate the biomechanical properties of isolated tendons. A tendon stress-strain curve represents the intrinsic material properties of the tendon and can be subdivided into three regions. The first is the toe region and has non-linear deformation. This region is associated with the un-crimping of

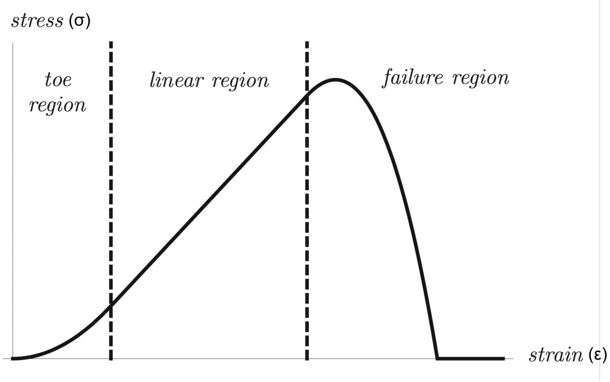

Figure 1.5: Stress–strain curve of a tendon showing three distinct regions (toe, linear and partial failure) before complete rupture (adapted from Rees *et al.* [183]).

the collagen fibers [222]. Beyond that region, the tendon experiences a linear deformation region, which has been defined to exist between 2% strain and 6% or even 8% strain [20, 158, 155]. Afterwards, there are the partial and complete failure region at 10%-15% strain [20].

In this type of curve, the slope of the curve in the linear region corresponds to the Young's modulus and it has been reported to range between 1-2 GPa [29, 20, 192, 180]. Ultimate tendon stress, in isolated tendon tensile tests, has been reported to be $\approx$ 100MPa, and ultimate tendon strain (i.e. strain at failure), has been reported to range between 4-10% in humans [29, 175, 63, 192].

Besides the stress-strain curves, other biomechanical properties of tendons can also be investigated using uniaxial tensile tests.

When a tendon is stretched, it does not behave perfectly elastic due to its viscoelastic properties. Given the time-dependent properties of the collagen fibers and proteoglycan matrix [41, 97], tendons exhibit force-relaxation, creep and mechanical hysteresis. Force-relaxation means that the force required to deform the tendon to a certain length decreases over time (Fig. 1.6(a)). Creep occurs when persistent constant force is applied, resulting in elongations which increase over time (Fig. 1.6(b)). Lastly, mechanical hysteresis is demonstrated by a loop of the force-elongation plots during loading and unloading of the tendon (Fig. 1.6(c)). The area of the loop represents the amount of elastic strain energy lost as heat in the stretch-recoil cycle. The average mechanical hysteresis value for isolated tendons, reported in the literature is $\approx$ 10% of the total work done on the tendon during stretching [20, 192, 180, 48, 116]. However, these

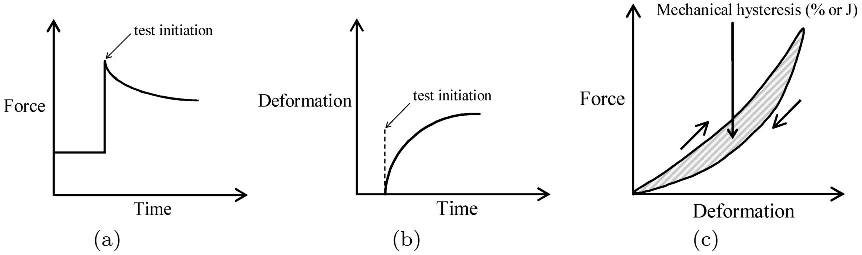

Figure 1.6: Force-relaxation (a), creep (b) and mechanical hysteresis (c) tests. In (c), the two arrows indicate loading and unloading directions. (obtained copyright from Maganaris *et al.* [152])

values are obtained after a few stretch-recoil cycles. This initial step is required because in the first few cycles, the tendon does not recover its original length. This phenomenon is referred to as tendon "conditioning" and it was initially believed to be an artifact caused by the improper fixation of the tendon during the tensile test [116], and afterwards demonstrated to also occur in in-vivo situations [150, 151].

Microscopical analysis

Besides the analysis of the biomechanical properties of tendons at macroscopical scale, also the biomechanical properties of tendons at microscopical scale can be evaluated. Due to the microscopical nature of this analysis, the quantification of the tendon strain is performed by mounting the studied specimen (commonly rat tail fascicles) on an uniaxial tensile test device, and confocal microscopy is the commonly used imaging modality for the acquisition of these images.

The importance of evaluating the biomechanical properties of tendons at microscopical level has been demonstrated by Screen *et al.* [191], Cheng *et al.* [33], Szczesny *et al.* [208], and Thorpe *et al* [211, 210, 209]. Screen *et al.* [191] reported that local strain within the fascicles was much smaller than the applied global strain. In this study, Screen *et al.* reported also an increase of sliding between the adjacent collagen fibers with the increase of global strain. Cheng *et al.* [33] also demonstrated an inhomogeneous strain response throughout the proteoglycan-water matrix together with a large strain variability between samples. In this work, Cheng *et al.* quantified local strains much lower than the applied gross strain, which is in line with the results found by Screen *et al.* [191]. Furthermore, large compressive strains, perpendicular to the major deformation axis, were also found and a Poisson's ration of 0.8 was measured. Finally, this work hypothesized as well the occurrence of sliding between fascicles and rotation at the level of the matrix.

Interestingly, and in line with the findings of Cheng *et al.* [33], Szczesny *et al.* [208] hypothesized that the external load applied to rat tail fascicles was transmitted through shear stresses which acted at the fiber-matrix interface. These authors suggested that collagen fibrils in tendons were loaded via interfibrillar shear, which is produced by the relative sliding of fibrils and that an increased interfibrillar sliding reduced the amount of strain that was transmitted to the fibrils, leading to a lowering of the macroscopic tensile modulus.

Lastly, Thorpe *et al.* [209] also investigated the microscopical deformation of isolated tendons and found a reduction of sliding, at the fascicle level, with the increase of age (in horse models). This reduction of inter-fascicle sliding was hypothesized to arise from the proliferation of collagen cross-linking and inter-fascicle adhesion.

1.2.2 Biomechanical properties of in-vivo Achilles musculo-tendinous unit

As mentioned above, the tendon stress-strain curves are important to characterize the tendon biomechanical properties. However, caution should be taken when inferring results from isolated tendons to in-vivo function. This caution is warranted because: linear region of in-vivo conditions may not be similar to isolated conditions; fixation of isolated tendons could suffer from slippage artifacts or it can be associated with un-physiological stress distributions [116]; and the common preservation of isolated tendons prior to the study may alter their biomechanical properties [157, 198].

Examples of differences between the hysteresis of the Achilles tendon estimated in-vivo and in isolated tendons have been reported in the literature. Hysteresis of isolated tendons has been shown to range between 5%-10% [116, 62, 220, 185]. Interestingly, the in-vivo hysteresis of the Achilles tendon has been reported to be small (7%) in the free Achilles tendon [220] while the hysteresis reported for the aponeurosis of the medial and lateral gastrocnemius has been reported to be much higher (24%) [66, 219, 141].

Another example of the different types of results obtained for the biomechanical characterization of isolated tendons versus in-vivo tendons was presented by Peltonen *et al.* [177]. These authors investigated the force-elongation characteristics of 14 subjects at different loading rates using ultrasound imaging.

The Achilles tendon stiffness and elongation were evaluated at 80% of maximum voluntary contraction during a ramping period of 1 second and 7 seconds. In the end, they concluded that no significant differences were obtained for either stiffness and elongation between the fast and slow loading rates. Furthermore, they also reported a hysteresis of 5% ± 2% which is within the lower range of the hysteresis reported in the literature for isolated tendons. Besides these differences, this study hypothesized as well that both the independence between stiffness and loading rate and the small hysteresis estimated, demonstrated a prevalence of elastic over viscous properties for the in-vivo Achilles tendon.

The estimation of different viscoelastic behavior of isolated and in-vivo tendons presented above gives an insight into the reasons why the biomechanical properties of the Achilles tendon should not be inferred from isolated tendon tests towards in-vivo conditions. In light of this, several studies proposed the investigation of the biomechanical properties of the Achilles tendon, as a whole, in vivo. This quantification is commonly performed using either magnetic resonance imaging or ultrasound imaging and a manual tracking of anatomical landmarks, such as the GM MTJ and SOL MTJ, is performed for the quantification of the elongation of the musculotendinous unit.

However, the investigation of the biomechanical properties of the musculotendinous unit is only valid and clinically relevant if the deformation of the aponeuroses and the free Achilles tendon are uniform.

In light of this, several studies investigated the assumption of uniform deformation between aponeuroses and free Achilles tendon and contradicting results were found. Arampatzis *et al.* [9] reported more elongation of the aponeurosis region, in comparison with the free Achilles tendon, while no significant difference was obtained for strain estimations of these two regions. Also Muramatsu *et al.* [161] found no significant difference between the strain at the MG aponeurosis and free Achilles tendon. Both performed this biomechanical analysis during maximal isometric plantar flexion. Contrarily, Magnusson *et al.* [155] reported larger elongation of the free Achilles tendon compared to the MG aponeurosis region, and significant differences were found between the strain of the free Achilles tendon (8.0% ± 1.2%) versus the MG aponeurosis region (1.4% ± 0.4%), during maximal isometric plantar flexion. Similarly, Iwanuma *et al.* [100] reported a free Achilles tendon strain (3.3%±1.5%) larger than the aponeurosis strain (1.6%±1.1%) during submaximal isometric plantar flexion. Lastly, Farris *et al.* [65] reported significantly larger strain of the free Achilles tendon (5.2%±1.7%) than of the aponeurosis (2.6%±2.0%). Interestingly, these authors hypothesized that the smaller strain obtained on the aponeurosis regions was caused by the considerable transversal strain this region presented (5.2%±4%) likely caused by the bulging of the triceps surae muscles upon contraction [65].

Another interesting result, which demonstrates another extent of the non-uniform elongation of the Achilles tendon was reported by Finni *et al.* and Lee *et al.* [73, 134]. These authors divided the aponeurosis region in two smaller regions (proximal region and distal region) and found that the proximal region of the aponeurosis stretched while the distal region of the aponeurosis shortened.

Besides the different strain distribution from proximal to distal regions of the aponeurosis, also differences in strain distribution when applying different force distributions between the three portions of the triceps surae muscles were investigated. Lersch *et al.* [137] found that changes in the force distribution within the triceps surae muscle resulted in strain differences up to 2.5%. These authors reported also that, overall, the strain between the proximal/distal mid-line (narrowest region) of the free Achilles and the calcaneal insertion exceeded the strain estimated between the SOL MTJ and the proximal/distal mid-line of the free Achilles tendon in every muscle variation tested. Another important finding of this work was that, in the proximal tendon aspect (SOL MTJ to proximal/distal mid-line free Achilles), strain on the lateral side was larger than strain on the medial side. Interestingly, the opposite occurred in the distal tendon aspect, where the strain on the medial side exceeded the strain estimated on the lateral side. These results are indicative of the possible rotation of the tendon which can also result in strain shearing effects.

Lastly, the influence of the knee position on non-uniform elongation of the Achilles tendon, was also investigated. Bojsen-Moller *et al.* [23] demonstrated that during maximal isometric contraction with the knee maximally extended, the displacement of the GM MTJ was larger than the SOL MTJ. Alternatively, during maximal isometric contraction with the knee maximally flexed (125°), the displacement of the SOL MTJ was larger than the one of the MG MTJ. Figure 1.7 illustrates the hypothesized uneven activation of soleus and medial gastrocnemius during maximal isometric contraction with knee maximally extended.

1.2.3 Biomechanical properties of in-vivo free Achilles tendon

Given all these conflicting results, but largely demonstrated non-uniform elongation patterns between the aponeurosis and the free Achilles tendon, the quantification of biomechanical properties of the global musculotendinous unit has very limited value. Instead, characterization of the biomechanical properties of the separate structures of the musculotendinous unit is assumed to yield better understanding of the functional role of each. In this manner, this work focuses on the quantification of the biomechanical properties of the free Achilles tendon.

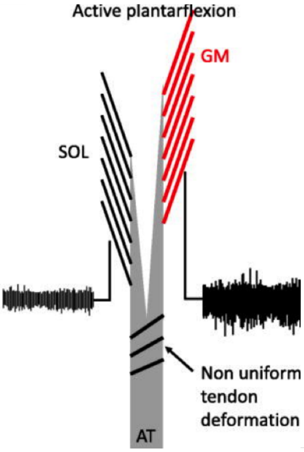

Figure 1.7: Uneven activation of soleus and medial gastrocnemius during maximal isometric contraction with knee maximally extended. SOL, soleus; GM, medial gastrocnemius; GL, lateral gastrocnemius; AT, Achilles tendon. (obtained copyright from Bojsen-Møller *et al.* [24])

Regarding the quantification of the biomechanical properties of the free Achilles tendon, the most relevant literature is the one of the group of Arndt *et al.* and Fröberg *et al.* [12, 80], the group of Slane *et al.* and Franz *et al.* [35, 196, 75, 197, 77], and the work of Lyman *et al.* [146]. All of these studies, but the one of Lyman *et al.*, used ultrasound imaging for the quantification of the biomechanical properties of the free Achilles tendon. Arndt *et al.* was the first to report non-uniform tissue displacement of the different layers of the free Achilles tendon. In this work, Arndt *et al.* found significant differences of the tendon tissue displacement between superficial, medial and deep layers (posterior-anterior), where the deep layer presented the largest tissue displacement. Afterwards, Slane *et al.* and Franz *et al.* [35, 196, 75, 197, 77] reported similar significant differences for tissue displacement estimations between the deep and superficial layer of the tendon of young volunteers, with the greater movement occurring in the deep layer. This research was then extended by the same group, and smaller differences of tissue displacements between superficial and deep regions were found for older tendons, in comparison with young tendons [77, 195]. Both Franz *et al.* and Slane *et al.* hypothesized that the load sharing at the multi-muscle level can be age dependent, resulting in such reduction of inter-fascicle tissue displacement. Slane *et al.* [195] also found that middle-aged tendons presented larger tendon tissue displacements which can be associated with an increase of the tendon compliance. As for the work of Lyman *et al.* [146], strain was measured in cadaveric legs using actuators, while the foot was moved into dorsiflexion. The main findings reported from this study was that the largest strain was obtained in the anterior side of the free Achilles tendon. However, during this dorsiflexion movement, the posterior sites of the tendon presented a significant increase of strain while the anterior did not present significant differences but a trend towards decreasing strain.

Given the findings describing non-uniform tendon tissue displacement, Bojsen-Møller *et al.* [23, 24] investigated the hypothesis of asymmetric loading and heterogeneous elongation of the Achilles tendon. In this work, Bojsen-Møller *et al.* hypothesized that the heterogeneous elongation of the Achilles tendon may be related to its anatomical design (rotation of subtendons towards the tendon insertion), different force-bearing properties of the different structures and regions of the Achilles tendon, and by a heterogeneous neural activation of muscles.

The biomechanical properties of the free Achilles tendon have also been investigated using shear wave elastography. Slane *et al.* [195] investigated the average shear wave speed on the free Achilles tendon of both young and middle aged adults, at three different regions and at two different ankle positions. The obtained results for both age groups showed that the wave speed decreased proximally, with the lowest speed being measured in the gastrocnemius aponeurosis. Besides, an increase of wave speed during passive dorsiflexion was observed, leading to the hypothesis of correlation between the strain-stiffening behavior of tendons.

Similar results were obtained by Aubry *et al.* [19], which showed a significantly increase in the average speed of the shear waves during the passive dorsiflexion of the tendon.

Besides ex-vivo and in-vivo experiments, Handsfield *et al.* [85] constructed a mathematical model which aims to modulate the non-uniform behavior of the Achilles tendon. These authors proposed a model for the 3D elongation of the Achilles tendon which incorporated structural information retrieved from MRI data and biomechanical information retrieved from the work of Slane *et al.* [196] and Arndt *et al.* [12]. The main finding of this work was that the sliding effect and the differential muscle forces were the main responsible (96% and 85% respectively) for the non-uniform elongation of the tendon. On the other hand, the tendon twisting effect and the retrocalcaneal insertion were only responsible for 35% and 3%, respectively, of the non-uniform elongation of the Achilles tendon. Nonetheless and due to the typical nature of modelling studies, some care should be taken when evaluating the presented results. Firstly, the triceps surae muscle forces were estimated by tuning the force boundary conditions used in this model, so that the displacement profiles observed by Slane *et al.* [196] would be obtained. The limitation of this fine-tuning lays on the fact that

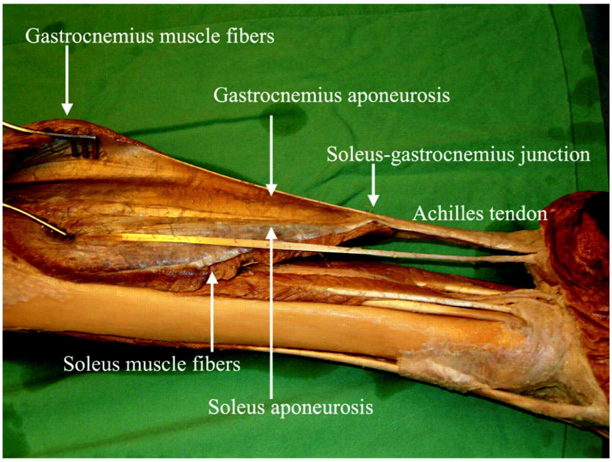

Figure 1.8: Medial view of a cadaver dissection of the lower leg, illustrating the most common type of junction between the gastrocnemius and soleus muscles (obtained copyright from Bojsen-Møller *et al.* [24])

the pattern of deformation and its magnitude have not yet been completely demonstrated in a large population sample and the representative power of this study may be limited. Moreover, these authors reported that by applying the tuning of the forces to obtain the specific displacement pattern, the constructed model was not sensitive to the specific material stiffness intended for this study.

1.2.4 Summary

The approaches used for the quantification of the biomechanical properties of the Achilles tendon are not consensual and the results obtained are even conflicting in some cases. Considering the merging of the gastrocnemius into the gastrocnemius aponeurosis, it seems logical to assume that the deformation of the gastrocnemius aponeurosis is mainly influenced by the mechanical work performed by the gastrocnemius muscle. Similarly, the same also seems logical to occur in the soleus aponeurosis. Considering the independent origin and insertion site of both gastrocnemius and soleus muscles, their different architecture (gastrocnemius is biarticular and the soleus is uniarticular) and their hypothesized different functional role [136], it seems reasonable to assume that both structures present different types of deformation. Moreover, it seems also plausible to assume that the merging of tissues which suffer different deformations into the free Achilles tendon may lead to deformation patterns different than the ones seen in the two separate aponeuroses. As for the differences within the aponeurosis structure, the variability found between proximal and distal regions can be due to the varying width of these structures (as represented in Fig. 1.8), from proximal to distal, which can lead to different stress distributions. Regarding these differences, Finni *et al.* [73] suggested also that these could arise from complex force transmission via intramuscular connective tissue, which could be a sign of compartmentalized recruitment of the muscle tissue.

Evidence of non-uniform deformation within the Achilles tendon has then been reported by the group of Arndt *et al.* and Fröberg *et al.* [12, 80], the group of Slane *et al.* and Franz *et al.* [35, 196, 75, 197, 77], and the work of Lyman *et al.* [146]. In summary, both the group of Arndt *et al.* and Fröberg *et al.* [12, 80], and the group of Slane *et al.* and Franz *et al.* [35, 196, 75, 197, 77] reported larger tissue displacement of the Achilles tendon at its deep layer and the smaller tissue displacement at the superficial region. Lyman *et al.* [146] reported also larger strain in the deep layer of the free Achilles tendon, but a significant increase of strain in the superficial layer of the tendon during dorsiflexion movements. One of the possible reasons for such non-uniform distribution of the tendon tissue displacement from superficial to deep layers of the tendon may be the different rotation of the medial and lateral gastrocnemius as well as the influence of the soleus muscle.

This quantification becomes even more challenging because the non-uniform deformation of tendons has also been reported at a microscopical scale. In these studies, the increasing of the applied global strain has been demonstrated to lead to an increasing of the sliding between the collagen fibers and to a non-uniform distribution of strain on the proteoglycan-water matrix [191, 33].

As these results demonstrate, the sliding effect, both at a macroscopical scale as well as at a microscopical scale, seems to have a ruling effect on the deformation patterns of the Achilles tendon. Interestingly, both Thorpe *et al.* [209], Franz *et al.* [76, 75] and Slane *et al.* [195] reported a reduction of the fascicle sliding, at microscopical level, and subtendon sliding, at a macroscopical level, as consequence of aging. Additionally, tendinopathy is known to increase in older adult athletes [109]. Combining these two findings, it is then feasible to hypothesize that a reduction of sliding is related with the pathogenesis of Achilles tendinopathy.

In conclusion, and despite being the largest tendon of the human body, the functional role of the Achilles tendon is still poorly understood and more investigation is warranted.

1.3 Achilles tendinopathy

Achilles tendinopathy has a clear effect on the performance of athletes representing a lifetime risk of 52% for elite long-runners and a yearly risk of 7-9% for top-level runners [107, 147, 128]. For recreational athletes, a cohort study of 725 males showed a tendinopathy incidence of 7.4% sustained shortly after or during a marathon [215]. Although less documented, the incidence of Achilles tendinopathy in the general population was reported as being 1.8‰[52].

Many terms have been used to describe Achilles tendon disorders. Although the aetiology of this disease remains unclear, tendinopathies have been linked to overuse, poor vascularity, lack of flexibility, genetic make-up, gender, and endocrine or metabolic factors [118]. Despite the multi-factorial nature of tendinopathies, *overuse* is pointed, by the majority of the literature, as being the main pathological stimulus [117, 42, 149, 14, 43, 16, 173].

Patients with tendinopathy present with activity related pain, localized tenderness upon palpation, swelling (diffused or localized) and reduction in function of the tendon [117, 42, 149, 14, 43, 16, 173].

Damage to the tendon can occur if microtrauma from repetitive and overuse tasks is produced and insufficient time is given for the repair process [122]. It has also been hypothesized that non-uniform strain distribution within the Achilles tendon can lead to microtrauma which can lead, in turn, to abnormal concentrations of load within the tendon, frictional forces or even localized damage to the fibers [13].

As explained above, tendinopathies have been correlated with repetitive loading exercises [117, 42, 149, 14, 43, 16, 173]. In line with this association, Magnusson *et al.* [173] presented a study where the pathogenesis of tendinopathy was associated with the mechanical loading of the tendon. This study showed that the mechanical loading of tendons results in an acute increase in collagen expression and increased collagen synthesis. It was also hypothesized that such elevated collagen expression was regulated by the strain transmitted to the tenoblasts. Alternatively, the degradation of collagen also increases in response to exercise [129]. Figure 1.9(a) depicts a schematic representation of the collagen synthesis and degradation after acute exercise. In the same figure, a net loss of collagen over the first 24–36h is observed, which is contradicted by a positive net synthesis 36–72h after exercise.

The results obtained by Magnusson *et al.* indicate that a recovery period is required to a net increase of collagen. This study showed also that without sufficient rest, a continuous loss of collagen is likely to occur, which can produce a more vulnerable tendon, which can possibly lead to the development of

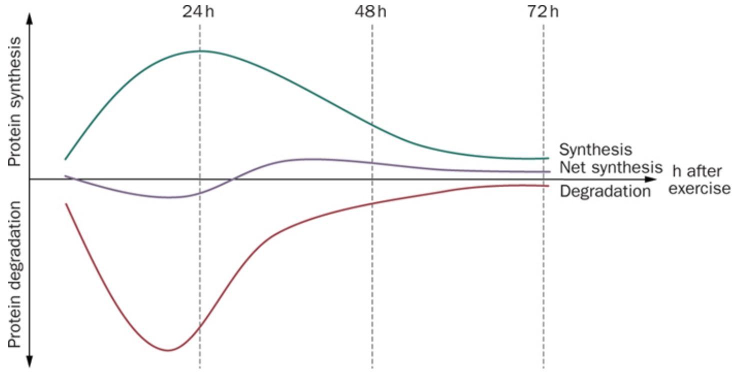

(a)

Figure 1.9: Acute exercise in humans is followed by an increase in both the synthesis and degradation of collagen (obtained copyright from Magnusson *et al.* [173])

tendinopathies [173, 129, 159].

Besides repetitive tendon loading, aging is also believed to promote tendinopathy [91, 162].

As briefly explained above, Thorpe *et al.* [209] investigated the local deformation of isolated tendons and found a reduction of sliding, at the fascicle level, with increasing age (in horse models). This reduction of inter-fascicle sliding was hypothesized to be related with aging and to arise from the proliferation of collagen cross-linking and inter-fascicle adhesion. This theory was then strengthened by the work of Franz *et al.* [76, 75] where the effects of aging in tendons were investigated during walking exercises. In this study, Franz *et al.* showed that old tendons present smaller differences of tendon tissue displacement between deep and superficial layers when compared with young volunteers. These two studies hypothesized that the increased cross-linking and adhesion between tendon fascicles can be responsible for the loss of independence between the three different Achilles subtendons which can, consequently, result in a different pattern of deformation and it can also lead to improper strain distribution within the tendon [76, 75].

Aubry *et al.* [18] investigated the viscoelastic properties of asymptomatic and symptomatic Achilles tendons by means of shear wave elastography. The main findings of this study were that significantly lower mean velocity was shown in tendons with tendinopathy than in normal tendons. Furthermore, it was also hypothesized that tendon softening was a sign of tendinopathy. Interestingly, this reduced shear wave speed of symptomatic tendons is in line with the results obtained by Slane *et al.* [195] for the middle-aged volunteers.

In conclusion the current insights and hypotheses on the biomechanical properties of symptomatic Achilles tendon seem to point to a tendon with softer constitution, which can also be caused by chronic degeneration, and a reduction of subtendon and fascicle sliding.

1.4 Quantification of Achilles tendon biomechanics

After an in-depth description of the current hypothesis on tendon motion and deformation patterns, it is important to describe the different experimental protocols used to measure the biomechanical properties of the tendon. As before, this section is divided into the methods used for the quantification of the biomechanical properties of: isolated tendons, the musculotendinous Achilles unit; and the free Achilles tendon.

1.4.1 Quantification of the biomechanical properties of isolated tendons

As shortly explained before, the most common approach used for the quantification of the biomechanical properties of isolated Achilles tendons makes use of uniaxial tensile testing devices. In this type of analysis, the tendon is mounted on a tensile tensing machine and elongated, at a particular rate. The changes in force and cross-head position of the tensile machine are measured.

The deformation that isolated tendons undergo during tensile tests can be evaluated both at macroscopical and at microscopical scale. In this way, depending on the chosen scale, different types of deformations are expected and both are illustrated in the following sections.

Macroscopical analysis

Macroscopical analysis of isolated tendon deformations using tensile tests can be performed by investigating the force/elongation curve or stress/strain curve of the material. Force/elongation curves are obtained by plotting the force against elongation (obtained from the cross-head position). Due to the dependency of the elongation/force curve with the dimensions of the tested specimen, this type of curve cannot be used for comparison of the biomechanical properties between different specimens. Because of this limitation, a normalized version of the force-elongation curve is preferred. This normalized curve is obtained by calculating the stress and the strain the tested tendon undergoes. The tendon stress (σ) is obtained by dividing the measured force (F) by the cross-section area of the tendon (A), as shown by equation 1.1, while the tendon strain is commonly estimated using the engineering strain (ε) formulation. For the engineering strain calculation, the length of the sample is measured before and after deformation, corresponding to L_0 and L, respectively, as described in eq 1.2.

$$\sigma = F/A \tag{1.1}$$

$$\varepsilon = \frac{L - L_0}{L_0} \Longleftrightarrow \varepsilon = \frac{\sigma}{E} \tag{1.2}$$

The relation between stress and strain can then be formulated using the Young's modulus (E) as shown by equation 1.2.

Engineering strain formulation is adopted in this work since it is the most commonly used for the characterization of tendon mechanics [59, 167, 167].

After calculating tendon stress and strain, the obtained normalized curve corresponds then to the stress-strain curve typically used to describe tendon mechanics. An example of a tendon stress-strain curve is shown in Fig. 1.5.

Limitations of global strain quantification using isolated tendons are the possible non-uniform strain distribution along the tendon and the improper clamping of the same.

Microscopical analysis

Besides the evaluation of the global strain of isolated tendons, also local deformations, which occurs at a microscopical scale, have been investigated.

Examples of works which investigated the local distribution of strain within the tendon are Arnoczky *et al.* [15], Screen *et al.* [191], Cheng *et al.* [33], Szczesny *et al.* [208] and Thorpe *et al.* [209].

All these works, with the exception of the work of Thorpe [209], evaluated the biomechanical properties of rat tail fascicles and used custom-built uniaxial tensile test devices. For imaging purposes, confocal microscopy was used and the nuclei of the cells, present in the fascicles, were stained using fluorescent dye.

In the work of both Arnoczky *et al.* and Screen *et al.* [191, 15], the local strain was calculated from the displacement of the nuclei of the cells during the stretching of the samples. The tracking of these nuclei was done manually.

As for the work of Cheng *et al.* and Szczesny *et al.* [33, 208] both used an ion laser to photobleach the studied fasciles. Cheng *et al.* photobleached a grid on the studied specimen, while Szczesny *et al.* photobleached four lines. Local strain for both these works was calculated from the grid deformation (obtained after preprocessing of the acquired data via thresholding and skeletonizing steps) and line tortuosity, respectively.

For the work of Thorpe *et al.* [209], horse fascicles, harvested from the forelimbs distal to the carpus, were used instead of rat tail fascicles. As with the above studies, these fascicles were stained with collagen dye and a grid was photobleached onto the fascicles. Incremental strain was applied using a custom-built uniaxial tensile device. Strain was calculated from the deformation of the photobleached grid, which was, obtained after preprocessing of the acquired images (thresholding and skeletonizing).

1.4.2 Quantification of the biomechanical properties of in-vivo Achilles musculotendinous unit

The in-vivo quantification of the biomechanical properties of the musculotendious unit of the Achilles tendon is commonly performed using either magnetic resonance imaging or ultrasound imaging (explained in detail in section 2). For both imaging modalities, the most common approach is the tracking of a reference point during maximum or sub-maximum isometric contraction. The most commonly used reference points are the myotendinous junction of the medial head of the gastrocnemius (GM MTJ), and the myotendinous junction of the soleus (SOL MJT). The tracking of this point(s), during a specific exercise, yields the elongation of the tendon, as shown in Fig. 1.10, while a dynamometer is commonly used to measure the muscle force generated during the activation process. The obtained elongation-force can then be transformed into a stress-strain curve by quantifying the cross-sectional area of the tendon and measuring the length of the tendon during rest, using the same imaging modality. The selection of these junctions is commonly performed manually, and a wealth of studies have been presented using this methodology [153, 73, 53, 203, 115, 90, 174, 64, 65, 165, 106].

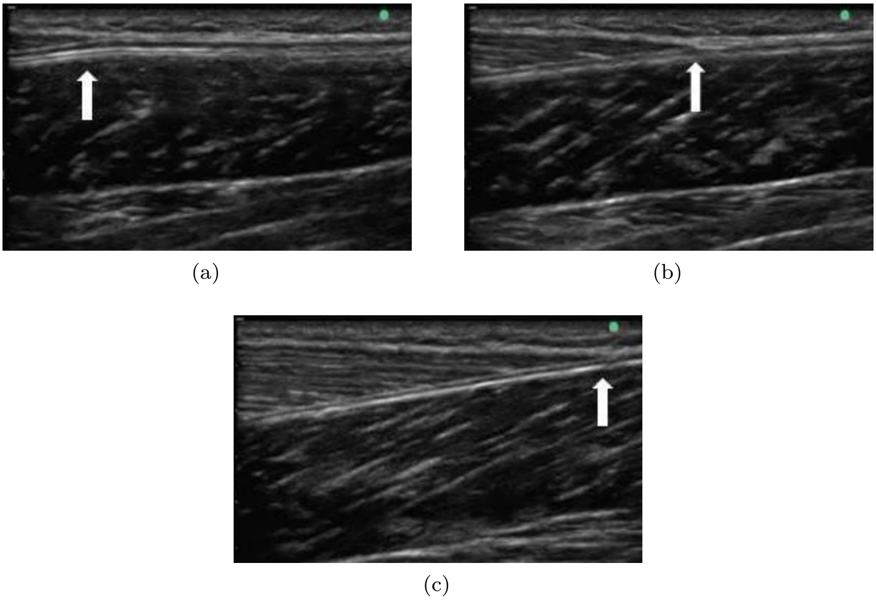
(a) (b) (c)

Figure 1.10: Example of sequential ultrasound images that show the medial gastrocnemius MTJ displacement (arrow), from plantarflexion to maximum dorsiflexion. (obtained copyright from Oliveira *et al.* [167])

1.4.3 Quantification of the biomechanical properties of in-vivo free Achilles tendon

As for the in-vivo characterization of the biomechanical properties of the free Achilles tendon, evaluation is commonly performed using ultrasound imaging (US). This choice is motivated by the higher resolution of ultrasound imaging, in comparison with MRI, and the possibility of acquiring fast dynamic images with US.

Four different approaches, namely **RF-based methods**, **B-mode based methods**, **shear-wave elastography** and **ultrasonographic tissue characterization**, have been used by different groups to characterize the biomechanical properties of the free Achilles tendon.

RF-based methods take advantage of the high resolution of the RF signal along the beam profile (axial direction). For this type of tendon mechanics quantification, pre-deformed and post-deformed RF-signals are recorded. The pre-deformed RF-signal is then divided into an axial–lateral grid of small windows, and the search for the matching RF-window in the post-deformed RF-signal is performed by maximizing the correlation coefficient between the two windows [145, 218, 67, 34, 32, 26]. The tissue displacement is obtained from the distance, in the RF-space, between the pre- and post-deformed regions. For this type of approach, the obtained motion estimations are typically smoothed after each iteration.

Examples of works which employed RF-based methods for the quantification of the biomechanical properties of the free Achilles tendon are the works of Slane *et al.* and Franz *et al.* [35, 196, 75, 197, 77]. Slane *et al.* developed in 2014 a RF-based method for tendon tissue displacement and strain quantification, which was later used by Franz *et al.* [75, 77]. The RF data was acquired at 63 frames per second, with a transducer of central frequency of 10MHz (L14-5/38, Ultrasonix Corporation, Richmond, BC, Canada). These images had a field of view of 38 x 30mm, image dimension of 128x1560 pixels and a pixel size of 0.297 x 0.019mm. The initial step for the quantification of the tissue motion was the upsampling of the acquired RF data by a factor of 4 perpendicularly to the beam profile (lateral direction) and by a factor of 2 along the beam profile (axial direction). This upsampling was performed to increase the spatial density of the correlation function later used to track the tissue motion. As auxiliary step, a B-mode image was created to allow the positioning of a grid of nodes. This grid covered $\approx$ 25mm of the tendon length, and the distance between nodes was 1mm along the lateral direction and 0.5mm along the axial direction. The frame-to-frame displacement of the nodes was computed using a 2D normalized cross-correlation function. The cross-correlation kernel had a size of 1.4 x 2.8mm and was centered at the respective node of the subsequent frame. Gross displacement of the kernel was obtained by maximization of the normalized cross-correlation function. This displacement estimate was then fine tuned by fitting a 2D quadratic spline to a 5x5 matrix of normalized correlations centered at the gross displacement. A correlation threshold of 0.7 was used to discriminate between valid and invalid estimations. In order to obtain a smooth tissue displacement estimation, a median filter (3x3 nodes) was applied to the frame-to-frame estimations and the node positions were updated according to this smoothing. The cumulative node displacement was obtained by repeating these steps. Besides forward motion estimation, also backward motion estimation was performed. In the end, a weighted average of the node displacements according to the forward and backward estimations was calculated.

Lateral strain at node i was estimated using the following equation:

$$\varepsilon_i = \frac{u_{i+1} - u_{i-1}}{x0_{i+1} - x0_{i-1}} \tag{1.3}$$

where $x0$ represents the node position in a pre-deformed frame, u represents the displacement of the node along the lateral direction and $i+1$ and $i-1$ refer to the nodes to both sides of the node of interest.

RF-based methods are sensitive to the size of the kernel chosen to evaluate the correlation function, as demonstrated above by the need of estimating gross displacement using a 2D normalized cross-correlation window, followed by the fine-tuning of the initial displacement estimation using a 2D quadratic spline. The size of this kernel can influence robustness to noise, if defined too small, or limit the diagnosis to global estimations, if defined too large. Furthermore, RF-based methods have high computational requirements due to the computation of the correlation functions on such high resolution data. This high computation can even be increased because of the upsampling of the RF data that is sometimes recommended to further increase the spatial density of the correlation function [124, 34].

Besides RF-based methods, also **B-mode methods** have been used to quantify the biomechanical properties of the Achilles tendon. Arndt *et al.* [12] used EchoPac™ of GE for the quantification of these properties while Fröberg *et al.* [80] developed an in-house block matching approach.

As for the methodology applied by the EchoPac™ method, very few information can be found in the literature due to the commercial nature of this method. Nonetheless, it is known that this is a B-mode based block-matching approach and a general description of this type of methods is given below.

Block-matching methods determine the local deformation by searching for the maximum similarity between an area of a template image (kernel) and the acquired B-mode cine-loop [204, 125, 176, 228, 184, 7]. Large or more local deformations can be recovered using multiscale block-matching approaches.

Arndt *et al.* [12] acquired 2D US images with a transducer of central frequency of 11MHz, a frame-rate of 78.5 frames-per-second, at a depth of 4cm. Three kernels were displaced equidistantly, within the tendon, from its more superficial region to the deeper. The distance between the center of these kernels was $\approx$ 2mm. After the selection of the region of interest and the placement the kernels, the EchoPac™ returns the tracking results.

Besides Arndt *et al.* [12], also Fröberg *et al.* [80] used a B-mode based block-matching approach for the quantification of the biomechanical properties of the Achilles tendon. The presented method was previously developed by Larsson *et al.* [130] for a cardiological application and adapted by Fröberg *et al.* for this tendon application. In this work, 2D US images were acquired using a transducer with a central frequency of 14MHz, with a frame-rate of 65.3 frames-per-second, at a depth of 4cm. The tissue displacement of the Achilles tendon was quantified after surgical repair of the tendon. For this motion estimation, a kernel with width (lateral) and length (axial) of 5.72mm and 2.75mm was used and normalized cross-correlation was the used similarity measure. The sub-sample motion was detected using a spline interpolation of the cross-correlation function. Afterwards, a median filter was applied on a region of 0.3mm (lateral) and 0.08mm (axial) to remove outliers. The motion between kernels was obtained through anisotropic linear interpolation. The cumulative displacement maps were estimated by applying a linear interpolation between the different frames.

The limitations of this type of method are similar to the ones presented by the RF-based methods, and are mostly dependent on the choice of the kernel size. This method can also suffer from speckle decorrelation, a phenomenon that can occur more easily due to the limited spatial size of the kernel, and it can lead to errors in the tissue tracking. Furthermore, the tracking of the tissue displacement within each kernel region is independent of the neighboring kernels, which can result in incoherent tissue tracking results. Due to this, a posterior regularization step is required to obtain smooth tissue tracking results. This regularization is usually achieved by applying a median filter [200] to the displacement estimations, averaging the strain maps [217] or by fitting a linear curve through the displacement estimations and obtaining a least-square 1D strain estimator [201].

Besides B-mode based block-matching approaches, also B-mode image registration approaches can be used to quantify the biomechanical properties of the Achilles tendon. Image registration methods align two or more images to each other by applying the optimal transformation that maximizes the similarity between those images. The used transformation is a mapping function that maps the points from one image to the other image [199]. The quality of the alignment is then evaluated according to an image similarity measure (e.g. sum of squared differences, correlation ratio, or mutual information) and the obtained results are subsequently used for an optimization process (e.g gradient descent). The transformations typically used for image registration approaches are rigid transformations, including rotation and translation; affine transformations, including scaling and skewing; or nonrigid transformations, using a spatially-varying deformation model [6, 61, 95, 178, 51].

Despite its interesting methodological specifications, image registration approaches have not been broadly applied for the quantification of biomechanical properties of the Achilles tendon. On the other hand, this type of approach has been rather successfully [94] applied in the cardiological field. This comparison is of value since, similarly to the quantification of biomechanical properties of the Achilles tendon, cardiological applications also attempt to estimate strain from tissue displacement, using both RF and B-mode data.

The biomechanical properties of the Achilles tendon, mainly viscoelasticity, have also been investigated using **shear-wave elastography**. In summary, shear-wave elastography (SWE) assesses the elastic properties of tissues by analyzing the displacement/speed of the shear-waves, perpendicular to the direction of the exploratory force. Stiff, rigid tissue presents less displacement when compared with elastic, soft tissue [58, 21].

When investigating the applicability of SWE for the quantification of the biomechanical properties of the Achilles tendon, Slane *et al.* and Aubry *et al.* [195, 19, 18] acquired both US B-mode and shear wave data using a 10MHz linear array transducer with a lateral field of view of 50mm (L15-4, Aixplorer, Supersonic Imagine, Aix-en-Provence, France). The pre-settings selected for this acquisition were: application mode: superficial musculoskeletal application; persist: high; and smoothing degree: 7. A region of interest was selected within the tendon and the shear wave speed was calculated by the device within that region. SWE presents several innovative and interesting advantages to estimate tissue elasticity. However, this modality is limited to 2D imaging and it is still in development phase.

Besides the above mentioned methods, also **ultrasonographic tissue characterization (UTC)** can be applied to evaluate the biomechanical properties of the tendon [216]. This technique consists of the acquisition of several 2D US images, with the transducer placed transversely to the tendon, from the aponeurosis to the calcaneus. In the end, the acquired 2D US images are compounded to obtain a 3D US image which is consequently evaluated according to the obtained speckle pattern. The assumption behind this technique is that depending on the size of the anatomical structure being scanned, echoes can be divided into two classes, namely: "structure-related" and "interfering" classes. The first class, composed by "structure-related" echoes , named type I and type II, are assumed to be generated by large structures, thus one interference and one reflection. This type of speckles is then stable over a large number of continuous transverse images while the transducer is being displaced. Alternatively, "interfering" echoes (types III and IV) are assumed to represent several smaller structures, thus multiple interferences and multiple reflections. These echoes are then characterized by a lack of stability over the continuous transverse images. Despite the interesting results obtained from the UTC imaging, due to the static analysis of this type of approach, the functional information that can be retrieved from the evaluated tendons is very reduced.

Lastly, not only image processing methods can be used to evaluate the biomechanical properties of the free Achilles tendon. The work of Lyman *et al.* [146] demonstrated the use of small extensometers, which were placed on different regions of cadaveric tendons, for the estimation of local strain, during different exercises. Digital image correlation (DIC) [206] is another approach that can be used to quantify tissue displacement of the tendon. In this technique, an oil-based paint speckle pattern is applied to the tendon and the tendon surface deformation is measured. Regarding these two approaches, the limitations of the use of extensometers are the invasive nature of these instruments, while the limitations of quantifying the biomechanical properties of the Achilles tendon using DIC is the quantification of the deformation of the surface of the tissue, rather than the tissue itself.

1.4.4 Thesis scope and contribution

When evaluating the benefits and limitations of the different quantification approaches described, the first selection criterion refers to the two clinical questions above presented. The first clinical question referred to the quantification of the local biomechanical properties of **in-vivo tendons**. In light of this, methods which are used to perform global and local quantification of the biomechanical properties of isolated tendons are excluded. Similarly, methods which are used to quantify the biomechanical properties of the musculotendinous unit were also excluded. In this manner, only methods utilized for the quantification of the biomechanical properties of the free Achilles tendon are considered viable.

As for the second clinical question, attempts of improving the accuracy of the results reported in the state-of-the-art were performed by, in first instance, investigating the applicability of two different novel acquisition modalities, namely, a novel *2D high-spatial and high-temporal resolution* ultrasound acquisition system and a *3D high-spatial resolution* ultrasound acquisition system.

As the previous section describes, non-uniform deformation of the Achilles tendon has been reported both at the level of subtendons and at the level of fascicles. Interestingly, a reduction of this subtendon and fascicle sliding has also been reported to occur with ageing, which is in turn associated with an increased incidence of tendinopathy.

In light of these facts, it is crucial to use imaging acquisition systems which allow to capture this type of sliding effect. Conventionally, ultrasound imaging is used for the acquisition of in-vivo images at the level of the free Achilles tendon. However, all the above mentioned studies used ultrasound acquisition central frequencies in range of 10MHz-14MHz. The use of a higher frequency acquisition system is beneficial for more accurate quantification of tendon deformation because it would allow a more detailed representation of the Achilles tendon and the capturing of deformation of tendon structure at finer scales. More information about this hypothesis and the use of higher-frequency ultrasound imaging is given in chapter 2.

Results can also be improved by acquiring US images at higher frame-rates, than the ones used in the literature (65.3 - 78.5 frames-per-second). This hypothesis is based on the fact that the tissue deformations between consecutive images acquired at higher frame-rates are smaller, and lower deformations are believed to lead to an easier and faster tracking of the speckle motion. Furthermore, a reduction of speckle decorrelation is also believed to be achieved by increasing the acquisition frame-rate [139, 170].

One last hypothesis which attempts to improve the accuracy of the results obtained in the literature concerns the investigation of a *3D high-spatial resolution* ultrasound imaging system. All of the above mentioned methods used conventional ultrasound acquisition frequencies in two-dimensions. However, the tendon suffers three-dimensional deformations which can lead to out-of-plane motion and consequently to a reduction of the accuracy of the estimated biomechanical properties of the Achilles tendon.

Due to the intrinsic higher spatial resolution of the images acquired using the novel imaging systems, B-mode based methods were preferred to RF-based methods. Moreover, attempts to increase the accuracy of the estimated biomechanical properties of the Achilles tendon were performed by investigating the applicability of an image registration rather than a block-matching method. One of the reasons behind this choice is the lower computational effort of B-mode based methods in comparison to the high computational effort of the RF-based methods. Regarding the accuracy of B-mode estimations against RF-estimations, conflicting results were presented in the literature. Lopata *et al.* [144] demonstrated that there are advantages of using a combined three-level coarse-to-fine approach where B-mode data was used for the image registration process at the coarsest scale, and RF-data was used for the middle and fine scales. On the contrary, Slane *et al.* [35] demonstrated better performances using RF-data instead of B-mode data. Albeit these results, and considering the already high-spatial and high-temporal resolution US acquisition system, it was not believed that using RF-data would result in significantly better quantification of the biomechanical properties of the Achilles tendon.

Lastly, an image registration approach was preferred to a block-matching. Heyde *et al.* [94] compared the performance of these two methodologies for cardiac US strain estimation and they obtained a higher correlation between the image registration estimations and the ground-truth, than for the block-matching method. In this work, it was hypothesized that these differences were due to the different underlying tracking principles used by block-matching and image registration methods. In summary, in this work, Heyde *et al.* [94]

hypothesized that the local independent tracking of speckles performed by the block-matching method, in a frame-by-frame approach, could be hampered if the selected kernel regions suffer from speckle decorrelation. The same would not occur with the image registration methods because the motion estimation was resolved by finding the optimal deformation field between consecutive frames. Moreover, for image registration methods, the regularization step was intrinsically embedded in the optimization process while for the block-matching methods, the regularization of the obtained displacement fields had to be done *a posteriori* and errors could be introduced at this stage.

Although image registration presents some advantages in comparison to block-matching methods, the decision of using a B-mode image registration approach was mostly dependent on the elevated expertise of the group where this work was developed (ESAT-PSI, KU Leuven) in image registration approaches. Furthermore, a previous work developed within the group demonstrated promising preliminary results for an image registration based approach for tendon strain quantification [6]. In this work, Almeida *et al.* [6] used conventional ultrasonography (12 MHz) for the acquisition of in-silico and in-vitro images. Quantification of strain was obtained using a deformable B-spline image registration approach. The strain was estimated with deviations of -0.011%±0.053% for in-silico data and ±0.28% for in-vitro data.

In conclusion, the applicability of a 2D high-spatial and high-temporal resolution ultrasound acquisition system and of a 3D high-spatial resolution ultrasound acquisition system were investigated. The acquisition of this new type of images was then combined with a B-mode based image registration approach for the characterization of tendon biomechanics.

1.5 Thesis goal and structure

As discussed above, the three clinical questions this work intends to answer are:

- How can we quantify the biomechanical properties of the Achilles tendon in-vivo?
- How can we improve the performance of our method, in comparison with the state-of-the-art?
- Are the obtained results clinically meaningful and can these be used for tendinopathy diagnosis?

The primary goal of this work was then to answer those clinical questions by: implementing for the first time a high-spatial resolution ultrasonography platform for 2D and 3D in-vivo quantification of tendon mechanics; developing fine-tuned global and local image registration approaches for the quantification of the tendon biomechanics at higher spatial resolutions; and evaluating the discrimination power of the developed method for diagnosis or discrimination between asymptomatic and symptomatic tendons. A secondary, but very important, goal of this thesis was the development of a user-friendly application for the quantification of the biomechanical properties of the Achilles tendon to be incorporated in the clinical practice.

Due to the crucial role of the used imaging acquisition system, chapter 2 describes the basic ultrasound imaging physics and the high-spatial resolution ultrasound imaging system used throughout this work. Chapter 3 describes the validation of the 2D high-spatial and high-temporal resolution US acquisition system using an image registration method developed for **global strain estimations**. For this validation, global strain estimations were preferred to local estimations due to the available ground-truth. The dataset used for this validation consisted of 2D high-spatial and high-temporal resolution images of in-silico and ex-vivo data.

After validation of the novel high-spatial and high-temporal resolution ultrasound imaging system, a deformable image registration method developed for the characterization of the **local tendon biomechanics** is presented in chapter 4. In this chapter, the results obtained for this local characterization are presented, and validated. Due to the absence of ground-truth for local deformation of the Achilles tendon, a psychometric validation approach was used [182].

Chapter 5 focuses on the expansion of the used high-spatial resolution US acquisition system from two-dimensional to three-dimensional imaging. In this part, the potential impact of out-of-plane motion on tendon strain estimations using 2D ultrasound imaging is investigated. For this test, 3D in-silico, in-vitro and ex-vivo data were acquired. Global strain estimations were the preferred validation step due to the available ground-truth for this type of data. In the end, a comparison between the 2D global tendon strain estimations obtained in chapter 3 and the results obtained using the 3D high-spatial resolution US images was performed.

Chapter 6 presents the final conclusion, where the main findings of this work, both from a biomechanical and from a technical perspective are described. Furthermore, the outcome for the initial clinical questions is discussed and the suitability of the developed application for use in the clinical practice is evaluated. The last chapter 7 describes the possible future steps for this work.

Chapter 2

2D and 3D high-spatial and high-temporal resolution ultrasound imaging system

Contents

Quantification of local tendon biomechanics is believed to be of crucial importance for a better understanding of the functional role of tendons and their pathogenesis process and risk.

Both magnetic resonance imaging (MRI) and ultrasound imaging are well suited for tendon imaging [31, 212]. On the one hand, MRI is considered the gold standard imaging technique because it provides a good anatomic overview and excellent soft tissue contrast. On the other hand, ultrasound imaging is faster and easily accessible, it allows acquisition during dynamic exercises, and it yields higher spatial resolution images [31, 212]. Due to these advantages, ultrasound

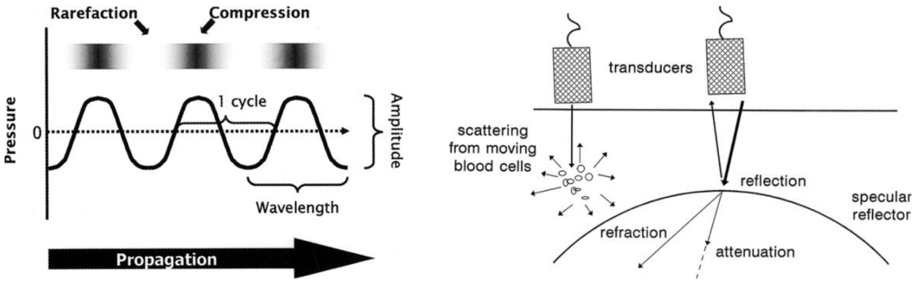

(a) (b)

Figure 2.1: Ultrasound physics. (a) Visual description of the US wave. (b) Different interactions of US beam with tissue. (obtained copyright from [133])

imaging (US) has become an ubiquitous tool to evaluate soft tissue like tendons and muscles [83] and is therefore the imaging modality used in this work.

Typical acquisition of Achilles tendon US images is performed by firstly applying a water-based gel on the area of the tendon being studied. This gel ensures proper contact between the scanned surface and the transducer so that the propagation of the US waves from and to the transducer is possible. The transducer is then aligned with the Achilles tendon and dynamic (2D+t) US images are obtained by scanning the same anatomical plane while exercising the tendon (e.g. isometric contraction or passive elongation).

This chapter provides an overview of the US physics and image acquisition process, followed by a description of the ultrasound imaging system used in this work, for both the acquisition of 2D and 3D images.

2.1 Basic ultrasound physics

Ultrasound imaging is based on the propagation of high-frequency sound waves (ultrasound) and it allows the construction of morphological images of organs. These high-frequency sound waves (also called pulses) are mechanical impulses of kinetic energy (vibrations) that can be described according to their frequency (Hz), wavelength (mm) and energy (dB). The kinetic energy is propagated through a medium by alternating between compression and rarefaction as represented in Fig. 2.1(a) [133]. Ultrasound waves have a frequency too high for humans to hear (greater than 20kHz) and for medical US devices, frequencies between 1 MHz and 20 MHz are conventionally used.

As soon as the US pulse interacts with human tissue, various interferences take place. For imaging purposes, the most interesting US interference is the reflection of the US pulses. This reflection, also called echo, occurs at the boundary between two materials that have different acoustic impedance. Acoustic impedance is the product of the material density and the speed at which sound can travel through the medium. The larger the difference in acoustic impedance between two materials, the larger the echo that will be generated [2].

As the US pulse propagates, its energy is reduced by attenuation. This attenuation occurs due to interference processes such as the previously mentioned reflection but also because of refraction, scattering and absorption of the US pulse, as demonstrated in Fig.2.1 (b). Reflection and refraction occur when scanning structures larger than the US wavelength, while scattering occurs when the US pulse encounters objects that are smaller than the US wavelength such as blood cells. The amount of attenuation depends directly on the frequency of the US pulse [2]. As a result, short-wavelength US, thus high-frequency pulses, produces high-resolution images at the cost of small scanning depth, whereas long-wavelength US, thus low-frequency pulses, have the ability to penetrate tissues more deeply but with a lower resolution [133].

US imaging suffers mainly from acquisition artifacts such as acoustic shadowing and reverberations. Acoustic shadowing produces shadows in the image and occurs when the scanned material is so dense (e.g. bones) that most of the US waves are reflected back. Reverberations also affect the US image quality and occur when an ultrasound beam encounters two strong parallel reflectors. In this situation, the US beam reflects back and forth between the reflectors, and the US transducer interprets the US waves returning from the reverberations as being located deeper than in reality. This artifact occurs because the emission and reception of the US wave were longer than it should [11, 172].

2.1.1 Linear ultrasound array transducers

US images are acquired using ultrasound transducers. This type of transducers convert electrical to mechanical energy, and vice-versa, according to the piezoelectric operation principle [156]. This principle states that when a piezoelectric material is mechanically deformed, it produces an electrical field and vice-versa. A linear array transducer is then the assembly of multiple transducer elements as shown in Fig. 2.2. Linear arrays are operated by activating several transducer elements at the same time generating an ultrasound beam (Fig. 2.2). Focusing along the axial direction is obtained by the emission of US waves from different elements with different time delays and the focusing of the beam along

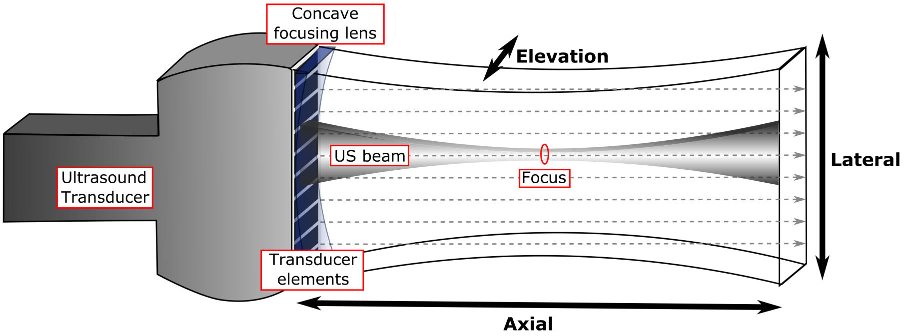

Figure 2.2: Linear ultrasound array transducer. In this figure the three different directions: axial, lateral and elevation of US acquisition are represented.

the elevation direction is obtained using a concave lens as represented in Fig.2.2. Activation of the transducer elements occurs sequentially along the array of elements, and a new image line of echoes is obtained for each set of elements. This line of echoes is called channel data or raw radio-frequency (RF) data.

The B-mode US image generation process is represented in Fig. 2.3 and it starts when the US transducer converts the reflected and scattered US waves into electrical raw-RF data, also called channel data (Fig. 2.3). Data from several channels are then used for the beamforming process where the delay of each echo is corrected considering its distance to the transducer element. This time delay correction is followed by summing the corrected delayed signals such that a beamformed RF-line is obtained. Afterwards, an envelope detection, used to detect the peaks of the received signal, and a log compression, used to reduce the dynamic range of the received signal, are applied to the beamformed RF-line [5]. The output can then be converted into a B-mode image where the lateral direction is given by the position of each beamformed RF-line (respective to the transducer dimensions), and the axial direction represents the depth in the scanned surface where a certain echo was detected.

In Fig. 2.3, the red arrows show the B-mode image generation process where a certain amplitude echo is stored according to its lateral coordinate and at a certain depth. In this example, *px2* is closer to the transducer than *px3* and it has higher gray-scale intensity. This image formation process is repeated for every line of echoes.

The echo line received by the transducer provides information about the internal structure of the scanned tissue. This echo is obtained by coherent summation of signals (smaller echoes) from scatterers that are typically smaller than the spatial resolution of the imaging system [179]. When these scatterer signals are

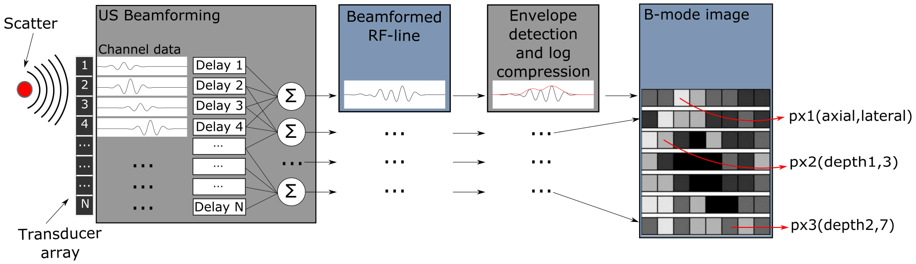

Figure 2.3: B-mode image formation process.

coherently added, an interference pattern designated as *speckle* is obtained [27]. B-mode images of soft tissues are characterized by the presence of speckles, which have a granular texture of bright and dark spots. This speckle is responsible for the degradation of the image resolution and image contrast. However, although classified as noise, speckles can be regarded as a deterministic artifact [27]. The deterministic speckle function allows then obtaining the same speckle pattern when scanning the same tissue under the same conditions in two different occasions. Furthermore, the speckle relative position is considerably stable over time [227]. These two speckle characteristics are then the basis of tissue tracking methods in B-mode images as explained in section 1.4.3.

On the other hand, speckle decorrelation, which occurs when the speckle patterns obtained before and after tissue motion are not invariant, is also known to occur when acquiring dynamic US images. Speckle decorrelation has been reported to occur when the tissue undergoes certain types of motion and deformation, such as compression, expansion, shearing and rotation. This speckle decorrelation occurs both at the level of geometric transformations, as well as at the level of speckle intensity changes, caused by changes of the interference of backscattered ultrasound pulses. The impact of speckle decorrelation can, nonetheless, be reduced by performing image acquisitions at high-frame rates, leading to almost identical speckle patterns between consecutive frames [139].

Different transducers can then be used to acquire ultrasound images of tendons and, depending on the type and properties of the transducer, different spatial resolutions can be obtained. Spatial resolution describes the ability to distinguish between objects located at different positions in space and it is commonly defined along the beam propagation direction (axial resolution) and perpendicularly to this (lateral resolution). By definition, the axial resolution of the ultrasound imaging system corresponds to the capability of the system to distinguish between echoes originated from two objects lying one behind the other, along the axial direction. Axial resolution of the ultrasound imaging system can be quantified using equation 2.1 where λ stands for the wavelength of the US wave, which is obtained by dividing the speed of sound in soft tissue ($\approx$ 1540m/s) by the central frequency used; and #cycle stands for the number of cycles emitted per US pulse. The numerator of this equation is also described as spatial pulse length (SPL). Besides axial resolution, spatial resolution of 2D imaging systems is also defined along the lateral direction. Lateral resolution is then the ability of the system to discriminate between two objects situated side by side, along the lateral direction. Lateral resolution of the ultrasound imaging system can be quantified using equation 2.2 where *focal depth* corresponds to the depth to which the US waves are focused, and *aperture* corresponds to the active area of the transducer that receives the US echoes. In this equation, the $2 \times$ *aperture* applies if the receive and the transmit aperture are equivalent. Otherwise, this expression should be replaced by $\textit{transmit aperture} + \textit{receive aperture}$.

$$\text{axial resolution} = \frac{\lambda \times \#\text{cycle}}{2} \tag{2.1}$$

$$\text{lateral resolution} = \frac{\lambda \times \text{focal depth}}{2 \times \text{aperture}} \tag{2.2}$$

Due to the striated morphology of tendons and their elongated shape, linear array transducers are best suited for tendon imaging. In this type of tissue, the examination should, if possible, be performed with the beam propagating perpendicularly to the tissue [36]. With this type of acquisition, strong reflections and good visualization of the anatomical details are obtained.

2.1.2 Low- vs. high-spatial resolution ultrasound imaging

High-frequency (also called high-spatial resolution) ultrasound imaging ($>$ 16 MHz) has been recommended [83] for the acquisition of tendon US images because this type of system yields higher spatial resolution, which allows a better description of the tendinous tissue.

As explained above, speckles are the result of coherent summation of scatterers, which are, in turn, dependent on the spatial resolution of the US acquisition system used. In other words, if lower US spatial resolutions are used, speckle patterns will result from the interference of the US wave with larger structures, while when using higher US spatial resolutions, speckle patterns will result from the interference of the US wave with smaller structures.

To further describe the differences between lower and higher-frequency US, let us compare the spatial axial resolution that would be obtained when acquiring US data with a conventional 10MHz US acquisition system (L14-5/38 Linear

Table 2.1: US spatial resolution of three different transducers

Central frequency	10MHz	21MHz	40MHz
US axial resolution(μm)*	308	36.7	19.2
US lateral resolution(μm)*	52.3	104.3	33.5
Image depth(mm)	50	30	15
Image width(mm)	38	23	14

* calculated at a focal depth of 10mm.

transducer, Ultrasonix medical corporation, Canada) and two higher-spatial resolution transducers (Vevo2100, MS250 – central frequency 21MHz, MS550 – central frequency 40MHz, Visualsonics, FUJIFILM, Inc, Toronto, Canada).

Table 2.1 shows the computed US spatial resolutions for the three different transducers. All these calculations were performed at a focal depth of 10mm. Due to the confidentiality of the data, #cycles per pulse, transducer element width and spacing between transducer elements are not presented here. These results show that the transducer with the highest central frequency returned the highest axial resolution while the opposite is the case for the transducer with the lowest central frequency. However, a different tendency is obtained for the calculated lateral resolution, where the transducer with a central frequency of 21MHz was the one with the worst lateral resolution. The reason for this is that this transducer is the one with the smallest aperture. As this table also shows, there is a compromise between the choice of central frequency and the field of view (maximum image depth and width) of the obtained US image.

Despite the assumed benefits of using high-frequency (high-spatial resolution) US instead of conventional 2D US for tendon imaging, this type of systems tends to be substantially more expensive than the conventional ones. Nevertheless, whether the potential benefits of high-frequency ultrasound outweigh this higher cost should be considered for the application at hand.

2.1.3 Low- vs. high-temporal resolution ultrasound imaging

Besides high-spatial resolution US, the acquisition of dynamic US images and the characterization of the tendon biomechanics can also be influenced by the low- vs. high-temporal resolution used during the acquisition process. By using a higher frame-rate (high-temporal resolution), a higher speckle correlation is hypothesized to occur between consecutive images, which would enhance the ability to accurately track the motion [139, 170]. High speckle correlation occurs when the changes in the speckle pattern are small, while low speckle correlation occurs when comparing two speckle patterns that have low similarity. If the acquisition at a lower frame-rate (low-temporal resolution) is performed instead, the possibility of speckle decorrelation between consecutive frames can increase and this speckle decorrelation can impair the good performance of the tendon tissue tracking methods.

2.2 Ultrasound imaging of tendons

In this section, the ultrasound imaging systems used for the acquisition of 2D and 3D images are explained.

The physiological interpretation of the content of 2D US images of the Achilles tendon is firstly presented. Finally, the rationale behind the choice of the imaging system used for the acquisition of 2D high-spatial and high-temporal resolution US images is presented. The following sections concern the acquisition of 3D high-spatial resolution US images and describe in first instance the different 3D US imaging systems commercially available. Aftertwards, the rationale for the selection of the 3D high-spatial resolution US imaging system used in this work is presented.

2.2.1 2D high-spatial and high-temporal resolution ultrasound imaging of tendons

One of the hypotheses of this work is that the use of an US imaging system with higher central frequency is beneficial for the quantification of the biomechanical properties of the Achilles tendon. This hypothesis relies on the fact that, by tracking speckle patterns of smaller structures, the deformation of smaller tendon structures, like fibers and small caliber fascicles, can be recovered allowing hence a better description of the inter-fiber and inter-fascicular deformation reported in the literature [12, 80, 35, 196, 75, 197, 77].

Physiological interpretation of US tendon images

In order to understand the implications of acquiring US images with higher or lower US central frequencies, a qualitative comparison was performed (Fig. 2.4) between the type of image acquired with a conventional 10MHz transducer (L14-5/38 Linear transducer, Ultrasonix medical corporation, Canada) and two transducers of 21MHz and 40MHz (Vevo2100, MS250 –central frequency 21MHz, MS550 – central frequency 40MHz).

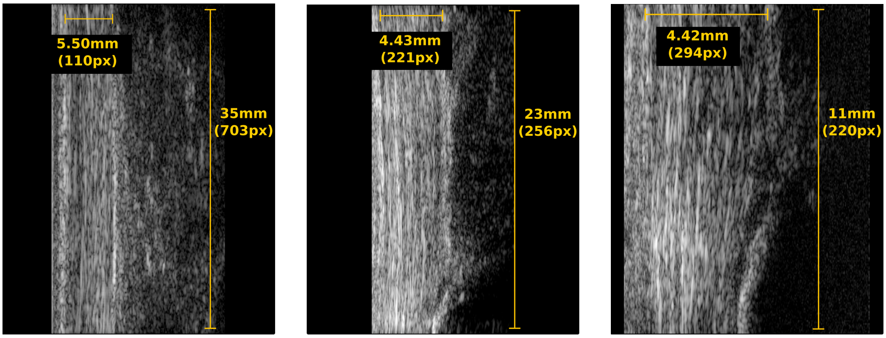

(a) (b) (c)

Figure 2.4: US images of Achilles tendon acquired with different central frequencies. (a) corresponds to an image acquired with a 10MHz transducer, (b) with a 21MHz transducer and (c) with a 40MHz transducer. Tendon width, length and corresponding image resolution is annotated in yellow.

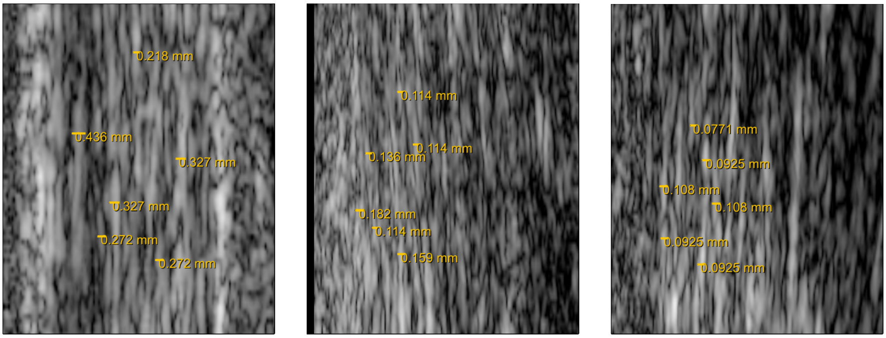

(a) (b) (c)

Figure 2.5: Close-up of Figure 1. Speckle pattern thickness is measured in the 10MHz image (a), 21MHz image (b) and 40MHz image (c)

As Fig. 2.4 shows, the Achilles tendon is represented with higher detail in Fig. 2.4(b) and Fig. 2.4(c) than in Fig. 2.4(a). The ultrasound axial pixel size of these images is 0.308mm for the 10MHz transducer, 0.0367mm for the 21MHz transducer and 0.0192mm for the 40MHz transducer.

A better perspective on the actual resolution of the images acquired using different transducers is presented in Fig. 2.5, which are close-ups of the images in Fig. 2.4.

As these images demonstrate, with the 10MHz system it is possible to measure a striated speckle pattern with an average thickness of ≈0.30mm. This obtained striated speckle would correspond to structures smaller than the system's axial resolution (0.308mm, see table 2.1), namely large fascicles (according to the classification of Handsfield [86]). On the other hand, with the 21MHz system, the striated speckle pattern that can be measured has an average thickness of ≈0.14mm and the striated speckle pattern that can be measured with the 40MHz system has an average thickness of ≈0.0951mm. The speckle pattern obtained from the 21MHz and 40MHz transducer are then assumed to represent tendon structures with thickness smaller than the axial resolution of these transducer (0.0367mm and 0.0182mm, respectively), which corresponds to tendon fibers (according to the classification of Handsfield [86]). This smaller structures will then merge to represent larger structures such as the speckle patterns represented with a thickness of ≈0.14mm or ≈0.0951mm. It can then be extrapolated that speckle patterns with smaller thickness corresponds to the representation of smaller tendon structures.

However, the acquisition of images with higher resolution along the beam propagation direction is compromised by a reduction of the field of view along the lateral direction, as presented in table 2.1. Regarding the lateral resolution, the impact of this parameter on the physiological interpretation of Achilles tendon US images was not strongly considered due to the elongated tubular structure of tendons and fascicles (length ≈ 3cm [47]). In other words, the tubular structure of the Achilles tendon and its components makes that the discrimination between two tendon structures, which are situated side by side, with a resolution of 0.05mm, 0.1mm or 0.03mm, for the 10MHz, 21MHz and 40MHz transducers, respectively, believed be not crucial.

Selected 2D high-spatial and high-temporal ultrasound imaging system

Considering the interest in using, for the first time, a higher-frequency ultrasound acquisition system for the quantification of the biomechanical properties of the Achilles tendon, the ultrasound imaging system Vevo 2100 of Visualsonics (FUJIFILM, Inc, Toronto, Canada) was selected (Fig. 2.6). As for the choice of the transducer, a larger field of view was preferred to an even higher axial frequency. In this way, the transducer MS250 - 21MHz was selected over the transducer MS550- 40MHz. Lateral resolution was not considered strongly because of the reasons described before.

Besides the interest in investigating the implementation of this novel higher-frequency ultrasound imaging system, it was also of interest to acquire images with high-temporal resolution. This high frame-rate acquisition is known to

Figure 2.6: Example of Vevo 2100 system during in-vivo Achilles tendon high-spatial and high-temporal US acquisition.

lead to lower deformation between consecutive frames, which is hypothesized to lead to more reliable tracking of the tissue motion and to reduce the impact of speckle decorrelation[139, 170]. Moreover, the acquisition at high-frame rates is also important for the adaptability of the implemented image acquisition process to real life situations, such as jumping or running exercises. In these situations, strain rates of 10%/s have been reported [225].

The acquisition of these images is performed in a cine fashion. Cine images correspond to the acquisition of a 2D frame every n seconds (defined by the used frame-rate), which are stored digitally as a sequence of individual frames.

2.2.2 3D high-spatial resolution ultrasound imaging of tendons

As reported in the introduction, chapter 1.1, the subtendons of the Achilles tendon are believed to undergo a "twisting effect" at the level of the free Achilles tendon. Furthermore, it has also been demonstrated that the free Achilles tendon undergoes non-uniform deformation which may be related with the mentioned "twisting effect" or the different loading properties of the different subtendons. Both these deformation patterns are believed to occur in a three-dimensional space. Hence, if a two-dimensional acquisition system is used to

Table 2.2: Image acquisition parameters of the investigated 3D ultrasound imaging systems

Ultrasound system - 3D	Central frequency (MHz)*	Axial resolution (mm)	Max depth (mm)	Max width (mm)
Esaote	7.2	0.2	44	22
Supersonic	8.9	0.17	43	38
Philips	8	0.19	-	-
Siemens	2.2	0.7	-	-
GE	10	0.15	-	-

* Calculation was done assuming a 2 wave cycle

capture the deformation of the Achilles tendon, the rotation which occurs to the soleus, medial-gastrocnemius and lateral-gastrocnemius subtendons will produces a deformation of the tissue into the field of view and away from this. This effect is called out-of-plane motion and it is defined in the literature as one of the most important sources of quantification errors when estimating the biomechanical properties of the Achilles tendon using 2D images. Due to that, in chapter 5, the applicability of 3D high-spatial resolution imaging for the acquisition of tendon images is investigated.

The minimum axial resolution expected for this type of 3D US acquisition was defined between 50-400μm, which was equivalent to the tendon fascicle level. By fulfilling this expected axial resolution, inter-fascicle sliding deformations were expected to be captured.

The typical shape of the tendons also played an important role in the definition of the pre-requisites for the acquisition of 3D high-spatial resolution US images. Because of the elongated shape of tendons, it is of interest to acquire the largest field-of-view possible.

To investigate the most advantageous 3D US systems for the quantification of the biomechanical properties of the Achilles tendon, a comparison study was performed between the commercially available 3D US imaging systems which is presented below.

Comparison of commercially available 3D ultrasound imaging systems

Table 2.2 represents a comparison of the investigated 3D ultrasound imaging systems.

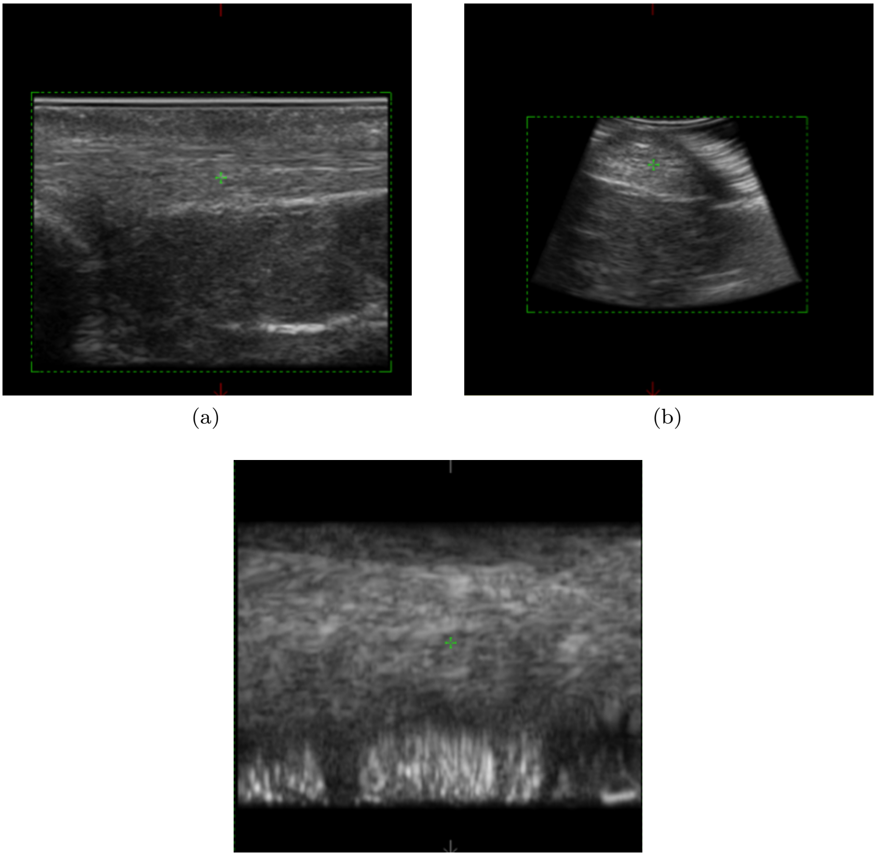

(a) (b)

(c)

Figure 2.7: 3D US image acquired with Esaote 3D US imaging system. (a) Sagittal view, (b) axial view, and (c) coronal view of in-vivo Achilles tendon.

As presented above, the transducer BL433 Volumetric apple-iQ-Linear of the *Esaote 3D ultrasound system* presented an US axial resolution of 0.2mm. Due to this low axial resolution, the pre-requirement of achieving an axial resolution lower than 400μm was not fulfilled. Figure 2.7 shows an example of a 3D US image acquired with the Esaote 3D ultrasound imaging system.

Besides the Esaote system, also the *Supersonic 3D ultrasound system* was evaluated. Also in this case, the estimated low axial resolution prevented the selection of this ultrasound imaging system for the quantification of the biomechanical properties of the Achilles tendon. Figure 2.8 shows an example

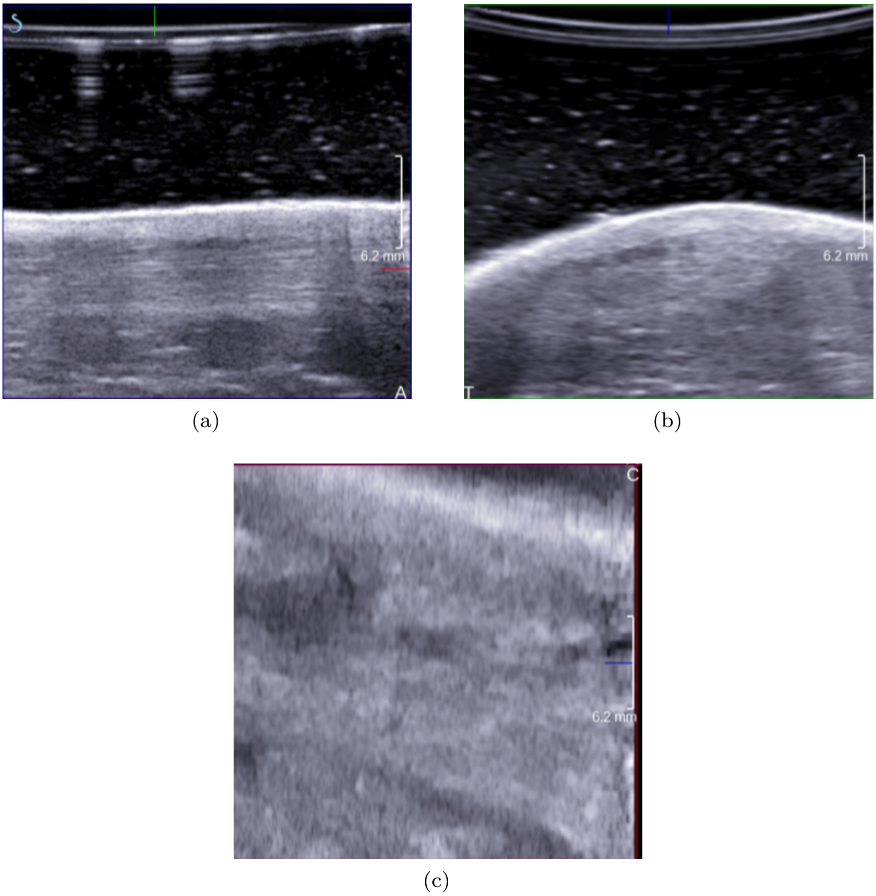

Figure 2.8: 3D US image acquired with Supersonic 3D US imaging system. (a) Sagittal view, (b) axial view, and (c) coronal view of in-vivo Achilles tendon.

of a 3D US image acquired with the Supersonic 3D ultrasound system.

Besides these systems, also the 3D US imaging solutions of Philips, Siemens and General Electric were investigated. For this evaluation, the 3D US transducer of Philips with the highest resolution (VL13-5) was considered. However, because of its axial resolution lower than was was stipulated, this system was not considered. The 3D transducer of Siemens examined in this work presented also a larger axial resolution than what was intended and was not considered. Lastly, the 3D transducer of General Electrics fulfilled the stipulated pre-requisites, but this system was commercially released only shortly before (June 2012) the beginning of this doctoral work and, because of that it was not considered.

Comparison of commercially available semi-3D ultrasound imaging systems

Considering the lack of a 3D high spatial resolution ultrasound acquisition system that would fullfil the established pre-requisites for tendon imaging, the commercially available semi-3D US acquisition systems were considered. When using *semi-3D* US acquisition systems, several 2D US images are acquired while displacing the transducer. Within this category, the tracking of the transducer's position in a freehand fashion or the use of a linear translation system are the two approaches most commonly used. In freehand 3D tracking, the operator moves freely the transducer while its position is tracked and multiple 2D US images are acquired. The most commonly used approaches for the tracking of the US transducer position are electromagnetic tracking and optical tracking. However, this type of systems requires special conditions to ensure the correctness of their position estimates, i.e. absence of ferromagnetic metals when using electromagnetic trackers and uninterrupted line of sight between the cameras and the transducer when using optical systems. Optical systems are more accurate than electromagnetic systems, and can achieve a spatial accuracy up to ±0.2mm [22] while electromagnetic position sensors can achieve an accuracy of up to ± 0.5mm. Both these systems can be affected by image transfer and temporal calibration errors and by improper spatial calibration [213].

When using linear translation systems, the transducer is driven by a motor which moves in a linear fashion, parallel to the patient's skin and perpendicularly to the image plane. Due to the controlled manner in which the transducer is displaced, this type of systems can present higher positional accuracy than the freehand tracking systems. Nonetheless, this higher accuracy is only possible due to the reduced flexibility of the system. One source of inaccuracy of this type of system, which also affects freehand tracking systems, is the assumption that the subject has not moved during the acquisition. Any movement of the patient can result in a distortion of the 3D data.

Selected 3D high-spatial resolution ultrasound acquisition system

Considering the pre-requisites described before, the Vevo 2100 of Visualsonics (FUJIFILM, Inc, Toronto, Canada) was the chosen imaging device. This system insured the acquisition of US images with high-spatial resolution, due to its wide transducer assortment, with transducers with central frequency ranging

Table 2.3: US axial resolution and field of view of images acquired with different transducers and frequencies *.

Transducer and frequency	US axial resolution (mm)	Max image width (mm)	Max image depth (mm)
MS250, 21MHz	75	23	30
MS400, 30MHz	50	15.4	20
MS550, 40MHz	40	14.1	15
MS700, 50MHz	30	9.7	12

Quoted at the geometric focus.

from 15MHz to 50MHz. Furthermore, this acquisition system allows as well the acquisition of 3D high-spatial resolution images.

Considering the wide assortment of available transducers, a qualitative evaluation of the image quality acquired with each transducer was performed. In order to test the axial resolution of the system, an agar-based phantom with amorphous graphite scattering was constructed and a metal wire with diameter of 0.05mm was included in the phantom. The introduction of the wire within the phantom was intended to mimic a structure of similar thickness as the tendon fibers (0.001mm-0.02mm).

Four transducers (MS250, MS400, MS550 and MS700) were evaluated. Figure 2.9 represents a sagittal cross-section of the 3D US image acquired with the four different transducers. The metal wire is present in Fig. 2.9(a-c) but not in Fig. 2.9(d). The absence of the metal wire in this last figure is caused by the very reduced scanning depth allowed by the MS700 (50MHz) transducer. In figures Fig. 2.9(a-c) the metal wire is represented with equivalent quality.

Table 2.3 shows an overview of the different axial resolution and field of view of the four different transducers.

Due to the pre-requisites of maximum coverage of the Achilles tendon length and its high spatial resolution (in comparison with conventional systems), the MS250 transducer with a central frequency of 21MHz was preferred.

This type of transducer yields images with an axial resolution of 75 μm and a lateral resolution of 165 μm, at the geometric focus (15 mm along the elevation direction)

For the acquisition of 3D high-spatial resolution US images, the 3D module provided by VisualSonics with the Vevo2100 was used. This module consisted of a mechanical arm, allowing displacements along vertical and horizontal direction,

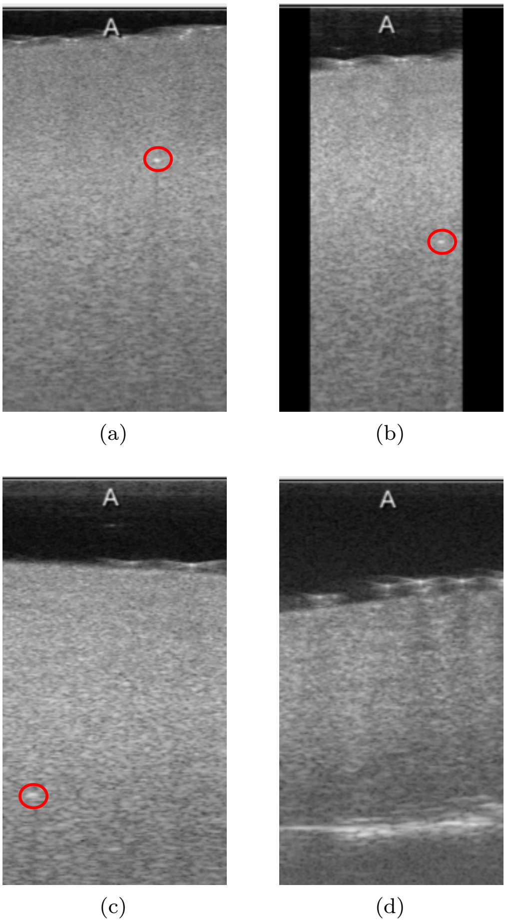

(a) (b)

(c) (d)

Figure 2.9: Sagittal cross-section of 3D US images acquired with Vevo2100 using different transducers and different central frequencies. Presence of metal wire is highlighted by red circle. (a) MS250, central frequency 21MHz; (b) MS400, central frequency 30MHz; (c) MS550, central frequency 40MHz; (d) MS700, central frequency 50MHz.

on which a stepper motor is attached (Fig. 2.10(a)). This motor displaced the US transducer along the elevation direction, and a single 2D US image was acquired at each step position . The minimum allowed step-size, along the elevation direction, is 0.03 mm and the maximum scanning distance along the elevation direction is 15 mm. The speed of the transducer's translation is 6 mm/s.

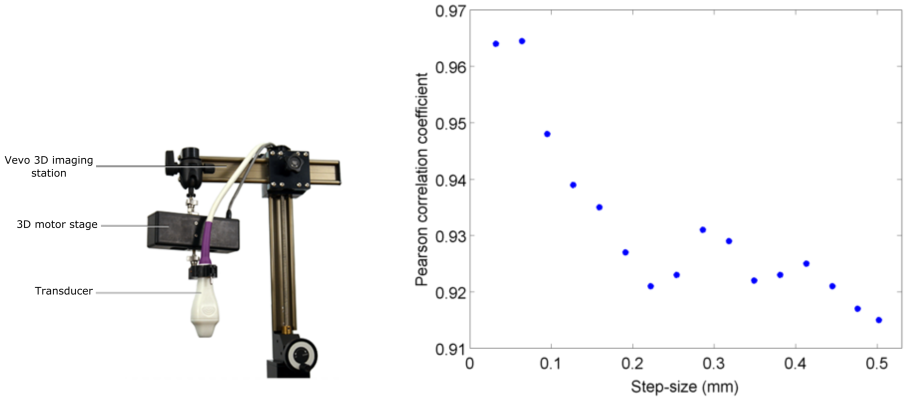

(a) (b)

Figure 2.10: 3D imaging of tendons: (a) 3D high-spatial resolution US acquisition station, and (b) Pearson correlation coefficient between consecutive 2D frames using different step-sizes.

At the end of the sweep, the multiple 2D high-spatial resolution US images acquired were concatenated into a 3D high-spatial resolution US image. The elevation resolution of this 3D high-spatial resolution US image was defined by the step-size used for the acquisition process. In this manner, an average of 100 frames was acquired along the elevation direction using a step-size of 0.09 mm.

Although the minimum step-size of the motor is 0.03mm, when scanning a distance of 15mm, the minimum step-size allowed increased to 0.09mm. The impact of using a larger step-size was then evaluated by computing the Pearson correlation coefficient between consecutive 2D slices using different step-sizes. As Fig. 2.10(b) demonstrates, a step-size of 0.09mm ensures a correlation of 0.947 between consecutive 2D frames which is important for the reconstruction of the 3D volume.

The final 3D image voxel size was [0.02,0.09,0.09]mm for the axial, lateral and elevation direction, respectively. Figure 2.11 exemplifies the acquisition process of the 3D high-spatial resolution US image [1].

As discussed previously, the image registration methods developed for the 2D global and local tendon characterization rely deeply on the high speckle temporal correlation provided by the US acquisition (100 frames-per-second). However, for the 3D experiments, high acquisition frame rates were not possible.

---

[1] Video with example of 3D high-spatial resolution US acquisition is available in the digital version

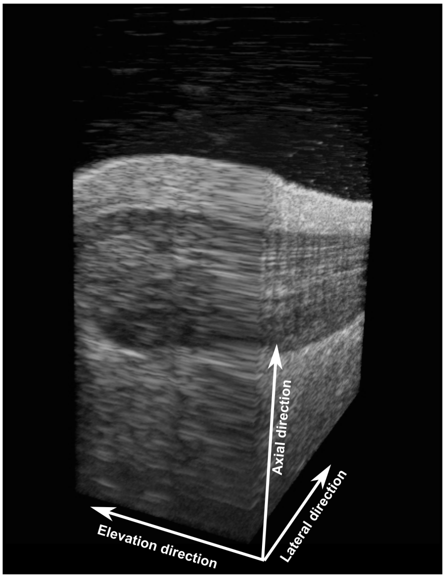

Figure 2.11: 3D high-spatial resolution US acquisition. (a) 3D high-spatial resolution US acquisition station and (b) example of 3D high-spatial resolution US acquisition. Each slice corresponds to a 2D US acquisition. Video with example of 3D high-spatial resolution US acquisition is available in the digital version

This limitation was due to the fact that the acquisition frame-rate, allowed by the used 3D ultrasound imaging system, was limited by the speed of the motor used for the transducer's translation. However, to compensate for the limited frame-rate in case of 3D imaging experiments, low strain increments were applied to the different types of data.

2.2.3 Summary

In conclusion, the Vevo2100 was the US imaging acquisition system chosen for the acquisition of 2D and 3D US images of the Achilles tendon. The selection of this US imaging system was mostly dependent on its spatial resolution, which is higher the one presented by the conventional US acquisition systems. The advantage of this US acquisition system for the acquisition of 2D US images was the combination of its high-spatial resolution together with its high-temporal resolution. On the other hand, the advantage of using the Vevo 2100 for the acquisition of 3D US images was the possibility of acquiring high-spatial resolution US images in a 3D fashion.

Chapter 3

Global tendon strain estimations for validation of 2D high-spatial and high-temporal resolution ultrasound acquisition system

Contents

In this chapter, the necessary steps for the validation of the novel high-spatial and high-temporal (HST) resolution US acquisition platform are presented.

The first section describes the image registration method developed for global strain quantification. In this section, a detailed description of the image registration principle and parameters is given. The second section describes the different types of data used and the following two sections present the validation of the obtained global strain estimations. In the end, some concluding remarks are presented.

3.1 Image registration approach for characterization of global tendon mechanics using 2D high-spatial and -temporal resolution US data

When following an image registration approach, global tissue motion can be estimated by finding the global transformation τ that maximizes the spatial correspondences between the moving and reference image. An example of a reference image would be an image of the tendon at its resting length, while an example of a moving image would be an image of a stretched tendon. The image registration method usually involves the selection of a number of corresponding control points (samples) in both reference and moving images and, from the correspondences between the selected points of these two images, a transformation function can be derived. Afterwards, this transformation function can be applied to determine the correspondence between all the other points in the reference and moving images [82].

The correspondence between the two images may be estimated over *all* pixels but the use of the full image resolution leads to high computational costs. In order to reduce this computational cost, different image sampling strategies can be followed. The commonly used image samplers include a grid sampler, where a regular grid is defined on the reference image and N points are selected on that grid. This sampler down-samples the image resolution without smoothing. Besides a grid sampler, a random sampler can be used instead. A random sampler selects N random voxels and every voxel has an equal chance to be selected. New samples can be selected for every evaluation step.

The registration problem can then be described below. Given the coordinates of N corresponding points in both moving and reference images:

$$(x_i, y_i), (X_i, Y_i) : i = 1, .., N \tag{3.1}$$

it is intended to determine the transformation $\mathbf{f}(x, y)$ with components $f_x(x, y)$ and $f_y(x, y)$ that satisfy the following equation:

$$X_i = f_x(x_i, y_i), \qquad Y_i = f_y(x_i, y_i), \qquad i = 1, ..., N \tag{3.2}$$

When ***f****(x,y)* has been determined, given the coordinates of a point *(x,y)* in the reference image, the coordinates of the corresponding point in the moving image *(X, Y)* can be determined. In image registration methods, the image which is kept unchanged is defined as fixed or reference image, while the moving image (also called sensed image) is the one whose geometry must be changed to match the reference image.

The type of transformation function chosen (rigid, affine or nonrigid) should depend on the type and magnitude of geometric differences expected between the two images. Rigid and affine transformations should be used in registration problems where nonlinear geometric differences are negligible. Alternatively, nonrigid transformations are needed to register images which have complex geometric differences between them. Rigid transformations are the simplest and are defined according to 4 parameters in 2D spaces (or 6 in 3D spaces): 2 translation parameters and 2 rotation parameters. As for nonrigid transformations, commonly used transformations are: similarity transform, which can recover rotation, translation and uniform scaling transformations; affine transform, which is considered to stand between rigid and nonrigid transformations and can recover rotation, translation, scaling and shearing transformations; and deformable registrations, which can recover non-linear geometric differences.

Considering that the geometric difference expected between the reference and moving images (tendon at its resting length vs. stretched tendon) is a stretching of the tendon along one direction and compression along another direction (anisotropic scaling), a rigid transformation is not considered. Furthermore, the expected anisotropic scaling of the moving image (compression along one direction and stretching along the other) also allows the rejection of the similarity transformation from the set of candidate transformations. In the end, the affine transformation is the transformation of choice because it allows the recovery of the expected geometric differences.

The definition of an affine transformation, in 2D, is given below:

$$X = ax + by + c, \tag{3.3}$$

$$Y = dx + ey + f. \tag{3.4}$$

This type of transformation has six parameters. The parameters a, b, d and e define the affine matrix (3.5) and the parameters c and f correspond to the translation parameters.

Homogeneous coordinates can be used to represent affine transformations as demonstrated below:

$$\text{Affine transformation} = \begin{bmatrix} a & b & c \\ d & e & f \\ 0 & 0 & 1 \end{bmatrix} \tag{3.5}$$

By using homogeneous coordinates, translation, rotation, scaling and shearing can be obtained by matrix multiplication as represented by matrix M in eq. 3.6. In this equation, M represents an affine matrix obtained from the composition of a translation with a scaling, a rotation, and a second translation ($T' * R * S * T$). In this case, *T'* corresponds to a translation with vector (t'_x, t'_y), R corresponds to a counter-clockwise rotation by an angle of θ, S corresponds to a scaling with factors (s_x, s_y), and T corresponds to a second translation with vector (t_x, t_y),

$$M = \begin{bmatrix} s_x \cos\theta & s_y - sin\theta & t_x s_x \cos\theta - t_y s_y \sin\theta + t'x \\ s_x \sin\theta & s_y \cos\theta & t_x s_x \sin\theta + t_y s_y \cos\theta + t'y \\ 0 & 0 & 1 \end{bmatrix}. \tag{3.6}$$

Registration problems are commonly formulated as optimization problems in which a cost function C is optimized with respect to a transformation τ, in this case an affine transformation, as shown in eq. 3.7. Typical cost functions weigh similarity, S, against regularity, P. Because for the estimation of the global transformation, no regularity term was used, this step is equivalent to maximizing the image similarity S.

$$\begin{gathered} \tau = arg\,\underset{\tau}{min}\, C(\tau; A, B), \text{with} \\ C(\tau; A, B) = -S(\tau; A, B) + \gamma P(\tau) \end{gathered} \tag{3.7}$$

where A represents the reference image, B represents the moving image and γ represents the weighting of the regularity term.

Due to the lack of clear anatomical landmarks within the US images of the Achilles tendon, the registration of images acquired with the same imaging modality and the expected brightness constancy of the obtained speckle pattern, intensity-based methods, in other words, methods which optimize the cost function directly from the pixel intensity information, were preferred.

There are several monomodal, intensity-based, similarity measures that can be used for this problem. One of the simplest is the sum of squared intensity differences between images, SSD:

$$SSD = \frac{1}{N} \sum_{x_A \epsilon \Omega^{\tau}_{A,B}} (A(x_A) - B^{\tau}(x_A))^2 \tag{3.8}$$

N corresponds to the number of pixels in the overlap domain $\Omega^{\tau}_{A,B}$ and B^{τ} represents the image B transformed by a given mapping τ.

Another monomodal, intensity-based, similarity measure that can be used is the sum of absolute differences, SAD (equation 3.9),

$$SAD = \frac{1}{N} \sum_{x_A \epsilon \Omega^{\tau}_{A,B}} \left| A(x_A) - B^{\tau}(x_A)) \right| . \tag{3.9}$$

The advantage of SAD, over SSD, is that this measure is more robust to the presence of a small number of intensity outliers, which can strongly affect the outcome of the registration when using SSD.

Besides SSD and SAD, also correlation techniques can be used as similarity measure for monomodal registrations. This type of methods assumes a linear relationship between the intensity of the corresponding structures in both moving and reference images. An example of a similarity measure which uses correlation techniques is the cross correlation, $CrossCorr$, [96].

$$CrossCorr = \sum_{x_A \epsilon \Omega^{\tau}_{A,B}} A(x_A) B^{\tau}(x_A) \tag{3.10}$$

Beside the cross correlation measure, also the correlation coefficient, CC, can be used. This correlation coefficient corresponds to a normalized version of the cross correlation measure.

$$CC = \frac{\sum_{x_A \epsilon \Omega^{\tau}_{A,B}} (A(x_A) - \bar{A})(B^{\tau}(x_A) - \bar{B})}{\sqrt{\sum_{x_A \epsilon \Omega^{\tau}_{A,B}} (A(x_A) - \bar{A})^2 \sum_{x_A \epsilon \Omega^{\tau}_{A,B}} (B^{\tau}(x_A) - \bar{B})^2}} \tag{3.11}$$

where $\bar{A}$ is the mean voxel value in image $A \mid_{\Omega^{\tau}_{A,B}}$, and $\bar{B}$ is the mean of $B^{\tau} \mid_{\Omega^{\tau}_{A,B}}$ [96].

When translating the applicability of these different monomodal intensity-based similarity measures to the acquired data, SSD is the preferred metric because: (1) it is assumed that the speckle patterns obtained using ultrasound imaging have a deterministic nature, which means that corresponding tendon structures, in the two registered images, will have equivalent intensity values, fulfilling in this way the brightness constancy constraint equation [102]; (2) the acquisition at high-frame rates (100fps) allows obtaining almost identical speckle patterns, leading to a more reliable matching and reduction of the impact of speckle decorrelation [139, 170]; (3) SSD similarity measure has been reported in the literature [126] to perform better than correlation similarity measures for registration of ultrasound images which do not present large differences between both speckle intensity and geometry, which is assumed to be the case when acquiring US images at high frame-rates. Besides these reasons, computational efforts for correlation methods are higher than for SSD and correlation methods have been reported to perform poorly in cases of image skewing [226] and sub-optimal in cases of imaging scale and rotation [138].

Typical image registration approaches require an iterative approach for the optimization of the estimated transformations. In this optimization process, the optimizer gradually refines the estimated transformation. In each iteration, the current estimated transformation is used to calculate the similarity measure and subsequently, the optimizer makes a new estimate of the transformation, which is, in theory, better than the previous transformation. This evaluation and re-estimation of the transformation continues until the algorithm converges. Convergence occurs when no transformation is found that yields better values of the similarity measure than the current transformation [96]. When the convergence point is reached, the obtained transformation is assumed to correctly register the moving and reference images.

To solve the optimization problem, an iterative optimization strategy is employed:

$$\mu_{k+1} = \mu_k + a_k d_k, k = 1, 2, 3, ... \tag{3.12}$$

with μ being the transformation parameters at iteration k, d_k being the search direction, and a_k a scalar gain factor controlling the step-size along the search direction. In this equation, the search direction and gain factors are defined so that the sequence μ_k converges to the local minimum of the cost function. Different optimization functions differ in the way the gain factor a_k and the search direction d_k are computed.

Popular optimization methods include gradient descent [163], quasi-Newton [101], nonlinear conjugate gradient [50], stochastic gradient descent [121], and evolution strategy [88]. The first four calculate their search direction d_k based on the derivative of the cost function with respect to the different parameters $\frac{\partial C}{\partial \mu}$. However, the first three methods are deterministic gradient-based algorithms while the fourth is a stochastic gradient-based algorithm. The difference between these is that the calculation of the $\frac{\partial C}{\partial \mu}$ using the deterministic methods is assumed to be exact, while with the stochastic method, approximations of the derivatives can be used for the calculation of $\frac{\partial C}{\partial \mu}$. Regarding evolution strategy, the calculation of the search direction is not performed using $\frac{\partial C}{\partial \mu}$, but rather using a random process. For notational convenience, $\frac{\partial C}{\partial \mu}$ will be henceforth referred to as g. A short summary of these methods is given below.

The **gradient descent method** [163] takes steps in the direction of the negative gradient of the cost function:

$$\mu_{k+1} = \mu_k - a_k g(\mu_k) \tag{3.13}$$

where $g(\mu_k)$ is the derivative of the cost function evaluated at the current position. This type of optimization process can then be implemented by following a decaying function $a_k = a/(k + A)^{\alpha}$, with user-defined constants $a > 0$, $A \geq 1$, and $0 \leq \alpha \leq 1$.

The **quasi-Newton methods** [163, 101] are inspired by the Newton-Raphson algorithm, which is defined as:

$$\mu_{k+1} = \mu_k - [H(\mu_k)]^{-1} g(\mu_k), \tag{3.14}$$

where $H(\mu_k)$ is the Hessian matrix of the cost function, evaluated for parameters μ at iteration k. The use of second-order information, by this optimizer, allows better theoretical convergence properties than the gradient descent. However, the computation of the Hessian matrix can be expensive, reason for which an approximation to the inverse of the Hessian $L_k \approx [H(\mu_k)]^{-1}$ is used. In this manner, the approximation is updated at each iteration. Quasi-Newton methods are commonly combined with inexact line search routines, determining a gain factor a_k which ensures progress towards the solution. The determination of the optimal registration parameters is then obtained by:

$$\mu_{k+1} = \mu_k + a_k L_k g(\mu_k) \tag{3.15}$$

An adaptation of the Quasi-Newton approach is the Broyden–Fletcher–Goldfarb––Shanno (BFGS) algorithm which has been reported to be very efficient in many applications [163]. In this optimizer, the gain factor (step length) a_k is chosen to satisfy the Wolfe condition [163] which ensures a sufficient decrease of the cost function and enforces reasonable progress towards a point of the cost function, where the derivative is zero.

The **nonlinear conjugate gradient methods** are an extension of linear conjugate gradient methods [92], initially designed for solving a set of linear equations. The nonlinear version of this method is then suitable for more general nonlinear functions. In this optimization, the search direction d_k is defined as a linear combination between the gradient $g(\mu_k)$ and the previous search direction d_{k-1}.

$$d_k = -g(\mu_k) + \beta_k d_{k-1} \tag{3.16}$$

Several β_k factors have been proposed in the literature and the work of Dai *et al.* [50] provides an extensive review on this topic.

As for the **stochastic gradient descent methods**, the same scheme as for the deterministic gradient descent is followed. However, due to the stochastic nature of this method, the derivative of the similarity function $g(\mu_k)$ is replaced by an approximation $\tilde{g}_k$, resulting in the following scheme:

$$\mu_{k+1} = \mu_k - a_k \tilde{g}_k \tag{3.17}$$

This type of method is often applied when the computation of the exact derivative is too expensive. Despite the decrease of the computational cost, using an approximation may have negative effects on the speed of the convergence [121].

The last optimization scheme here described is **evolution strategies** which are based on the principle of natural selection. The covariance matrix adaptation evolution strategy (CMA-ES) is one of the most commonly used evolution strategy optimization methods. Each iteration of the CMA-ES algorithm is defined by three phases: offspring generation, selection, and recombination. In the offspring phase, a set of λ trial search directions is generated from a normal distribution:

$$d_k^{(\ell)} \sim \mathcal{N}(0, C_k), \ell = 1, 2, ...\lambda \tag{3.18}$$

The population size λ is defined by the user and the covariant matrix C_k favours search directions that were successful in the previous iterations. For each trial search direction, the cost function is evaluated for $\mu_k + a_k d_k^{(\ell)}$, and a_k corresponds to the gain factor which controls the step size. The selection phase consists of selecting $P \leq \lambda$ trial directions that yield the lowest similarity measure. The pth best trial direction of all λ directions is denoted $d_k^{(p;\lambda)}$. In the recombination phase, a weighted average of the P selected trial directions is computed:

$$d_k = \sum_{p=1}^{P} w_p d_k^{(p;\lambda)} \tag{3.19}$$

After each iteration, a_k and C_k are updated, based on the previous search direction, and the selected trial search directions $d_{k-1}^{(p;\lambda)}$ [121, 89].

From the presented optimizers, the optimizer of choice to minimize the cost function C is the quasi-Newton limited memory BFGS because of its good performance for optimization the 6 parameters for an affine transformation while eliminating the need for storing the inverse of the Hessian matrix during the optimization routine [30].

One of the constraints of optimization algorithms is that these can converge to an incorrect solution called local optimum. Depending on the type of transformation used (rigid or nonrigid), different degrees of freedom, hence, different parameter spaces can be obtained. This parameter space can be understood as a multidimensional image with as many dimensions as the degrees of freedom of the transformation. In this image, the intensity at each location corresponds to the similarity measure and the regularity term for a certain transformation, obtained with certain parameters μ. When considering low intensities as good values of similarity, and high intensities as poor ones, the ideal parameter space would be characterized by a sharp low intensity optimum with the intensities increasing monotonically with the distance away from the optimum position. In this case, the optimizer would find the same optimum position independently from the starting position. However, parameter spaces for image registration approaches are frequently not that simple. These parameter spaces usually contain multiple local optima, and the registration can converge to the wrong optimum [96].

One way of avoiding local optima is by using multi-resolution approaches. In this type of hierarchical approaches, both moving and reference images are first registered at lower resolutions, and the obtained transformation solution at this lower resolution is afterwards used as initialization for the next higher resolution registration. This process is repeated for the number of multi-resolution levels selected. In this work, a three level multi-resolution strategy, using a pyramidal scheme, was used. An image pyramid is a multi-resolution representation of an image constructed by consecutive filtering and subsampling. To implement this pyramidal multi-resolution scheme a Gaussian pyramid with $\sigma = 4$ and $\sigma = 2$ pixels is used along both the axial and the lateral direction. Figure 3.1 exemplifies the three resolution levels of the pyramidal scheme used in this work. The reason behind the choice of three layers (L0=original resolution, $L_1\sigma = 2$, $L_2\sigma = 4$) resides on the content of the structure of interest. In this manner, in L2, the registration is mostly guided by the larger and brighter structures present within the tendon, in L1, the transformation estimate for the lower resolution image is used as initialization, and the information of smaller structures guides the registration at this level. As for the registration at L0, the previous transformation is used as initialization and the image features present at the full resolution images are used to improve the registration performance.

The advantage of multi-resolution approaches, i.e. avoiding local minima, reflects on the better registration accuracy of larger deformations at the lower resolutions, and a better registration accuracy of smaller deformations at higher resolutions. This approach is commonly defined as coarse-to-fine registration and its importance has been demonstrated by Curiale *et al.* [49].

Besides the parameters mentioned above (similarity measure, transformation, optimization and multi-resolution) some considerations should be made regarding the type of interpolation function used for the transformation of the moving image. During the registration process, the reference image is iteratively transformed into the moving image until the optimizer converges, in theory, to a global optimum. During this iterative process, the reference image is transformed with respect to the moving image by means of interpolation. The choice between a higher-order (e.g. cubic B-splines) and lower order (linear or nearest neighbors) interpolation method comes with a compromise between quality and speed. In order to balance this compromise, a lower-cost interpolation (first-order B-spline) is used until the transformation is close to the desired solution, being then replaced by a more expensive interpolation (third-order B-spline) in the last iterations.

One last decision that should be made to complete the image registration

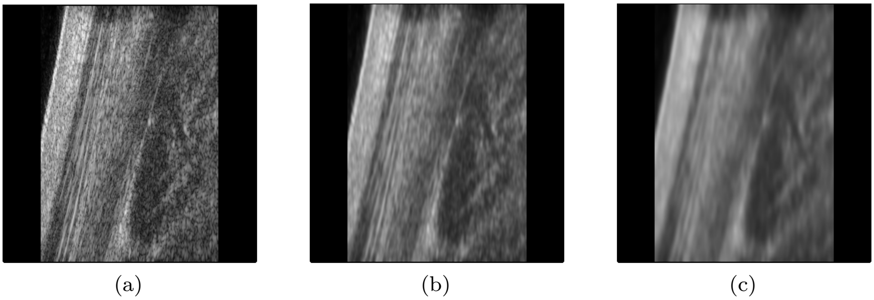

(a) (b) (c)

Figure 3.1: Example image of 3 layer, multi-resolution pyramidal scheme used. (a) corresponds to the original image, (b) corresponds to the original image after smoothing ($\sigma = 2$) and downsampling, using a nearest neighbor method, by a factor of 2, along both directions, (c) corresponds to the original image after smoothing with an $\sigma = 4$ and a downsampling factor of 4.

framework, concerns the choice between the use of a pairwise or groupwise image registration strategy. In the first one, a reference image is selected from a set of images and a repeated pairwise registration is applied between that reference image and each of the other images. However, this type of approach may be flawed because: (1) only information for the given time point, and not all the time points, is used for the pairwise registration; (2) the obtained transformations may be biased towards the selected reference image, which may lead to errors in the final alignment. Groupwise registration was proposed to address these issues and it consists of using all of the available information, from the entire image dataset, to estimate the optimal transformation of these images to a reference space. In this case, the information from the entire dataset is used, rather than that from only a single pair of images [230, 44, 45]. However, in general, unlike pairwise image registration methods, where the correspondences between the two images are optimized, the dimensionality of the parameter space obtained for groupwise registration, in which the optimization is performed grows rapidly with the number of corresponding control points evaluated. This very high dimensionality of the parameters space can then present limitations to groupwise registration approaches for the finding of the optimal solution [98].

Considering the interest in registering data acquired from the same volunteer, which means that gross anatomical features are present in all images; acquired at high-temporal resolution during a short temporal window, which leads to small deformation between consecutive pair of images; and the interest in applying the developed method to the clinical practice, hence need for fast processing, a pairwise registration approach was preferred.

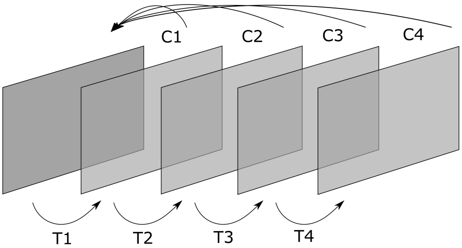

Figure 3.2: Image registration strategy. The bottom axis (T_n) represents the pairwise image registration, and the top axis (C_n) accounts for the composition process to the first frame.

This pairwise registration is performed for each consecutive pair of images, as represented in Fig. 3.2 (bottom-axis). Once this pairwise registration is completed, each pairwise transformation was composed with its previous transformation(s). The initial frame was used as reference image because it represents the beginning of the movement of interest. This composition process yields a final affine transformation matrix which describes the transformation applied between the moving and the reference image, as represented in Fig. 3.2 (top-axis).

Elastix was the toolbox used to implement this method [120, 193] and the used parameter file can be found in appendix A.

3.2 Data

In this section, a description of the 2D HST US data used for the validation of the HST US acquisition system and of the global strain estimation method is given.

2D HST US in-silico data

Due to the complex nature of US images, initial validation of US quantification methods is commonly performed using in-silico (computer simulated) data.

In this case, a simplified 3D model of a tendon, with physiologically plausible dimensions [86], was constructed in Matlab. Tendon components (tendon unit, tendon fascicles, and surrounding soft-tissue) were approximated using cylindrical shapes with 2 cm of height. Lowest intensity values were assigned

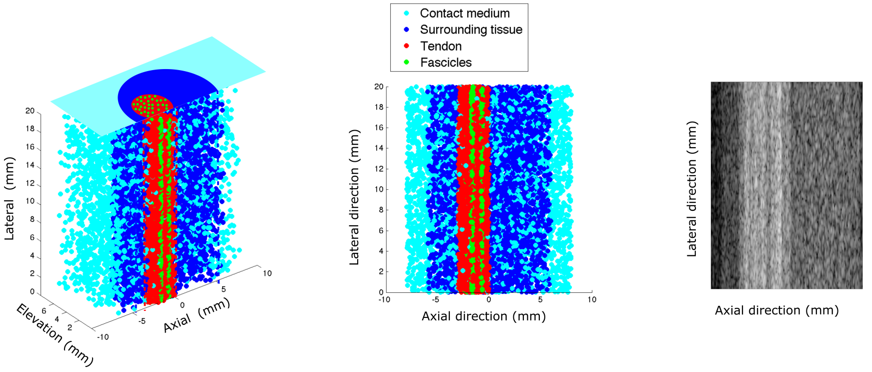

(a) (b) (c)

Figure 3.3: HST US simulation process. (a) represents a cross-section of the 3D model used to simulate 2D HST US images of tendon US images. (b) represents the selected central slab of points from the 3D model and (c) represents the 2D HST US image simulated from the slab of points.

to surrounding soft tissue points (cylinder radius of 4 mm). Medium and high-intensity values were allocated to tendon unit and tendon fascicles points, respectively. The tendon unit structure had a radius of 1.5 mm (dimension equivalent to a subtendon) and the constructed 95 fascicles had a radius of 0.1 mm each (dimension equivalent to a fascicle). Scatter points mimicking contact gel particles were added to the constructed model at random positions. Fig. 3.3(a) illustrates the 3D tendon model with its different components. This model presents also the three different directions used as reference throughout the rest of this work. The axial direction corresponds to the beam propagation direction of the US system, the lateral direction corresponds to the direction aligned with the US transducer's width, and the elevation direction corresponds to the US transducer's height.

The linear region of the tendon stress-strain curve was simulated, and a linear strain was applied along the lateral direction of the US system. This deformation was obtained by displacing the scatterers along the strain direction and towards the center of the volume. The applied lateral strain was simulated within a realistic physiologic range of 0% to 2% strain with incremental intervals of 0.25% strain resulting in one undeformed model and eight deformed models. Contact medium points were randomly positioned for each strain value.

Strain was estimated using an elliptic cylinder volume preservation equation $V = \pi * Dsmall * Dlarge * L/4$, where $Dsmall$ and $Dlarge$ correspond to the axis lengths of the base of the ellipse and L corresponds to the height of the cylindrical shape.

A 3D slab of points (example is presented in Fig. 3.3(b)) from the center of the 3D model was selected from undeformed and deformed models. This slab had a dimension of [12,20,2.8]mm along the axial, lateral and elevation directions. The thickness of the slab was defined according to the height of the US transducer elements. Each 3D central slab of points, from deformed and underformed models, was then given as input to a commonly used *US simulation platform* called *Field II* [105, 104]. Field II is a program for the simulation of ultrasound transducer fields and ultrasound imaging which uses linear acoustics, more specifically the Tupholme-Stepanishen method, for the calculation of the pulsed ultrasound fields [105, 104]. Simulation parameters were chosen to optimally mimic the used Vevo 2100 US system (see section 2.2.1). In the end, a simulated 2D HST US slice was obtained for each of the eight differently deformed models. An example of a 2D HST US in-silico image is given in Fig. 3.3(c).

2D HST US isolated tendons data

Three fresh isolated sheep tendons (institutional and national guides for the care and use of laboratory animals were followed - P065-2013) were initially preconditioned with cyclic stretches at a frequency of 0.5 Hz to 2% strain for ten cycles using a uniaxial tensile test device, also called *tensiometer* (ZwickiLine Prüfmaschinen Z0.5-Zwick-Roell, Ulm, Germany). Before each test, seven minutes of rest were given to the samples [152, 35, 34]. After the specimens preconditioning, these tendons were strained between 0% and 5% of strain.

Figure 3.4(a) illustrates a schematic representation of the mounting of the isolated tendon in the uniaxial tensile test device (ZwickiLine Prüfmaschinen Z0.5 - Zwick-Roell, Ulm, Germany). The coupling of an extensometer (MTS 634.12, MTS systems corp., MN, USA), used for validation purposes, to the tendon is also illustrated in Fig. 3.4(a). Each specimen was strained twice in an identical fashion. Simultaneously, 2D HST US images were acquired, at a *frame rate of 100fps*, with the transducer aligned with the central axis of the tendon along the elevation direction and placed equidistantly between the moving and the fixed clamping systems. Gel was applied in abundance to avoid loss of contact. For this image acquisition, the 2D HST US acquisition system described in section 2.2.1 was used.

Two ground-truth sources were used in this part of the work. One of the datasets was obtained from the grip-to-grip distance of the tensiometer, and the other was obtained from the gage-length of the extensometer. The strain was afterwards calculated using both tensiometer initial and final grip-to-grip distance and

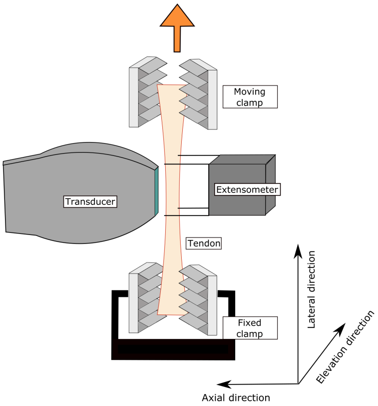

(a)

Figure 3.4: Example of acquisition setup for 2D HST US isolated tendons data. For this acquisition, the transducer was aligned with the central axis of the tendon. An extensometer was also coupled to the tendon.

extensometer initial and final gage-length distance with the engineering strain equation (eq. 1.2).

3.3 Validation of 2D global strain estimations

In this section, the statistical methods used for evaluating the performance of the developed 2D global strain estimation method are presented. Afterwards, the results obtained for the 2D global strain estimations of in-silico and isolated tendons data are presented.

3.3.1 Analysis

In the first instance, obtained results were compared with ground-truth values using the Pearson correlation coefficient [154, 37, 123, 94, 35, 169]. This type of measurement is commonly used for strain estimation validation, and it determines the strength of the relationship between calculated and ground-truth strain values. Results were found to be significant when the obtained alpha level was below 0.05.

Additionally, the mean absolute error (MAE eq.(3.20)), mean relative error (MRE eq.(3.20)), mean absolute deviation (MAD eq.(3.20)) and normalized squared error (NSE eq.(3.20) [26]) were also computed.

$$MAE = \frac{1}{n}\sum_{i=1}^{n} |\varepsilon_{Est} - \varepsilon_{GT}| \qquad MRE = \frac{1}{n}\sum_{i=1}^{n} \frac{\varepsilon_{Est} - \varepsilon_{GT}}{\varepsilon_{GT}}$$

$$MAD = \frac{1}{n}\sum_{i=1}^{n} |\varepsilon_{Est} - \overline{\varepsilon_{Est}}| \qquad NSE = \left(\varepsilon_{Est} - \varepsilon_{GT}\right)^2 / \varepsilon_{GT} \tag{3.20}$$

where ε_{Est} is the estimated strain, $\overline{\varepsilon_{Est}}$ the mean estimated strain and ε_{GT} the ground-truth strain.

The statistical power of the performed statistical analysis was calculated using G*Power 3.1 (Statistical power analysis program, Heinrich Hein, Universität Düsseldorf, 2014) [71, 70].

Estimated strains were derived from the affine transformation whereas ground-truth strains were retrieved from the deformation mechanisms (i.e. simulation model, tensiometer and extensometer).

3.3.2 Results

In this section, the performance of the global strain estimation method for both 2D HST US in-silico and isolated tendons data is presented.

Performance of global strain estimations using 2D HST US *in-silico data*

2D strain estimation correlation plots showed a high correlation (1 and 0.99) between the ground-truth values and the estimated values (Fig. 3.5). For this type of data, a MAE of 0.29%, a MAD of 0.59% and a NSE of 0.08% were obtained along the lateral direction (table 3.1). A MRE of ≈ 29% was also obtained for this experiment.

Performance of global strain estimations using 2D HST US *isolated tendons data*

Regarding the evaluation of the 2D HST US isolated tendons data, two different ground-truth sources were used. One type of ground-truth values was obtained

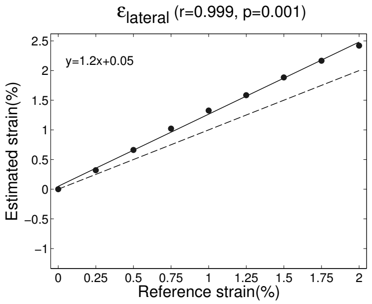

Figure 3.5: Representation of scatter plots for 2D in-silico data strain estimations along lateral direction. The dashed line represents the line of identity and the solid line represents the linear fitting to the data.

Table 3.1: Mean absolute error (MAE), mean relative error (MRE), mean absolute deviation (MAD) and standard deviation normalized squared error (NSE) for 2D global strain estimations for 2D in-silico and isolated tendons data. Global strain estimations are compared to the two different types of ground-truth. Errors are presented in %.

	2D HST US in-silico				2D HST US isolated tendons vs tensiometer				2D HST US isolated tendons vs extensometer			
	MAE	MRE	MAD	NSE	MAE	MRE	MAD	NSE	MAE	MRE	MAD	NSE
$\overrightarrow{lateral}$	0.29	28.28	0.59	0.08	0.32	18.27	1.29	0.075	0.71	27.22	1.25	0.20

from the *tensiometer*, while the other ground-truth was obtained from an *extensometer* coupled to the tendon. When comparing the two different ground-truth sources, significant differences (two-tailed paired t-test, p=0.02) were obtained. Figure 3.6 represents the comparison between the two different ground-truths.

When comparing the estimated global strain with the tensiometer and extensometer ground-truths, a correlation coefficient of 0.97 and 0.96 was obtained, respectively.

The mean absolute global strain values obtained for the three specimens (each specimen was measured twice) evaluated using only the tensiometer as ground-truth were 6.83%, 2.5% and 1.8%, respectively (Fig. 3.7(a)). The MAE, MAD and NSE for this experiment were respectively 0.32%, 1.29% and 0.075% as presented in table 3.1. When using the extensometer, the two tendons evaluated showed an absolute global strain value of 4.64% and 5.20% (Fig. 3.7(b)), and

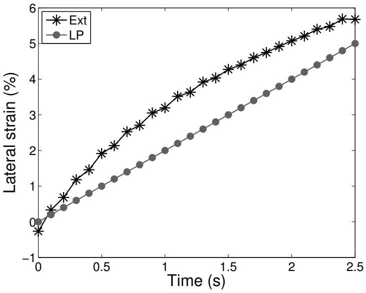

(a)

Figure 3.6: Example of different ground-truth data obtained using a tensiometer (LP) and an extensometer (Ext).

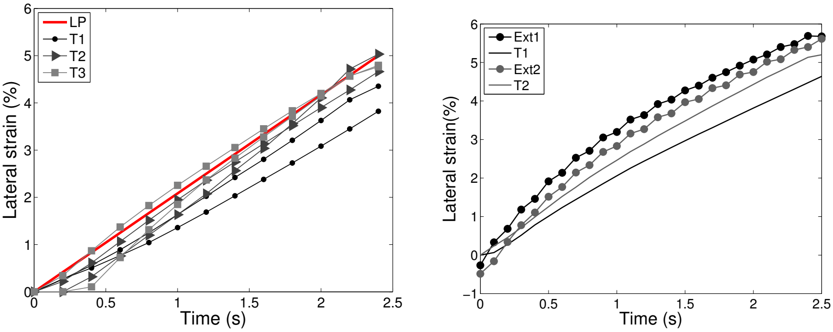

(a) (b)

Figure 3.7: Representation of obtained results for isolated tendons data using a tensiometer (LP) (a) and an extensometer (Ext) (b) as ground-truth data. Different tendons are identified by different T indexes.

a MAE, MAD and NSE of 0.71%, 1.25% and 0.20%, respectively as shown in table 3.1. For the tensiometer experiments, a MRE of $\approx$ 18% was obtained while for the extensometer, a MRE of $\approx$ 27% was obtained.

3.4 Discussion

In this section, an analysis of the results obtained for global strain estimations using 2D HST US data is presented.

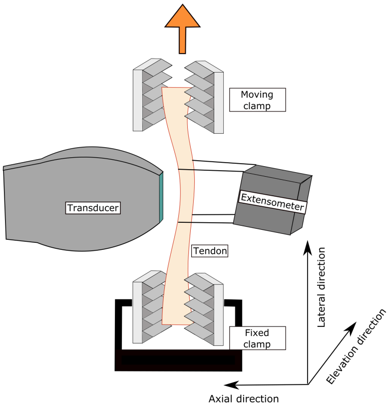

(a)

Figure 3.8: Illustration of the possible "bending" of the tendon due to the weight of the extensometer. The bending is exaggerated for illustration purposes.

3.4.1 2D HST US *in-silico* global strain estimations

As expected, in-silico data presented *high correlation* with ground-truth value and low estimation errors. However, when evaluating Fig. 3.5, an increment of strain estimation error linear with the increase of the applied strain is visible. This increase in error is assumed to be indicative of propagation and accumulation of error, commonly observed when following a pairwise approach, due to the composition process of mapping all of the moving images to the reference image [148].

This type of error can be reduced by increasing the speckle correlation between paired images which can be achieved by using high-temporal acquisition frame-rates. This experiment shows also the *crucial importance* of the acquisition of 2D HST US images with *high-temporal resolution*, such as it is the case of images acquired using the Vevo 2100 at *100fps*.

3.4.2 2D HST US isolated tendons global strain estimations

Concerning results obtained for 2D HST US isolated tendons data, the first surprising result is found when comparing the two ground-truth sources. There are several reasons for the occurrence of such differences. The first reason is the possible "bending" of the tendon due to the weight of the extensometer (as presented in Fig. 3.8(b)). If this bending occurred, deformation does not occur only along the lateral direction, and out-of-plane motion can be introduced influencing the accuracy of the strain estimations. One other reason for the found ground-truth differences concerns what is actually being measured. In first instance, it is possible that the extensometer is estimating the deformation of the epitenon or of a superficial thin fat layer rather than the deformation of the whole tendon. Secondly, it is also possible that the captured difference corresponds to different distributions of strain in different regions of the tendon.

At last, the obtained tendon strain estimation errors using isolated tendons data can as well be related to the out-of-plane motion. This type of artifact affects every 2D imaging acquisition system and occurs when tissue moves inside or outside of the field of view of the acquisition system. Out-of-plane motion has been commonly pointed out as a possible source of tendon strain estimation errors [34, 26, 168, 176, 204, 6]. However, contrary to those studies which used conventional ultrasonography, it is believed that the use of a *HST US system*, is beneficial for the *reduction of out-of-plane motion* strain estimation errors. Evidence of this advantage can be seen when comparing in-silico and isolated tendons experiments. Although strain estimation using US isolated tendons data is intrinsically more challenging (as described above) than when using in-silico data, equivalent or lower relative strain estimation errors were obtained. This may then be related with the fact that for in-silico data, the strain increment between consecutive images was 0.25% strain, while for isolated tendons data, the strain increment between consecutive images was 0.04%, which leads to higher speckle correlation between consecutive frames.

3.4.3 Comparison with state-of-the-art

The obtained results were compared with the results reported by Chernak-Slane *et al.* [35]. In this work, Chernak-Slane *et al.* [35] evaluated the performance of three different types of data (RF-data, B-mode data, and digital image correlation data) with three different image processing methods for the estimation of isolated tendons global tendon strain. The reported global strain estimations mean absolute errors (MAE) for the RF-approach, B-mode approach and digital image correlation approach were 1.8%, 2.5% and 1.4%, respectively. As table 3.1 shows, the MAE obtained with the developed method was 0.32% or 0.71%, for tensiometer and extensometer respectively, demonstrating thus the better performance of the developed method. The mean relative error (MRE) estimations for these three methods were 45% for the RF-approach, 62.5% for the B-mode approach and 35% for the digital image correlation (DIC) approach. Also for the MRE, the developed method presented lower estimations of 18.27% and 27.22% for tensiometer and extensometer, respectively.

Fröberg *et al.* [81] used a commercial speckle tracking method, EchoPAC 110.1.2 (GE Healthcare), to quantify isolated tendons global tendon strain. The ground-truth for this work was obtained from a tensiometer device. In this study, Fröberg *et al.* [81] found mean absolute errors (MAE±std) with a mean absolute deviation (MAD±std) of 0.70%±0.65% and of 10%±3.40% for isolated tendons data. When comparing our results with the estimations of Fröberg *et al.* [81], the developed method returns equivalent MAE and larger MAD compared to their best estimation (0.70%±0.65%) and the developed method has a better performance than their worst estimation (10%±3.40%).

3.4.4 Limitations

The presented work has two main limitations. The first one is related to the *insufficiently accurate, over-simplified ground-truth* values and *low sample size* used for the validation step. This inaccuracy was reflected by the different ground-truth values obtained from the tensiometer and the extensometer. Better validation of the developed method can only be obtained if a more accurate ground-truth measurement is used. However, the other commonly used validation approaches for isolated tendons experiments are either invasive [155, 9, 53, 125], involving the stitching of markers on the tendon or their insertion in the tendon which would disrupt the tendon, or are based on surface analysis techniques [206, 56, 166, 35], such as digital image correlation, which measures the tendon surface deformation rather than the tendon tissue deformation.

The second main limitation refers to the attempt in quantification of global tendon mechanics while using a model in which the tendon is *physiologically unrealistically* stretched and the clamping of the same is also *artificial*, which may in turn, produce deformation patterns different than the ones occurring in-vivo.

3.5 Concluding remarks

Results obtained for the *in-silico and isolated tendons data* show a *good performance* of the developed image registration method for global strain estimations. Furthermore, this good performance demonstrates also the feasibility of the use of the HST US acquisition system for tendon imaging.

When evaluating the global strain estimations for *isolated tendons data*, a *good correlation* was found between results of both *tensiometer* and *extensometer*.

Equivalent or lower mean relative strain estimation errors were also found for isolated tendons data in comparison with in-silico data. Although surprising, it was hypothesized that the low strain estimation errors found for isolated tendons data were associated with the higher temporal image resolution used for the acquisition of these images, in opposition to the lower temporal resolution used for the acquisition of in-silico data.

The comparison of the obtained results with the work of Chernak-Slane [35], which is a reference work in the field, shows a tendency towards the improvement of isolated tendon global strain estimations results. This tendency can be due to the use of different imaging systems in each work, being the acquisition of conventional (10MHz) vs. high-frequency (21MHz) US images and the acquisition at lower (56fps) vs. higher (100fps) temporal resolution. The improvement found can also be due to the different global strain estimation approach used in each method (RF-based method vs. image registration approach).

Considering the results obtained for the comparison between in-silico and isolated tendons data and the improvement of the strain estimation errors in comparison with the literature, it is believed that the acquisition of *high-temporal resolution* images is of *crucial importance*. Notwithstanding, it is also believed that the combination of high-temporal and high-spatial resolution data with the developed image registration method, fine-tuned for this type of data, contributed as well to the reduction of tendon strain estimation errors.

In conclusion, the obtained results allow, firstly, the validation of the developed 2D HST US global tendon strain estimation method with improved performance, when compared with the literature; and secondly, the validation of the 2D HST US acquisition system for the imaging of tendons.

Chapter 4

In-vivo characterization of local tendon biomechanics using 2D high-spatial and high-temporal resolution US data

Contents

As mentioned before, the main goal of the presented manuscript is the implementation of a high-spatial and -temporal resolution (HST) ultrasonography system for in-vivo quantification of tendon biomechanics and the evaluation of the potential of this imaging modality for clinical applications. Due to the novelty of such HST US acquisition system, an initial validation of this acquisition system was required. This validation was obtained by comparing 2D global strain estimations of in-silico and isolated tendons data with known ground-truth (chapter 3). The results obtained for 2D global strain estimations for both in-silico and isolated tendons data showed good correlation and a reduction of strain estimation error when compared with a reference work [35]. However, a more extensive validation of the 2D global strain estimation method was compromised due to uncertainties in the ground-truth measurements. Furthermore, 2D global strain estimation approaches have been shown to yield very limited clinical information about the tendon biomechanics. Alternatively, convincing evidence describing *local tendon deformation* has been published [225, 146, 191, 33, 137, 12, 196, 24] and it has been hypothesized that the characterization of local tendon biomechanics is fundamental for a better understanding of the functional role of healthy tendons. Once the biomechanical properties of healthy tendons are better understood, it is hypothesized that the pathogenesis of Achilles tendinopathies can also be better understood.

After considering the ground-truth limitations for 2D global tendon strain estimations of isolated tendons data and the increased interest in in-vivo quantification of local tendon biomechanics, it was decided to investigate the implementation of the HST US acquisition system for the in-vivo characterization of local tendon biomechanics. Moreover, the potential applicability of this HST US acquisition system for the clinical practice was also investigated.

The first section of this chapter describes the image registration method developed for the in-vivo characterization of the tendon biomechanics.

Afterwards, the different types of in-vivo data acquired for this work, which include asymptomatic and symptomatic tendons, are described. After the definition of the image registration framework used for the in-vivo characterization of local tendon biomechanics and the type of acquired data, the KULTeC application is explained. KULTeC stands for KU Leuven Tendon Characterization application and allows the selection, processing, and visualization of the features used to describe the in-vivo local tendon biomechanics. Unfortunately, ground-truth for the characterization of local tendon biomechanical is not available. This unavailability is due to the local nature of these measurements, the desire of maintaining the tendon's condition (no invasive measurements) and the interest of quantifying local tendon biomechanics in-vivo. Due to the absence of ground-truth, the validation of the developed method and obtained results is performed according to a psychometric approach [214]. Four different validity tests being: predictive, convergent, discriminant and concurrent validity tests were designed. The results obtained for the characterization of the local tendon biomechanics using the developed image registration method are then grouped according to the type of validity test which was performed on them. At the end, the concluding remarks of the in-vivo characterization of local tendon biomechanics are presented together with the limitations of the presented framework.

4.1 Deformable image registration approach for in-vivo characterization of local tendon biomechanics using 2D high-spatial and high-temporal resolution US data

Identical to the global strain estimation approach presented in chapter 3, the method developed for the in-vivo characterization of local tendon biomechanics also follows an image registration approach. However, a *deformable image registration* is preferred over the previously applied affine image registration, because the first allows the characterization of *local* rather than *global* tendon biomechanics. The fundamental difference between the deformable and affine image registration approaches is that deformable methods allow the maximization of the similarity between sub-regions of the reference and moving images while the affine approach computes a global transformation that maximizes the similarity between the reference and the moving image.

When image landmarks are available, thin-planes splines methods [25] are commonly applied to recover these nonrigid transformations. However, for intensity-based problems, the nonrigid components of the transformation can be estimated using a linear combination of polynomial terms [223, 224], basis functions [79], or B-spline surfaces defined by a regular grid of control points [187]. Alternatively, methods which mimic physical phenomena, such as elastic deformation and fluid flow methods, can also be used.

The transformation τ determined by nonrigid registration methods can be understood as a deformation field, which records at each pixel, the displacement vector required to align image B (moving image) with image A (reference image).

As mentioned above, thin-plane splines are used when image landmarks are available which is not the case for the images acquired for this work. On the other hand, deformable methods which optimize a similarity measure are preferred for this work (similarly to the method presented in section 3.1). A B-spline transformation is chosen to model the local deformations of the Achilles tendon because of its local-support, and its computational efficiency, even for a large number of control points. Equation 4.1 describes the cubic B-spline formulation:

$$\tau_{\mu}(y) = y + \sum_{y_k \epsilon N_y} p_k \beta^3 \left(\frac{y - y_k}{\sigma} \right) \tag{4.1}$$

with y_k being the control points, $\beta^3(y)$ the cubic B-spline polynomial, p_k the B-spline coefficient vectors (the control point displacements), σ the control point spacing, and N_y the set of all control points within the compact support of the B-spline at y [187]. In this type of transformation, the control points are placed in a uniform grid and act as parameters of the B-spline. The spacing between these control points defines the locality of the transformation. The smaller the spacing, the more local deformations are obtained. The displacement of the pixels at non-control positions was obtained by cubic interpolation. At the same time, the resolution of the control points mesh defines the number of degrees of freedom, and the computational complexity of this B-spline transformation. A compromise between computational effort and model flexibility is typically accomplished by following a hierarchical multi-resolution approach [135]. According to Lee *et al.* [135], this multi-resolution approach is achieved by increasing the resolution of the control mesh along with the image resolution, in a coarse-to-fine fashion. Let $\Phi^1, ..., \Phi^L$ denote the hierarchy of control meshes at different resolutions, where the spacing between control points decreases from Φ^l to Φ^{l+1}, hence the resolution of the control points increases. Each control point Φ^l and the associated B-spline define a local transformation τ^l_{local} at each resolution level and their sum defines the local transformation:

$$\tau_{local} = \sum_{l=1}^{L} \tau^l_{local} \tag{4.2}$$

As this equation shows, the local transformation is represented as a combination of B-splines at increasing resolution of the control point mesh. Similarly to the multi-resolution approach followed for the affine transformation, also 3 resolutions were used for the B-spline transformation.

The grid spacing schedule used consisted of halving of the control points spacing in every resolution step ($\Phi^3 = 4$, $\Phi^2 = 2$, and $\Phi^1 = 1$). To apply this control spacing schedule, a final grid spacing of 16 pixels was selected leading to a resolution at: Φ^3 of 1.28mm and 5.76mm, along axial and lateral direction; at Φ^2 of 0.64mm and 2.88mm, along axial and lateral direction; and at Φ^1 of 0.32mm and 1.44mm, along axial and lateral direction. In practice, this multi-resolution scheme would allow the recovery of the deformation at the fascicle level, ranging from 1.28mm to $320\mu m$. The local support of the B-spline would then divide the tendon in ≈4 layers at the lower resolution, and ≈15 layers at the highest resolution, along the axial direction. Regarding the local support of the B-spline along the lateral resolution, at the lowest resolution level, the length of the tendon would be divided into ≈4 regions, and at the highest resolution, the tendon would be divided in ≈14 regions. The reason behind the choice of three resolutions for the processing of these images was due to the interest of registering larger structures at lower resolutions and improving the tracking results for smaller structures at higher resolutions.

In general, the local deformation of the Achilles tendon has been reported to present a smooth transformation [12, 80, 35, 196, 75, 197, 77]. However, the optimization of nonrigid transformations is an ill-posed problem, which results in ill-conditioning, instability of solutions and a highly non-convex cost function [74]. Due to this ill-posedness, nonrigid registration problems are formulated differently than rigid registration problems, and consist in the optimization of a cost function which is defined by a similarity measure (S) and an added regularization or penalty term (P). This penalty term is intended to discourage undesirable transformations, such as high local stretching or bending, and folding [187, 17], or to constrain unfeasible solutions [74], as illustrated in equation 4.3.

$$
\begin{gathered}
\tau = arg \underset{\tau}{min} C(\tau; A, B), with \\
C(T; A, B) = -(\gamma_0 * S(\tau; A, B)) + \gamma_1 * P(\tau))
\end{gathered}
\tag{4.3}
$$

where γ_0 is the weight attributed to the similarity measure and γ_1 is the weight attributed to the penalty term.

The B-spline optimization problem was regularized by the magnitude of the Laplacian of the deformation, also known as the bending energy of the deformation, and defined in 2D as:

$$
p_{BE}(\mu) = \frac{1}{P} \sum_{\tilde{x_i}} \left\| \frac{\partial^2 \tau}{\partial x \partial x^\tau}(\tilde{x_i}) \right\|_F^2 \tag{4.4}
$$

$$
= \frac{1}{P} \sum_{\tilde{x_i}} \sum_{j=1}^{2} \left(\frac{\partial^2 \tau_j}{\partial x_1^2}(\tilde{x_i}) \right)^2 + 2 \left(\frac{\partial^2 \tau_j}{\partial x_1 \partial x_2}(\tilde{x_i}) \right)^2 + \left(\frac{\partial^2 \tau_j}{\partial x_2^2}(\tilde{x_i}) \right)^2, \tag{4.5}
$$

where P is the number of evaluated points $\tilde{x_i}$, and the tilde denotes the difference between a variable and a given point over which a term is evaluated [119]. Equal weights $\gamma_0 = \gamma_1 = 0.5$ were selected. Due to the absence of ground-truth, an visual assessment was used to establish the compromise between the regularity term and the similarity measure.

As for the chosen similarity measure, sum of squared intensity differences (SSD) was chosen for the same reasons as described in section 3.1. In summary, brightness constancy between speckle patterns obtained at two temporally close images is expected; the acquisition at high frame rates allows the acquisition of almost identical speckle patterns; this measure has been reported to perform better than correlation methods in ultrasound images which do not present large differences between both speckle intensity and geometry; and the computational efforts for correlation methods are higher than for SSD.

As for the chosen optimizer, the quasi-Newton limited memory BFGS was chosen because of its good performance for optimization of a large amount of parameters, which is even more important in B-spline transformations than in affine transformations.

Regarding the interpolation scheme used for this nonrigid transformation, a lower-cost interpolation (first-order B-spline) was used until the optimized transformation was close to the desired solution, being then replaced by a more expensive interpolation (third-order B-spline) in the last iterations.

Similarly to the global strain estimation, the method developed for the in-vivo characterization of local tendon biomechanics followed a pairwise, instead of a groupwise, strategy. Once the pairwise registration process was complete, each pairwise transformation was composed with its previous transformation(s). This composition process returned displacement fields that contained the spatial transformation along the axial and lateral directions between moving and reference image. Elastix was the toolbox used to implement this method [120, 193] and the used parameter file can be found in appendix B.

For the characterization of the local tendon biomechanics using the presented B-spline approach, the use of a mask is recommended. This mask was manually segmented and should contain only the tendon tissue. This recommendation is motivated by the different mechanical behavior, more specifically the average tissue displacement, of the different types of tissue present in the 2D HST US images of the Achilles tendon. Figure 4.1 presents a typical 2D HST US image of the Achilles tendon with the different tissues that surround the tendon. The relative tissue displacement of each of the tissues is illustrated by the arrows in Fig. 4.1. Relatively, skin is the type of tissue with the lowest deformation; the tendon has the medium deformation; and the tissue under the tendon has the largest deformation. Because of the included penalty term, if no mask was used, the abrupt deformation (shear) at the borders of the tendon would not be adequately tracked. Finally, and considering the use of a mask for the nonrigid registration, a random mask sampler was used to select the correspondence points at which the transformation is evaluated during the optimization process.

Overall, the selection of the different image registration parameters should not be only based on the individual performance of each, but on their performance as a whole due to the inter-connectivity present between them. Because of that, a sensitivity test comparing different image registration parameters is presented in section 4.5.1.

4.2 Feature estimation for characterization of in-vivo local tendon biomechanics

To characterize the local tendon biomechanics, several pre-processing steps were required. The initial step was to align the obtained displacement field (in the anatomical coordinate system) with the anatomical coordinate system (major deformation direction of the tendon). This conversion was performed by

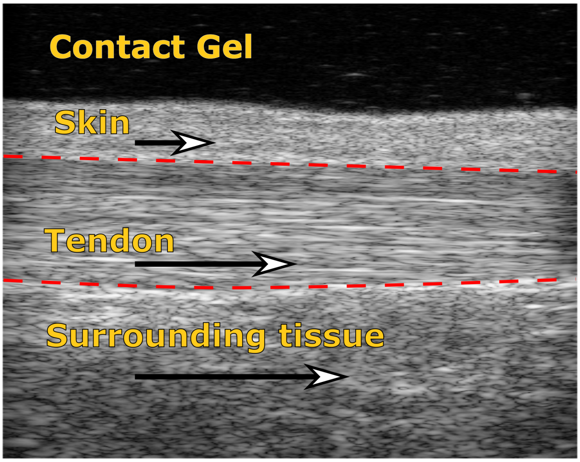

(a)

Figure 4.1: Example of 2D HST US in-vivo data. The arrows illustrate the relative difference of the absolute tissue displacement of each type of tissue.

projecting the obtained tissue displacement field from the Cartesian coordinate system onto the major tendon deformation direction. The angle used for this projection was estimated from the manually selected mask, which was used for the registration framework.

Besides the alignment of the obtained displacement field with the Cartesian coordinate system, also a *selection of sub-regions of interest* (sub-ROIs) was required. This sub-ROI selection served the main goal of allowing the estimation of local deformations within the tendon while reducing possible high variability estimations due to the scattering effect. Six sub-ROIS were defined at 25% and 75% along the lateral direction and 25%, 50% and 75% along the axial direction of the mask image used for the registration method. The positioning of these sub-ROIs was decided in consultation with the clinician in order to allow the evaluation of the tendon according to proximal or distal regions, as represented in Fig. 4.2(a), and according to three different tendon layers, being superficial, middle and deep, as represented in Fig. 4.2(b).

Local tendon biomechanics was evaluated using features that were calculated along the major deformation direction (lateral direction). These features, also defined as primary features, were the *local tendon tissue displacement* and the *regional tendon strain*. Both local tendon tissue displacement and regional tendon strain were estimated from the displacement field obtained from the composition process of the registration framework. *Tendon tissue displacement*

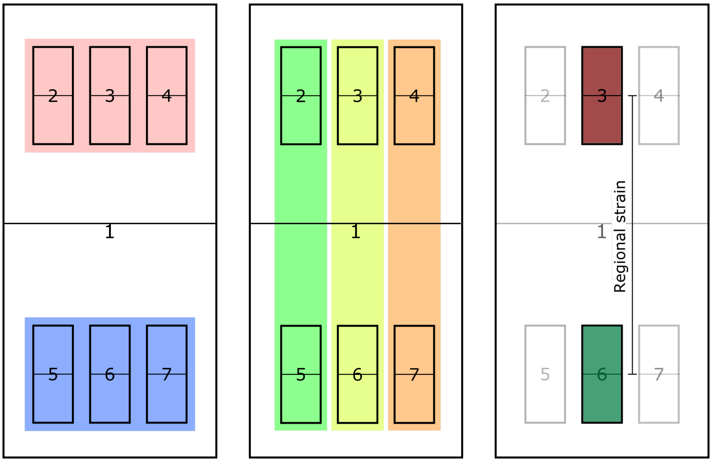

(a) (b) (c)

Figure 4.2: Sub-ROIs positioning. (a) proximal (pink, regions 2,3 and 4) vs. distal (blue, regions 5,6, and 7) sub-ROIs, (b) superficial (orange, regions 4 and 7), middle (yellow, regions 3 and 6) and deep (green, regions 2 and 5) sub-ROIs. (c) example of regional strain estimation(calculated between sub-ROI 3 and sub-ROI 6). Large region (1) corresponds to the mask selected for the image registration method.

estimations were calculated by averaging the displacement field values that were contained within each of the selected ROI and sub-ROIs. *Regional tendon strain* ($Regional\varepsilon$) was calculated using two different sub-ROIS, as illustrated by sub-ROI 4 and sub-ROI 7 in Fig. 4.2(c). The difference in average tissue displacement of each sub-ROI was computed and divided by the initial distance between these two sub-ROIs (see table 4.1).

Besides primary features, auxiliary features were also calculated. This type of features combines the calculated primary features by proximal/distal region as well as superficial/medial/deep layers of the tendon. Table 4.1 shows the calculated auxiliary features.

4.3 Data

The following two sections describe the acquisition of two different in-vivo datasets. The first dataset contained data from asymptomatic tendons repeatedly acquired at two consecutive days and the second dataset contained

Table 4.1: Estimated features for characterization of in-vivo local tendon mechanics

Primary features	
Mean tissue displacement	ΔRn
Regional strain	$Regional\varepsilon = -\dfrac{\overline{\Delta Ri} - \overline{\Delta Rj}}{C_{init}Ri - C_{init}Rj}$
Auxiliary features	
Mean prox/dist ΔRn	$\Delta prox$ / $\Delta dist$
Mean sup/med/deep ΔRn	ΔSup /ΔMed / $\Delta Deep$

Every feature was calculated along the lateral direction. Δ described tissue displacement and Rn, $1 < n < 7$ refers to the sub-ROIs. Ri, $i = 2, 3, 4$ are the distal sub-ROIs and Rj, $i = 5, 6, 7$ are the proximal sub-ROIs. C_{init} corresponds to the initial center position of certain ROI. *Prox/dist* correspond to the proximal and distal sub-ROIs, respectively, and *sup/med/deep* correspond to the superficial, medial and distal sub-ROIs, respectively.

images from volunteers with Achilles tendinopathies (denoted symptomatic volunteers).

For every test, the US acquisition system used was the Vevo 2100 with the 21 MHz central frequency transducer with an acquisition frame-rate of 100fps (described in 2.2.1).

2D HST US in-vivo asymptomatic data

Ten asymptomatic volunteers were recruited to perform the first in-vivo acquisition test. These asymptomatic volunteers have a mean age of 25 years (± 3.9 years) and a mean weight of 72 kg (± 13.4 kg). Informed consent (UZ Leuven ethics committee number s57302) was obtained from all of the participants. Participants were asked to fill in a document with demographic questions and a VISA-A questionnaire, which is a validated measure of tendon health and function [186]. Subjects with previous history of Achilles tendon rupture, surgery, and systemic or neuromuscular diseases were excluded. Participants were asked to refrain from intense physical activity the day before the experiments. The acquisition of 2D HST US data was done in two consecutive days at approximately the same time of the day.

For the 2D HST US acquisition, the volunteer lay prone on a table, knees extended, with the foot fixated in an isokinetic testing device according to the manufacturer's guidelines (Biodex system 4 PRO, Biodex Medical Systems, Inc., Shirley, New York). After a standardized warm-up of 5 repetitions of concentric plantar- and dorsiflexion was done, starting from a neutral position through 20° range of motion [152, 35, 34].

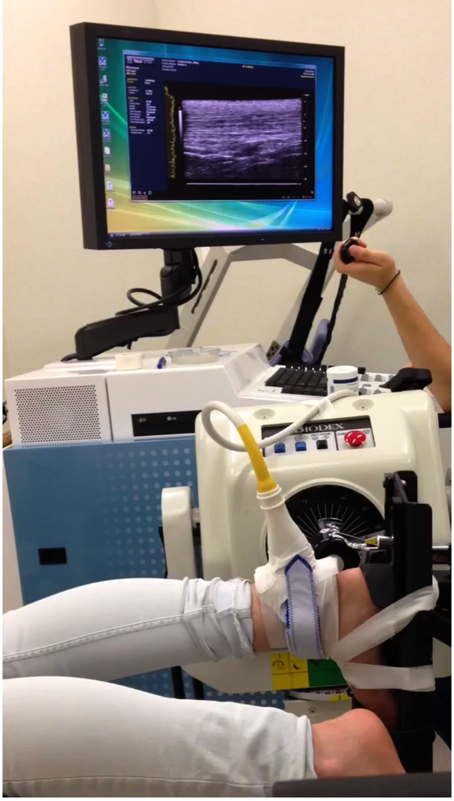

(a)

Figure 4.3: Example of acquisition of in-vivo asymptomatic 2D HST US images using a custom-made transducer holder. The foot was fixated to the Biodex device. Demo video is available in digital version

Two motions were used in randomized order between subjects and between days: 2 repetitions of maximal voluntary isometric contraction in a neutral ankle position during 5 seconds, and 2 repetitions of passive elongation from 10° plantarflexion to 10° dorsiflexion and back at 15°/sec.

The US transducer was aligned with the major deformation direction of the tendon and attached to a custom-made holder at Achilles tendon mid-portion, as represented in Fig. 4.3[1]. The position of the holder was marked on the skin with a marker to allow reproducible positioning on day two. A cine image, containing 500 frames, was acquired with a temporal frequency of *100 frames per second*.

Figure 4.4(a) shows an example of an asymptomatic 2D HST US image.

2D HST US in-vivo symptomatic data

For the acquisition of symptomatic data, eight symptomatic volunteers with Achilles tendon pathology were recruited from the consultation of physical and rehabilitation medicine at the UZ Leuven Hospitals. These symptomatic volunteers had a mean age of 45 years (± 17.85 years) and a mean weight of 76.6 kg (± 21.3 kg). Informed consent was obtained from all participants and participants filled in a document with demographic questions and a VISA-A questionnaire [186]. Also in this study, subjects with previous history of Achilles tendon rupture, surgery, and systemic or neuromuscular diseases were excluded.

The diagnosis of mid-portion Achilles tendinopathy was confirmed by clinical examination and diagnostic ultrasound. Cases of differential diagnoses (peritendinous changes, rupture, insertional changes, etc.) were excluded. Symptomatic subjects were classified based on two factors: (a) symptom severity, objectified using the validated VISA-A questionnaire [186]; (b) morphological appearance on gray-scale ultrasound, objectified using the Archambault score [10]. The Archambault score classifies a tendon as grade I, normal; grade II, enlarged tendon; and grade III, tendon containing a hypoechoic area, regardless of size. This classification resulted then in three groups which were: less severe tendinopathy group (C1), medium severe tendinopathy group (C2) and very severe tendinopathy group (C3).

For the acquisition of 2D HST US images, the previously used custom-made transducer holder was here reused. This holder was mounted so that the US transducer was aligned with the major deformation direction of the tendon. Also as before, a cine image containing 500 frames, was acquired at a temporal frequency of 100 frames per second.

For this study, two tendon activation exercises, equivalent to the ones applied for the acquisition of asymptomatic data, were performed. In summary, these two activation exercises consisted of a passive elongation of the tendon from 10° plantarflexion to 10° dorsiflexion and back at 15°/sec; and a maximal

---

[1] Video with an example of acquisition is available in digital version

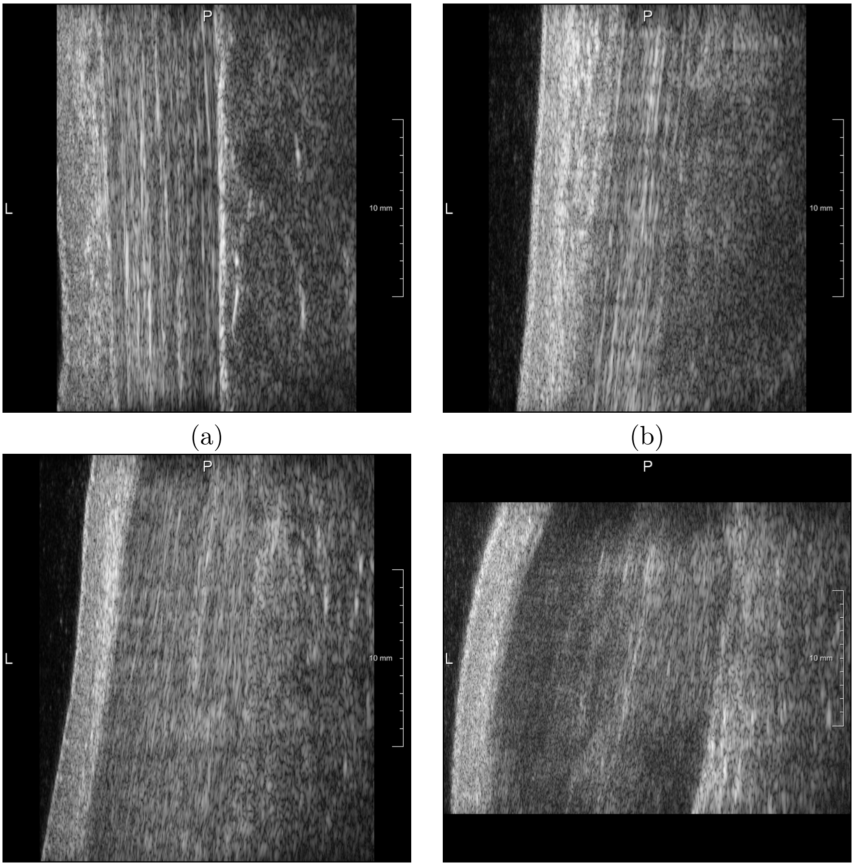

(a) (b)

(c) (d)

Figure 4.4: Example of an asymptomatic 2D HST US image (a), a 2D HST US image of a C1 tendon is represented in (b), a 2D HST US image of a C2 tendon is represented in (c), and a 2D HST US image of a C3 tendon is represented in (d).

voluntary isometric contraction in a neutral ankle position during 5 seconds. The acquisition of each type of exercise was repeated twice on both legs on a single day.

Figure 4.4(b) shows an example of a 2D HST US image of a C1 tendon, Fig. 4.4(c) shows an example of a 2D HST US image of a C2 tendon while Fig. 4.4(d) shows an example of a 2D HST US image of a C3 tendon.

Alternative 2D HST US in-vivo acquisition setups

Due to the inability to move the Biodex device and its large requirement of space, together with the strict limitations to the moving of the US acquisition system, initial in-vivo tests explored the applicability of electrical stimulation for the elongation of the Achilles tendon [153, 136, 155, 77, 67, 68]. In this experiment, the volunteer lay on a table and two electrodes where placed on its gastrocnemius muscle. Cycles of 5/5 seconds were used to stimulate/relax the tendon and a maximum of 34mA was used for the stimulation. Two young and active volunteers were scanned using the electrical stimulation protocol and both reported discomfort during the tests. Moreover, the elongation of the acquired tendons, when stimulated electrically, was too fast and of difficult control leading to improper data acquisition. Due to these reasons, this line of experiment was abandoned.

4.4 KULTeC - KU Leuven Tendon Characterization application

The developed deformable image registration method was then embedded in the KULTeC application to allow the use of the developed technology by the clinicians.

The KULTeC application is a three-modular solution that allows the pre-processing of the acquired 2D HST US images (KULTeC - Selection module), implementation of the developed deformable image registration approach for the processing of the pre-processed images (KULTeC - Offline processing module), and visualization of the results obtained for the in-vivo characterization of local tendon biomechanics (KULTeC - Visualization module). The KULTeC was implemented in Mevislab (Mevislab, version 2.6a, MeVis Medical Solutions AG, Bremen, Germany).

4.4.1 KULTeC - Selection module

The first module of the KULTeC application performs mainly pre-processing tasks such as the selection of a temporal interval of interest and region of interest from the cine images (asymptomatic and symptomatic datasets).

The first required pre-processing step is the selection of a temporal interval of interest from the cine images. As explained in section 4.3, the acquired 2D HST US images correspond to the acquisition of a certain tendon activation exercise and were acquired over a maximum period of 5 seconds. Taking as an example the passive elongation exercise, the movement from 10° plantarflexion to 10° dorsiflexion was estimated to last approximately 2 seconds and the inverse movement another 2 seconds. As a result, both plantar-to-dorsiflexion and dorsi-to-plantarflexion movements were stored in a single cine image. From a clinical perspective, the characterization of local tendon biomechanics for the plantar-to-dorsiflexion movement is more interesting than its counterpart because it shows the elongation of the tendon. Besides the clinical motivation, the selection of the interval of interest was also required due to computational reasons. Although the pairwise registration is not severely affected by the increase of the number of processed frames, the composition process is. This occurs because the interpolation between every pair of displacement fields is done subsequently. In order to maintain a reasonable processing time per image ($\approx$ 40min), the selection of an interval of interest containing 100 frames, corresponding to an acquisition of 1 second, was recommended.

The second required pre-processing step is the selection of a region of interest (ROI). This matter was already explained in section 4.1 where the benefits of having a mask, here designated as ROI, were explained. In summary, the use of a mask for the image registration process is recommended because, otherwise, the different absolute displacement values of the tissues surrounding the tendon could influence the performance of the image registration method negatively.

Both pre-processing steps can be accomplished by using the KULTeC - Selection module as explained below.

To perform the selection of the region and interval of interest, the username and the path to an image, preferably in NIfTI-1 format [55], are required. Figure 4.5(a) shows the application window where ① receives the path to the input image and ② takes the unique user identity.

Once an image is uploaded, the interval of interest can be selected using the panel of the temporal selection window (Fig.4.5(a)④). The selected interval of interest can then be reviewed using the play, stop and reverse buttons (Fig.4.5(a)③). After this selection, a default region of interest (ROI), also used as mask for the image registration process is presented (Fig.4.5(b)). This ROI can be stretched or contracted, rotated and displaced. Once the ROI is well placed, it can be saved and used for the automatic drawing of the six sub-ROIs by selecting "Draw sub-ROIS" (Fig.4.5(a)⑤) [2].

These sub-ROIs are used for the in-vivo characterization of local tendon biomechanics as described in section 4.2 and are drawn at 25% and 75% along

---

[2] Demo video is available in digital version

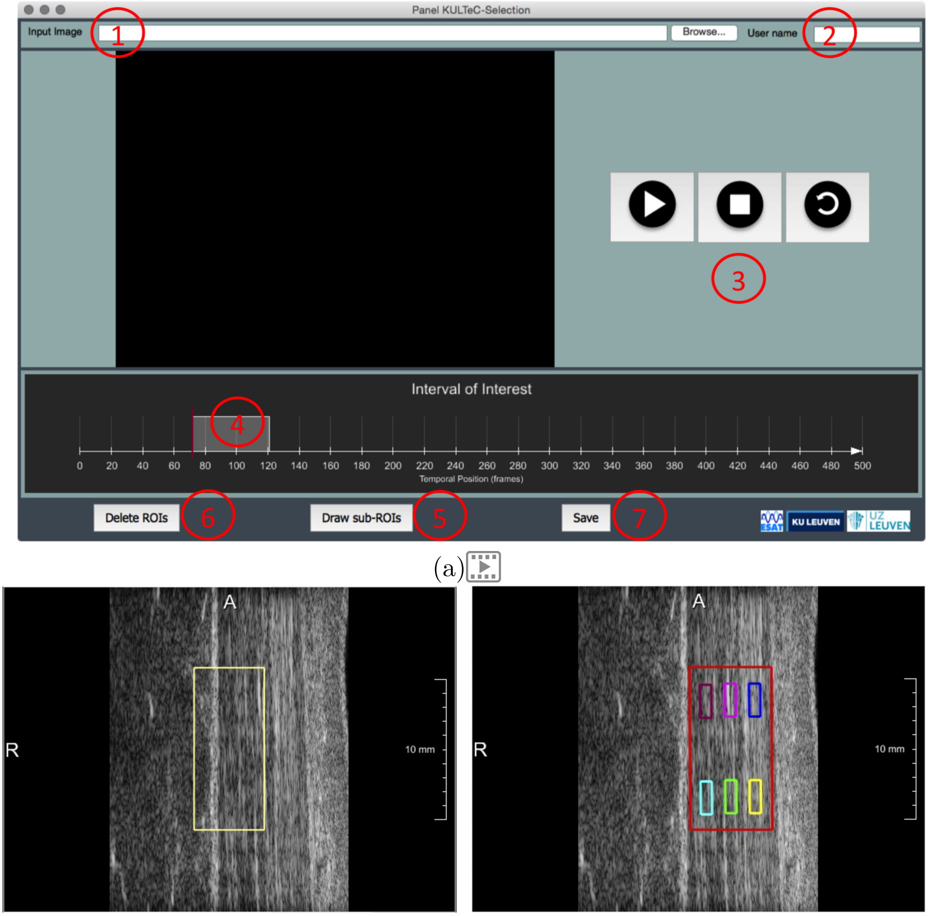

(a)

(b)

(c)

Figure 4.5: KULTeC - Selection module. Demo video is available in digital version

the lateral direction and 25%, 50% and 75% along the axial direction of the principal ROI (Fig.4.5(c)). If the drawing of these sub-ROIs is not satisfactory, they can be deleted by selecting "Delete ROIs"(Fig.4.5(a)⑥).

Once good quality interval of interest and ROIs are obtained, the button "Save" (Fig.4.5(a)⑦) saves the spatial coordinates of the region of interest and the temporal coordinate of the interval of interest in association with the processed patient to a database.

4.4.2 KULTeC - Offline processing module

After selecting the interval and region of interest on the previous module, consecutive 2D frames within the interval of interest are registered pairwise using the B-spline image registration method described before. The final results are obtained by composing the intermediate displacement fields to the initial frame.

Afterwards, the calculation of the primary and auxiliary features (equivalent to the ones described in detail in section 4.2) is performed to allow the characterization of the local tendon biomechanics and stored in the results databases.

Figure 4.6 describes the flowchart of the offline processing module generically. Modules in blue correspond to the given inputs and modules represented in green indicate the most important outputs.

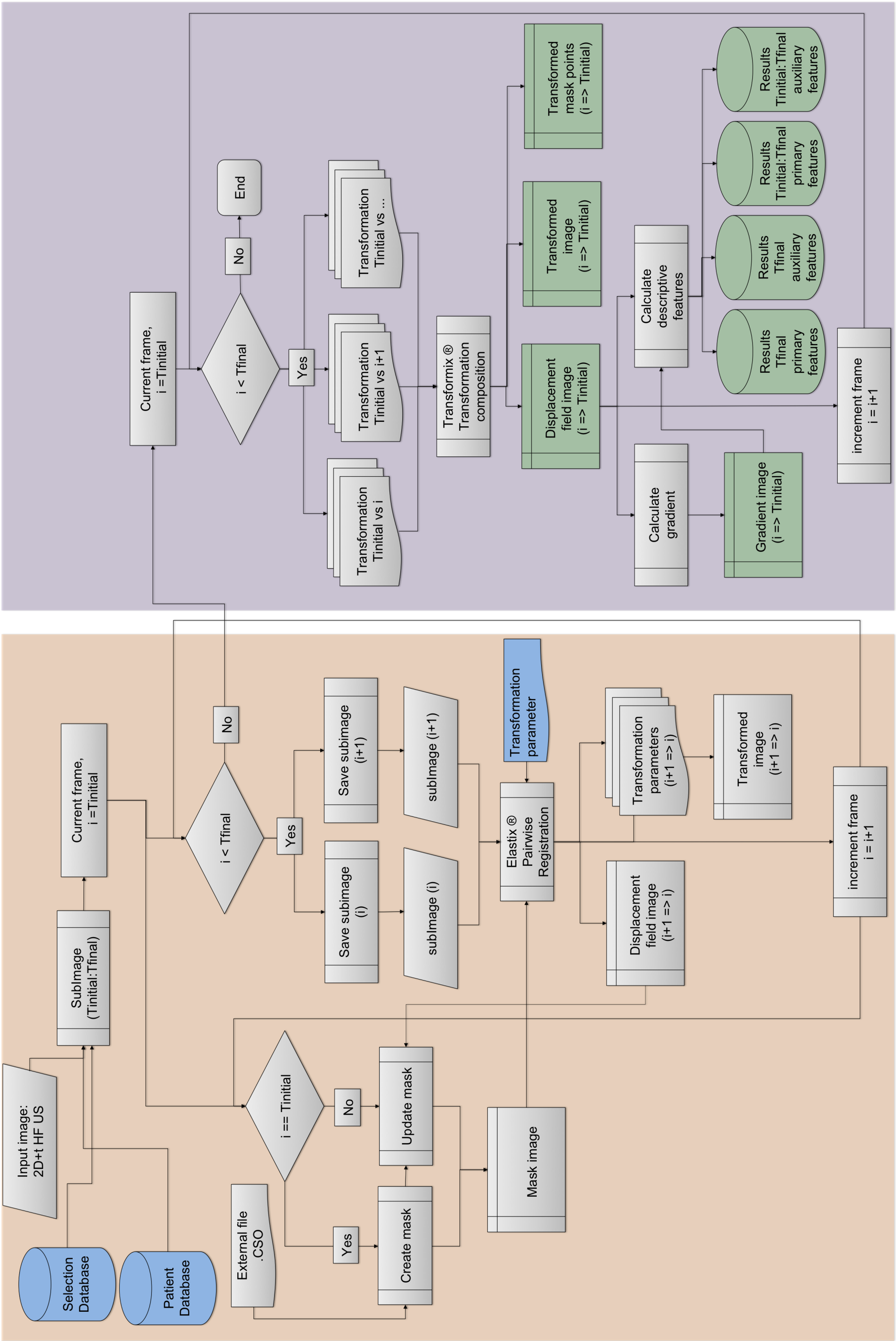

Figure 4.6: Flowchart of KULTeC- offline processing module. Blue modules represent the given inputs, and green modules represent the most important outputs. Orange rectangle illustrates pairwise registration process while purple rectangle illustrates the composition process.

In summary, the developed image registration framework can be divided into two main parts. The image registration part, corresponding to the orange rectangle, receives the pre-processed image and the information regarding the ROI and sub-ROIs. The initial step is the generation of a mask image, which uses the input provided by the user. Afterwards, the initial and consecutive frames are saved individually and fed, together with the mask image, and the B-spline transformation file to Elastix. Elastix outputs then a displacement field, corresponding to the spatial transformation between the two frames, and a transformation file containing the transformation applied between the two frames ("Transformation parameter"). Before the beginning of another pairwise registration, the position of the mask image is updated with the average displacement of the previously obtained displacement field image.

After the completion of the entire pairwise registration process, the composition part (illustrated by the purple rectangle) takes place. This composition process uses the subsequent "Transformation parameter" files, obtained from the pairwise registration process, to transform the multiple moving images into the reference image space. At the end, a displacement field image is obtained. The transformation between every moving image and the reference image (e.g. frame 1 vs frame 2 or frame 1 vs frame 100), is then contained in each of these displacement field images. The gradient of the displacement field is afterwards computed. In the end, the descriptive features (primary and auxiliary features) are computed and the results are stored in databases.

4.4.3 KULTeC- Visualization module

The last module, the KULTeC - Visualization module, allows the visual evaluation of the tracking results, a visual representation of the computed features, and it also allows the visualization of the displacement fields obtained from the composition process.

This module requires the uploading of the patient's database (Fig.4.7①) and the clinician username (Fig.4.7②). Once these two variables are given to the system, a list containing the processed images for the uploaded database is displayed (Fig.4.7③). When an item is selected in this list, the corresponding input image is represented in Fig.4.7⑤, ⑥, ⑦. On Fig.4.7⑤ the used ROI and sub-ROIs are overlaid to the input image, and each region is identified by a color. Each region is then represented in the plots with its corresponding color (Fig.4.7⑧, ⑨,⑩ and ⑪).

Light blue dots are represented as a regular grid on top of Fig.4.7⑤. These

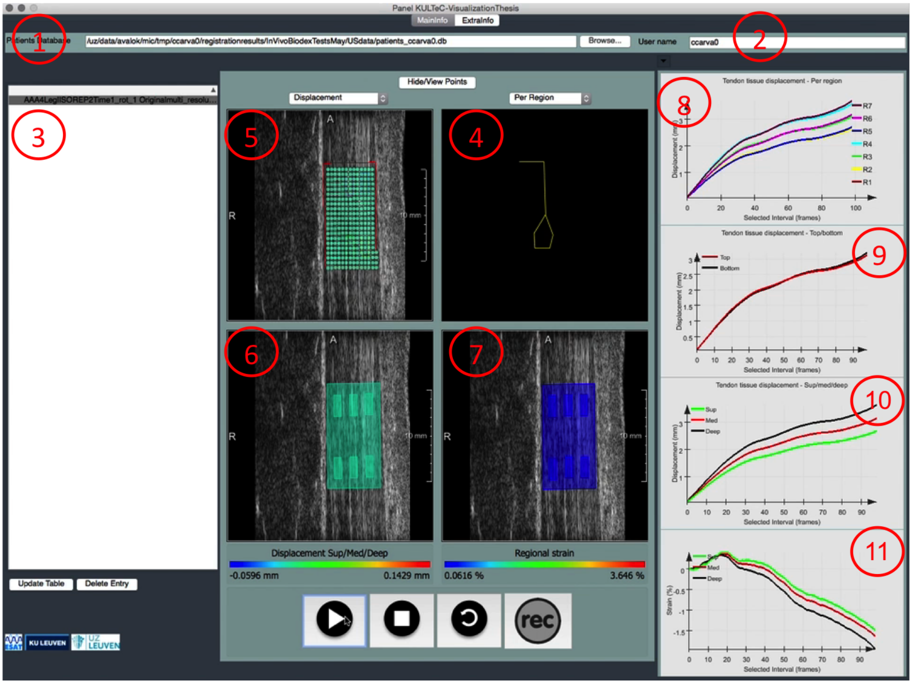

Patients Database: /uz/data/avalok/mic/tmp/ccarva0/registrationresults/InVivoBiodexTestsMay/USdata/patients_ccarva0.db

User name: ccarva0

(a)

Figure 4.7: KULTeC - Visualization module. Demo video is available in digital version

dots correspond to the transformation of a regular grid of points using the deformable image registration. Figure 4.7⑥ illustrates the tendon tissue displacement estimations according to the different layers and Fig. 4.7⑦ illustrates the calculated regional tendon strain according to the different layers as well. Fig. 4.7⑧, Fig. 4.7⑨, Fig. 4.7⑩ and Fig. 4.7⑪ present the calculated primary features (tendon tissue displacement and regional strain) and the auxiliary features (top/distal tendon tissue displacement and superficial/medial/deep tendon tissue displacement).

Fig.4.7④ shows a schematic representation of the performed tendon activation exercise.

4.4.4 Role of KULTeC

The KULTeC application had an important role in the in-vivo characterization of local tendon biomechanics. Every task, from region and interval of interest selection, image registration and results visualization, was implemented via this application. Furthermore, this application was developed in a manner that it could be easily and intuitively used by the clinicians.

One minute is the conservative estimation for the average time a clinician spends on the KULTeC - Selection module, while each 2D HST US image (100 frames) takes approximately 40 minutes to be registered and to calculate local tendon tissue displacement and regional strain. Although not real time, the presented solution can easily be applied in clinical trials where the need for fast diagnosis is less important.

4.5 Validation of 2D deformable image registration approach

Despite the absence of physiologically meaningful ground-truth for the validation of the obtained results, the used image registration approach was validated according to the:

- sensitivity of the estimated results to variations of the parameters used for the registration process;
- sensitivity of the estimated results to variations of the selection of the region of interest;
- inter-observer variability.

Due to time constraints, the dataset chosen for the validation of the developed image registration method was reduced. The size of the dataset used for the evaluation of the estimated results to variations to the image registration parameters and for the evaluation of the sensitivity of the estimated results to variations of the selected region of interest was 38 images. This set included 19 images from asymptomatic and 19 from symptomatic volunteers, randomly selected. The size of the dataset used for the evaluation of the inter-observer variability, was 8 images. This set included 4 images from asymptomatic and 4 images from symptomatic subjects, randomly selected.

The selection of the interval of interest (approximately 100 frames) was done in order to include both slow and fast movements as well as fast transitions of the direction of the movement. The default region of interest (ROI) was selected in the central region of the tendon. For each of the selected ROIs, six sub-ROIs were automatically drawn. The biomechanical features of the Achilles tendon evaluated during this validation step were equivalent to the ones presented in section 4.2.

4.5.1 Sensitivity of the estimated results to variations of the parameters used for the image registration process

For this validation step, sixteen different image registration parameter sets were used. These sixteen parameter sets were derived from the image registration parameters defined in section 4.1, from here on called *default parameters*. For sake of easy comparison, the default parameter set used was: sum of squared differences as similarity measure, the quasi-Newton limited memory BFGS optimizer, 3 multi-resolutions, a bending penalty of 0.5 and a random mask sampler.

Each of the sixteen different parameter sets were obtained by replacing the specific parameter (e.g similarity measure) from the default parameters (e.g sum of squared differences), by the new corresponding parameter (e.g normalized cross-correlation). All the other variables remained the same as in the default parameter set.

The different parameters used for the validation tests were grouped according to their category and are presented below:

- **similarity measure** - advanced normalized correlation, advanced Mattes mutual information and normalized mutual information;
- **optimization strategy** - adaptive stochastic gradient descent, CMA evolution strategy, standard gradient descent and conjugate gradient;
- **number of multi-resolutions** - 1, 6 and 9;
- **bending energy penalty** - 0.1, 0.9, 0.99999;
- **image sampler** - full and grid

After the definition of the different sixteen parameters, the thirty-eight images selected for this validation study were registered. The analysis of the sensitivity of the estimated results (tendon tissue displacement and regional strain) to variations of the image registration parameters was quantified using a two-tailed paired t-test between the results obtained for the default parameter and the results obtained using the other sixteen parameters. The statistical power of this evaluation was calculated using G*Power 3.1 (Statistical power analysis program, Heinrich Hein, Universität Düsseldorf, 2014) [71, 70]. In this tool, the post hoc analysis of the computed two-tailed paired t-test was estimated using an effect size, computed via the mean and standard deviation of the differences of the results obtained using the compared parameters; a probability of error of 0.05% and a sample size of 38 were used.

From the 16 parameters used for the image registration process, four parameters (adaptive stochastic gradient descent, CMA-ES, standard gradient descent and 9 multi-resolutions) were inadequate and yielded registration errors. Two other parameters (conjugate gradient and adaptive stochastic gradient descent) did return misregistration results. Two examples of these results are presented in Fig. 4.8. Figure 4.8(a) corresponds to the registration results using the conjugate gradient optimizer and Fig. 4.8(b) represents the results obtained using the adaptive stochastic gradient descent optimizer.

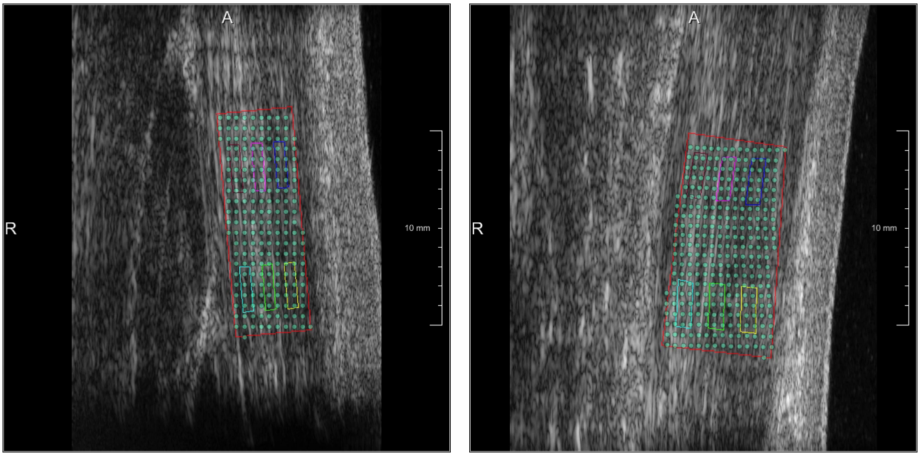

Figure 4.8: Example of misregistrations. Registration results obtained using the conjugate gradient optimizer (left image), and the adaptive stochastic gradient descent optimized (right image).

No significant differences ($p > 0.05$, $power > 0.99$) were found between the results obtained using SSD as similarity measure and normalized mutual information and between the results obtained using SSD as similarity measure and the results obtained using advanced mattes mutual information. However, significant differences were found between the results estimated using SSD as similarity measure and advanced normalized cross-correlation ($0.0024 \leq p \leq$

0.025, $power > 0.99$). After visual evaluation of the tissue motion tracking with both parameters, no obvious difference was visible. In order to understand these results, the absolute difference for the tendon tissue displacement estimations using both parameters is computed and a maximum difference of 0.17mm was obtained. Considering the pixel size along the lateral direction, which is the major direction of deformation, this difference corresponds to ≈ 2 pixels. Due to the small absolute value of this difference, it is believed that such difference does not affect the clinical interpretation of the obtained results. Due to the absence of ground-truth, the assessment of the more appropriate metric is not possible.

Significant differences ($0.007 \leq p \leq 0.024$, $power > 0.99$) were also obtained for the results using different image samplers. The default sampler was the *random mask sampler* and the biomechanical properties estimated with this sampler were compared with a *full sampler* and *grid sampler*. Significant differences were then obtained for the tendon tissue displacement estimates at the deep and superficial regions. Both full sampler and grid sampler select points on the full fixed image. In the case of the random mask sampler, random points are only selected within the mask. These different results can then be justified by the clear non-uniform deformation of the different tissues present in the acquired US images (skin, tendon and surrounding tissue). In this manner, when using points selected from the full fixed image, the regularization step will then smooth the deformation which occurs at the different tissues leading to registration errors at the boundaries: skin-tendon and tendon-surrounding tissue.

As for the different multi-resolutions tested, no significant differences ($p > 0.14$, $0.22 \leq power \leq 0.90$) were obtained when using 1 or 6 resolutions. Due to the low statistical power of these comparisons, few can be said about the results. Interestingly, this comparison was the only one of this validation test which presented such reduced statistical power. Theoretically, the use of multi-resolution approaches is beneficial for the optimization process and to correctly track the motion of the tendon. Because of this, it was initially expected that significant differences would be obtained for this test. The low statistical power obtained in this comparison allows the non-rejection of the benefits of multi-resolution approaches for the estimation of more accurate results.

Lastly, the use of different weights for the regularization also did not return significant differences ($p > 0.31$, $power > 0.97$). These results illustrate the intrinsic smooth deformation of the speckle patterns which does not seem to require much regularization.

In light of the absence of major significant differences between the default parameters and all the other parameters, the rest of this validation and this work makes use of the default parameters.

4.5.2 Inter-observer variability

For the evaluation of the inter-observer variability test, a supplementary graphical user interface (KULTeC - Ground-Truth module) was developed. This interface allowed the visual tracking of six different speckles, per image, and this tracking was performed by selecting an initial speckle and tracking it forward in time. At the end, both the initial and final position of the speckle were stored.

Two observers (Obs1 and Obs2) tracked six speckles per each of the 8 images selected for this validation study. The previously computed pairwise transformation files and the initial position of the selected speckles were then fed to Transformix, which is a program provided with Elastix that can be used to apply any transformation obtained by Elastix to any other image/points [120, 193], to obtain the estimated final position of the speckle. The evaluation of the performance of this transformation was obtained by calculating the Euclidean distance between the ground-truth and estimated final positions of the tracked speckles. Afterwards, a two-tailed paired t-test was used to investigate significant differences between the Euclidean distances (of the six speckles) obtained for each observer. The variability of these Euclidean distances obtained from each observer was expressed as the mean difference between estimations ± standard deviation.

No significant differences ($p = 0.16$, $power = 0.27$) were found between the obtained Euclidean distances of the two observers. However, a reduced power was obtained due to the very reduced sample size.

4.5.3 Sensitivity of the estimated results to variations of the region of interest selected

For the investigation of the sensitivity of the estimated results to variations of the selection of the region of interest, 38 ROIs and sub-ROIs were selected in 38 images. Afterwards, these ROIs and sub-ROIs were translated, in average, 1.8mm (9% of the full image width) along the lateral direction.

Also for this test, a two-tailed paired t-test was used to investigate differences between the biomechanical features estimated using the default and displaced ROIs. These differences were expressed as the mean difference between estimations ± standard deviation.

No significant differences ($0.11 \leq p \leq 0.98$, $0.05 \leq power \leq 0.35$) were found between the biomechanical features estimated using the two ROIs. However, the statistical power obtained for this analysis was lower, reducing the value of any conclusion using this data.

4.6 Validation of 2D in-vivo characterization of local tendon biomechanics

Due to the absence of ground-truth, four different validity tests, based on a psychometric approach [214], were used to validate the obtained results. The four validity tests, extensively discussed by Trochim *et al.* [214], were:

- Predictive validity test - which evaluated the reproducibility of the method developed for the in-vivo characterization of local tendon biomechanics. This reproducibility was evaluated using the asymptomatic dataset which was acquired at two consecutive days and repeated within each day with a few minutes apart;
- Convergent validity test - which evaluated the convergence of the results obtained by the developed method with the results presented in the literature. The convergent validity was evaluated for the asymptomatic dataset.
- Discriminant validity test - which evaluated the degree to which the developed method was not similar (diverged from) to the methods presented in the literature. Also the discriminant validity test was evaluated for the asymptomatic dataset.
- Concurrent validity test - which evaluated the ability of the estimated features to discriminate between asymptomatic and symptomatic tendons. This validity test used the asymptomatic and the symptomatic datasets;

This validation section describes the statistical tools used for each of the psychometric validity tests followed by the obtained results, also grouped according to each of the psychometric validity test performed on these results.

4.6.1 Analysis

In this section, the statistical tools used for each of the psychometric tests are grouped.

Predictive validity test

A predictive validity test assessed the method's ability to predict something it should, theoretically, be able to predict. A high correlation would provide then the evidence for the predictive validity[214].

The predictive validity test was done by evaluating the reproducibility of the developed method. As a measure of reproducibility, intraclass correlation coefficients (ICC) were measured using a mixed model approach using SAS University Edition. Mixed model analysis is a useful statistical tool when there is correlated data, as it is the case of repeated measures because this allows modeling a variety of correlation patterns. The term mixed model refers to the use of fixed and random effects [143].

The fixed effects of the mixed model approach used to evaluate reproducibility were the gender, leg, time (repeated acquisitions) and peak torque. The primary and auxiliary features calculated previously were the response variables with the subject being defined as a random intercept variable. Results were grouped by activation type (e.g. passive elongation or isometric contraction). ICC less than 0.40 corresponds to poor correlation, between 0.40-0.59 corresponds to fair correlation, between 0.60-0.74 corresponds to good correlation and between 0.75-1.00 to excellent correlation [39].

The asymptomatic dataset was used for this predictive validity test because this dataset contained images acquired twice within a day and between two days for the same patient.

Convergent validity tests

The convergent validity test evaluated the degree to which the estimated results were similar (converge) to the results obtained in the literature. This test was based on the hypothesis that the estimated results and the results from the literature should, theoretically, be similar.

In summary, the convergent validity test was evaluated by investigating the features commonly used in the literature [35, 12] for the description of the local tendon biomechanics. The commonly used features for this description are the differences in the tendon tissue displacement at each layer of the tendon (e.g. superficial, medial and deep). This difference in tendon tissue displacement is also called non-uniform tissue displacement. A two-sided paired t-test with α-level set at 0.05 between the different tendon layers was used to investigate the convergent validity.

The statistical power of the performed statistical analysis was calculated using G*Power 3.1 (Statistical power analysis program, Heinrich Hein, Universität Düsseldorf, 2014) [71, 70].

The asymptomatic dataset was used for this convergent validity test, and the obtained outcome was compared against the literature methods. Also, in this case, high correlations between the estimated results and the literature results, was evidence of convergent validity.

Discriminant validity tests

The discriminant validity test evaluated the degree to which the developed method was different from the methods developed in the literature and used to perform the convergent analysis [214]. It is however, important to understand that a powerful convergent validity analysis can only be performed when comparing results obtained from different (discriminant) methods.

Concurrent validity test

The concurrent validity test evaluated the ability of the developed method, more specifically of the estimated features, to distinguish between asymptomatic and symptomatic groups. The quality of the discrimination was then evaluated according to the power of the method for the discrimination between two groups that were very similar.

The discrimination between classes was measured with a mixed model approach using SAS University Edition. This model had the repetition of the measurement per leg, torque and class as fixed variables. The primary and auxiliary features calculated previously were the response variables with the subject being defined as a random intercept variable. Hypothesis tests for the significance of each of the fixed effects were the obtained output.

To investigate the effectiveness of the developed image registration method to discriminate between asymptomatic and symptomatic images, a receiver-operating characteristic (ROC) curve was also used [87]. This type of curve is created by defining cut-off values defined between the minimum and maximum estimations for a certain feature. In other words, these cut-off values are defined by successively considering broader and broader categories of abnormal conditions. At each of these threshold points, the true positive (TPR) and false positive (FPR) rates are evaluated and plotted in a graph. In the end, a curve is fitted through the obtained TPR/FPR points. This type of analysis describes the trade-off between the sensitivity, the fall-out (1-specificity) and the accuracy of the method. While the sensitivity of the method can be described using the TPR and the fall-out using the FPR, the accuracy of the method is measured by the area under the ROC curve. An AUC of 1 represents a perfect test whereas an AUC of 0.5 presents an ineffective test [87].

4.6.2 Results

The results section follows the same structure as the analysis section and the results are grouped according to the type of validity test (predictive, convergent, discriminant and concurrent) performed on them.

Predictive validity test

For the investigation of the reproducibility of the developed method, the dataset with asymptomatic volunteers was used. Local tissue displacement and the regional strain were the features used for this predictive validity test.

Figure 4.9(a) shows an example of tendon tissue tracking results for one asymptomatic volunteer during *passive elongation* while 4.9(b) represents the tendon tissue tracking results for a different asymptomatic volunteer during *isometric contraction*. Figures 4.9(a-left) and 4.9(b-left) show the estimated tendon tissue displacement and figures 4.9(a-middle) and 4.9(b-middle) illustrate the average tissue displacement per tendon layer. A maximum tendon tissue displacement of 3.52 mm was obtained for passive elongation and of 5.25 mm for isometric contraction. Figures 4.9(a-right) and 4.9(b-right) represent the regional strain per tendon layer. The maximum estimations obtained for regional strain were 0.59 % and 0.18 % for passive elongation and isometric contraction, respectively [3].

Intra-class correlation (ICC) coefficients, calculated with the mixed model approach, for tendon tissue displacement ranged from 0.64 to 0.94 on day one and from 0.21 to 0.92 on day two. For regional strain, the ICC coefficients range was 0.58 – 0.94 on day one and 0.21 – 0.93 on day two. Inter-day ICCs were overall low (< 0.6) for tendon tissue displacement as well as regional strain.

Table 4.2 shows the ICC results for passive and isometric activation for the in-vivo characterization of local tendon biomechanics (tendon tissue displacement and regional strain estimations) grouped by leg, acquisition moment and tendon layer.

---

[3] Tracking videos are available in digital version

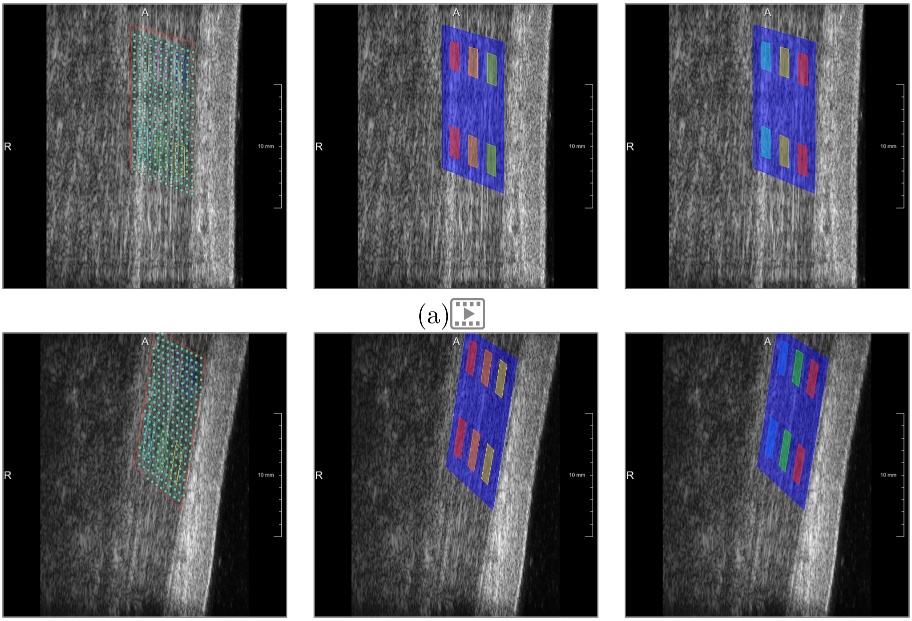

(a)

(b)

Figure 4.9: Tracking results for two different asymptomatic subjects during passive elongation (a) and isometric contraction (b). The left panel shows tracking results; middle panel represents average tendon tissue displacement estimations whereas right panel represents average regional tendon strain estimations along time. Tracking videos are available in digital version.

Convergent validity test

In this section, local tendon tissue displacement and regional strain estimations obtained by the method developed for the in-vivo characterization of local tendon biomechanics are presented. Afterwards, the results obtained by the state-of-the-art methods are also presented. In the end, a convergent validity test is performed by comparing the obtained results with the ones of the literature.

Non-uniform tendon tissue displacement of asymptomatic data is the feature commonly used for the characterization of the local tendon biomechanics [35, 12]. A paired t-test analysis was performed between the tissue displacement of each tendon layer (e.g. superficial vs. medial, medial vs. deep and superficial vs. deep) to investigate the non-uniform tendon deformation.

Table 4.2: ICC values for tendon tissue displacement and regional tendon strain estimations per layer. Results are grouped by activation type (passive or isometric), acquisition moment, leg and tendon layer.

	Tendon tissue displacement					
	Left leg			Right leg		
	Sup	Med	Deep	Sup	Med	Deep
PAS - day 1	0.94	0.92	0.85	0.72	0.68	0.72
PAS - day 2	0.92	0.74	0.75	0.21	0.38	0.50
ISO - day 1	0.78	0.71	0.64	0.79	0.81	0.72
ISO - day 2	0.6	0.62	0.63	0.73	0.77	0.82
	Regional tendon strain					
	Left leg			Right leg		
	Sup	Med	Deep	Sup	Med	Deep
PAS - day 1	0.75	0.75	0.73	0.94	0.94	0.94
PAS - day 2	0.93	0.91	0.90	0.64	0.56	0.40
ISO - day 1	0.87	0.87	0.89	0.77	0.68	0.58
ISO - day 2	0.91	0.88	0.89	0.21	0.27	0.34

Results obtained with the method developed for in-vivo characterization of local tendon biomechanics

Significant differences were found (using a paired t-test with a significance level of 0.05) when comparing the tendon tissue displacement of the three different layers during both isometric and passive exercises ($p<0.0001$) (Fig. 4.10(a)). A statistical power of ≈ 1 was obtained for the comparison, between each tendon layer, of the tendon tissue displacement estimations during passive elongation and isometric contraction. The deep layer of the tendon was found to move the most (3.03 mm) during passive elongation and 2.59 mm during isometric contraction.

Significant differences were also found for regional tendon strain when comparing all three layers, but only during passive elongation as represented in Fig. 4.10(b). A statistical power of > 0.92 was obtained for the comparison, between each tendon layer, of tendon tissue displacement estimations during passive elongation. The estimations of regional tendon strain were not found to be significantly different during the isometric trials. The highest regional strain was found in the superficial layer with an average of 0.33% during passive elongation.

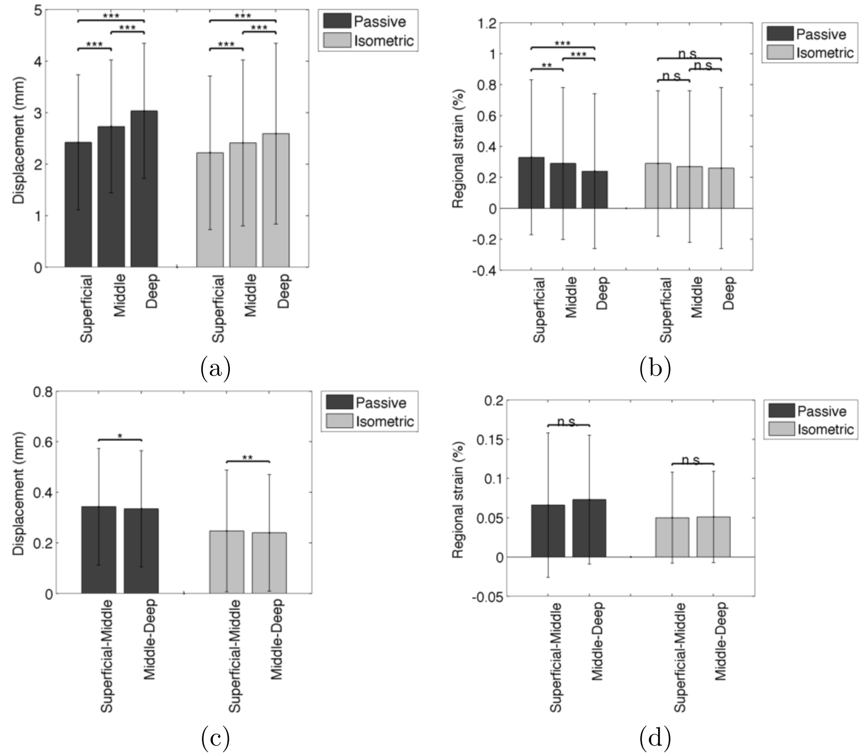

Figure 4.10: Significant differences and average values for (a) local tendon tissue displacement and (b) regional strain estimations for passive elongation and isometric contraction. (c) and (d) represent local tendon tissue displacement and regional tendon strain estimations between superficial/middle and middle/deep tendon layers, respectively. (** = p = 0.002 / *** = p < 0.001 / n.s. = non significant).

Significant differences were found for tendon tissue displacement estimation between superficial/medial and medial/deep during passive elongation and isometric contraction, as represented in Fig. 4.10(c). A statistical power of > 0.90 and 0.92 was obtained for the comparison, between each tendon layer, of regional tendon strain estimations per layer during passive elongation and isometric contraction, respectively. On the contrary, no significant differences were found for equivalent regional strain estimations (Fig. 4.10(d)).

Results reported in the literature for in-vivo characterization of local tendon biomechanics

Arndt *et al.* [12] and Slane *et al.* [196] found also significant differences of tendon tissue displacement estimations for the different layers of the tendon (superficial, medial and deep).

Both these studies found that the superficial layer had the lowest tendon tissue displacement estimations (8.4 mm±1.0 mm for Arndt *et al.* and 6mm±2mm for Slane *et al.*) and maximum tendon tissue displacement at the deep layer (10.4 mm±2.1 mm for Arndt *et al.* and 8.5 mm±3 mm for Slane *et al.*).

Concerning regional tendon strain estimations, the presented work is the first to report such type of estimations and due to that, no comparison is possible.

Discriminant validity test

For the evaluation of the discriminant validity test, the methodology and acquisition system used in the literature studies was compared with the methodology and acquisition system used in the developed method.

In first instance, the different imaging systems used in this work and the ones of the relevant literature [12, 196] were compared. 2D HST (20MHZ) and high-temporal (100fps) US data was acquired and processed in the presented work while Arndt *et al.* [12] acquired US data with a transducer with central frequency of 11MHz at 78.5fps, and Slane *et al.* acquired US data with a transducer with central frequency of 10MHz at 70fps.

Secondly, the tendon tissue displacement estimation approaches used in the three different methods was also different. The developed method followed a B-spline image registration approach based on B-mode data, the method applied by Arndt *et al.* [12] used an the automated block-matching tracking algorithm supplied by EchoPac™, and the method applied by Slane *et al.* was based on a block-matching approach applied to the RF-signal space.

Concurrent validity tests

In this section, the concurrent validity test was evaluated by investigating the suitability of the estimated primary and auxiliary features for the discrimination between asymptomatic and symptomatic groups. For this experiment, primary and auxiliary features were calculated from the asymptomatic and symptomatic datasets.

The symptomatic volunteers were classified according to their VISA-A questionnaire and their Archambault score [186, 10]. This classification resulted in three classes: the less severe tendinopathy class (C1), the medium severe tendinopathy class (C2) and the very severe tendinopathy class (C3).

Figure 4.11 shows an example of tracking results for a C1 (Fig. 4.11(a)), C2 (Fig. 4.11(b)) and C3 (Fig. 4.11(c)) subjects during isometric contraction. A maximum tendon tissue displacement of 0.71 mm was obtained for the C1 subject, of 2.8 mm for the C2 subject and 5.58 mm for the C3 subject. The maximum estimations obtained for regional strain were 0.16 %, 0.3 % and 0.59 % for C1, C2 and C3 volunteers, respectively [4].

Significant differences were found, when using the mixed model approach, during isometric contraction between asymptomatic volunteers (C0) and C2; and between C0 and C3 subjects for superficial, medial and deep tendon tissue displacement ($0.0001<p<0.0016$) (Fig. 4.12(a)).

Significant differences, using the same mixed model approach, were found between the same groups (C0vsC2 and C0vsC3) for the proximal and distal tendon tissue displacement estimations ($0.0001<p<00008$). C1 and C3 were also found to be statistically different for superficial, medial and deep displacement ($0.0048<p<0.0497$) (Fig. 4.12(a)) and for proximal and distal tissue displacement ($0.014<p<0.021$). No significant differences were found between C0 and C1, C1 and C2 or between C2 and C3 during isometric contraction. Figures 4.12(c-d) represent information equivalent to the information presented by Fig. 4.12(a-b) but illustrate clearly a reduction of the sliding effect for group C2 and C3. Furthermore, a clear larger tissue displacement is obtained, at the three different layers, for C2 and C3 during isometric contractions in comparison with C0 and C1. This increasing of tendon tissue displacement for medium to severe cases is less pronounced during passive elongation of the tendon (as represented in Fig. 4.12(d)).

Table 4.3 shows the α values obtained using a mixed model approach for proximal/distal and superficial/medial/deep tendon tissue displacement estimations during isometric contraction. No significant differences were found between C0,C1,C2 and C3 during passive elongation (Fig. 4.12(b)).

For regional strain estimations during isometric and passive activation no significant results were obtained.

A ROC analysis between asymptomatic and more severe symptomatic cases (C0 vs. C2+C3) for average tissue displacement (using the 6 sub-ROIs) estimated during isometric contraction, returned an area under the ROC curve (AUC) of

---

[4] Tracking videos are available in digital version

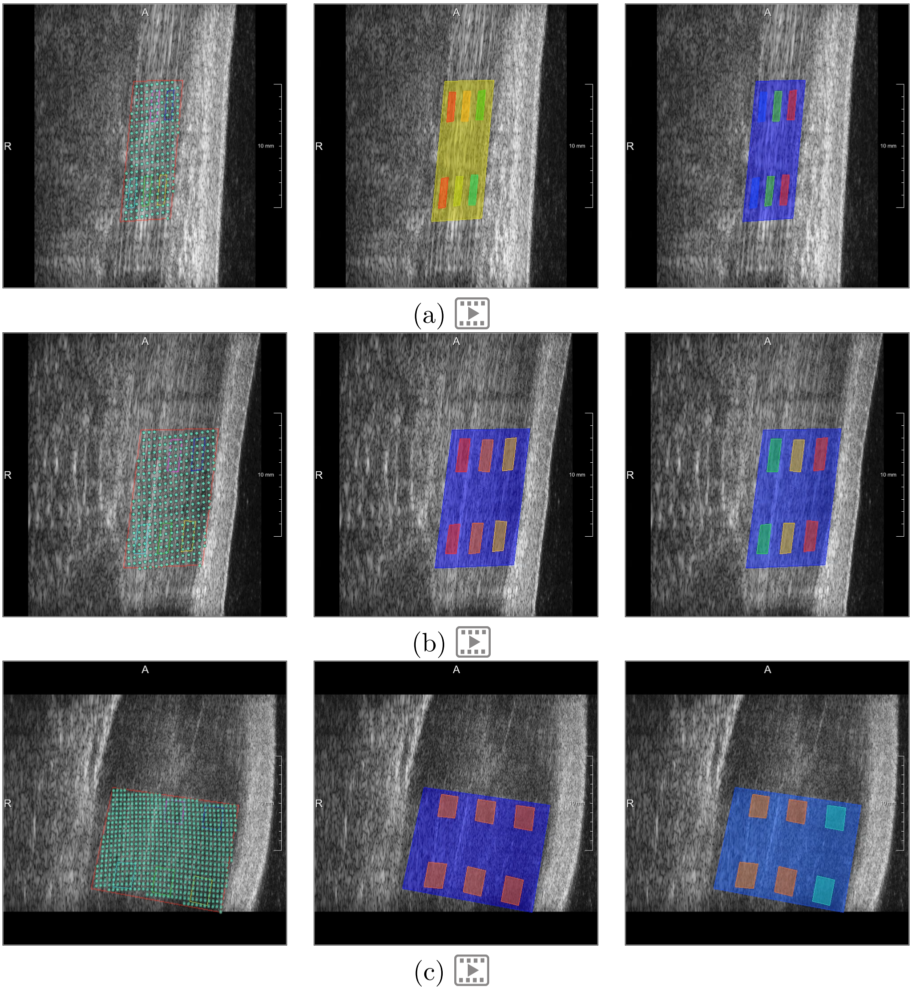

(a)

(b)

(c)

Figure 4.11: Tracking results for C1 (a), C2 (b) and C3 (c) classes during isometric contraction. The left panel shows tracking results; middle panel represents average displacement estimations whereas right panel represents average regional strain estimations along time. Tracking videos are available in digital version.

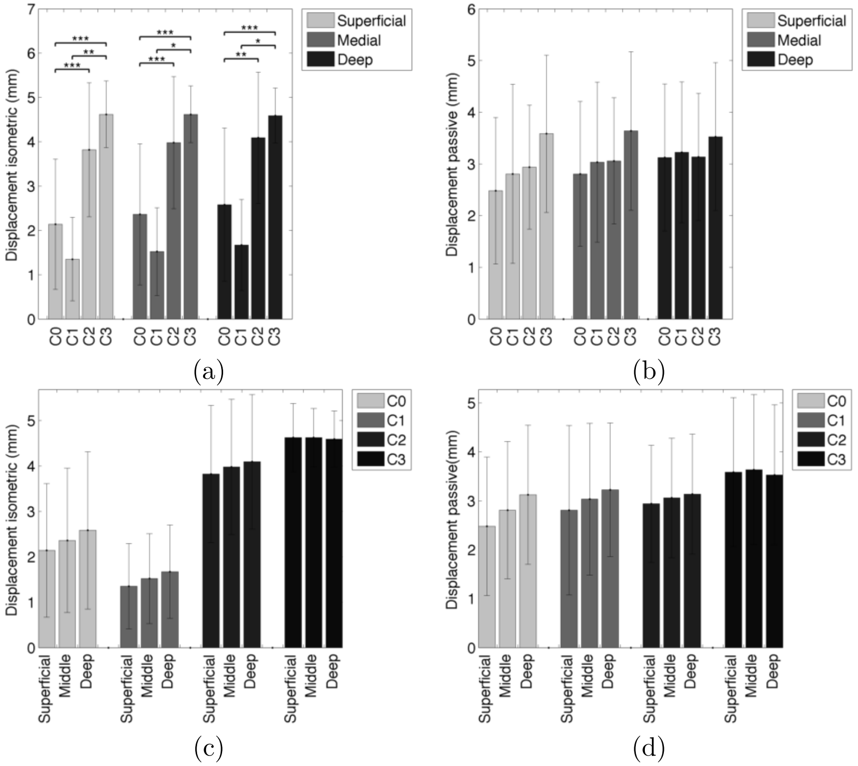

Figure 4.12: Significant differences and average values for local tendon tissue displacement estimations between superficial, middle and deep tendon layers during (a) isometric contraction and (b) passive elongation. (c) and (d) represent the same information as (a) and (b) but organized per group (** = p = 0.002 / *** = p < 0.001 / n.s. = non significant).

0.83, as represented in Fig. 4.13(a). When performing the same analysis but including all the symptomatic cases (C0 vs. C1+C2+C3), an AUC of 0.70 was obtained, as represented in Fig. 4.13(b).

4.7 Discussion

In this section, the results obtained for the four different psychometric tests are discussed.

Table 4.3: Mixed model analysis of tendon tissue displacement at proximal(prox)/distal(dist) and superficial(sup)/medial(med)/deep regions during isometric contraction along lateral direction. $\overline{\Delta}$ corresponds to medial tissue displacement.

		$\overline{\Delta prox}$	$\overline{\Delta dist}$	$\overline{\Delta Sup}$	$\overline{\Delta Med}$	$\overline{\Delta Deep}$
Mixed model analysis	C0vsC1	0.2873	0.3149	0.3062	0.3029	0.3041
	C0vsC2	0.0002	0.0008	0.0001	0.0004	0.0016
	C0vsC3	0.0001	0.0002	0.0001	0.0001	0.0009
	C1vsC2	0.0813	0.1365	0.0583	0.1019	0.1799
	C1vsC3	0.014	0.0213	0.0048	0.0163	0.0497
	C2vsC3	0.2735	0.2411	0.1715	0.2538	0.3558

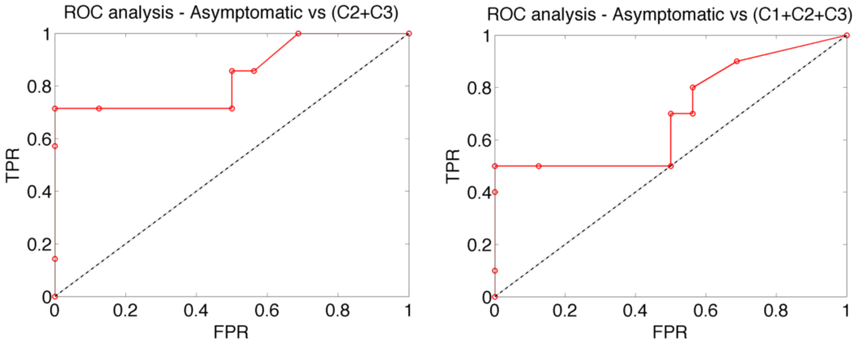

(a)

(b)

Figure 4.13: ROC analysis of asymptomatic vs. symptomatic cases. (a) ROC analysis of C0 vs. C2+C3 and, (b) ROC analysis of C0 vs. C1+C2+C3.

4.7.1 Predictive validity test

The reproducibility study showed fair to good reproducibility for in-vivo characterization of the local tendon tissue displacement and regional tendon strain estimations during isometric contraction and passive elongation. The low ICC values obtained on day two (4.2) were influenced by inaccurate US acquisition as well as inaccurate selection of the interval of interest for three images.

These fair to good correlations, for day one, provide evidence for the predictive validity test.

The reproducibility of the estimation of biomechanical properties of the Achilles tendon may be partly limited by the intrinsic anatomical variability between volunteers. Edama *et al.* and Szaro *et al.* [60, 207] have both demonstrated architectural variability of the Achilles tendon, which is one of the possible reasons for the variability obtained between volunteers. Abellaneda *et al.* [1] also investigated this variability of the Achilles tendon. In this work, they compared the elongation of the whole musculotendinous unit during a dorsiflexion between -10°and 30°. They observed that 62.5% of the tested subjects presented less tissue elongation than the others. A difference in the contribution of muscle and tendon for the elongation was also reported, with the muscle contribution being 71.8% and the Achilles tendon contribution being 28.2%.

This study hypothesized that these differences indicate that muscle strain and elongation of the Achilles tendon vary greatly between individuals. Arndt *et al.* [12] also observed a wide range of tendon tissue displacements and suggested that the differences seen between subjects could be an indication of the anatomical complexity of the Achilles tendon and the multiple variations of the insertion of the different subtendons.

Besides the known intrinsic variability, the reduced inter-day reproducibility of the obtained results is believed to be mainly caused by the differences in positioning of the US transducer on the two testing days. Besides that, the acquisition with the transducer holder and the gel pad sometimes became difficult because of slippage of the gel pad. In this case, repositioning of the transducer was required, which could have led to the acquisition of US images in a different plane than the images previously acquired.

4.7.2 Convergent validity test

The significant differences found for local tendon tissue displacement estimations between the various layers of the tendon were in line with the hypothesis formulated by Arndt *et al.*[12] and Slane *et al.* [196].

However, smaller values were obtained for the estimations with the presented method than for the estimations presented by Arndt *et al.* [12] and Slane *et al.* [196]. These differences can be due to the use of a smaller range of motion in this work (10° plantarflexion to 10° dorsiflexion) than the range of motion used by Arndt *et al.* (20° plantarflexion up to 15° dorsiflexion) and Slane *et al.* (0° to 30° plantarflexion). Fath *et al.* [69] reported a relation between the Achilles tendon length (estimated via the muscle-tendon junction displacement) and the

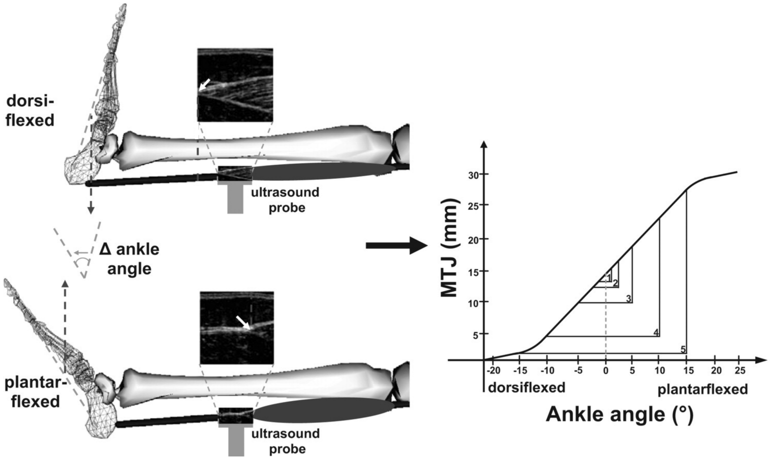

(a)

Figure 4.14: Schematic illustration of the tendon excursion method. Muscle-tendon junction MTJ, which illustrates tendon lengthening, is presented according to changes in the ankle angle.

range of motion from dorsi-to-plantarflexion. As Fig. 4.14 shows, if a smaller ranges of motion are applied, smaller tendon length, and thus smaller tendon tissue displacements, are obtained.

Another reason for the absolute differences in tendon tissue displacement found between the reported study and the ones of Arndt *et al.* [12] and Slane *et al.* [196], could arise from fundamental differences of the used US acquisition systems. As explained in section 2.2.1, the use of different US acquisition systems can result in the acquisition of different types of structures (fascicles with smaller caliber vs. larger caliber) that may deform differently from each other.

On the other hand, if the relative difference $(((\Delta_{deep} - \Delta_{sup})/\Delta_{deep})) \times 100)$ of the displacement at the deep and superficial layer is computed, a relative difference of 28.5% is obtained by Arndt *et al.*, 18.26% by Slane *et al.* and 14.5% in this study. These results show that, despite apparent large absolute differences of tissue displacement estimated at the different tendon layers, the relative difference of our method is similar to the results obtained by Slane *et al.*.

Physiological interpretation of these results is not straightforward but several reasons for this non-uniform behavior can be hypothesized. One of the possible reasons is associated with the "twisting effect" that occurs at the free Achilles

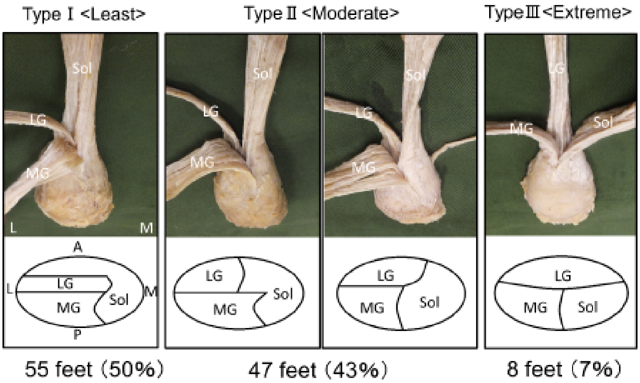

Figure 4.15: The patterns of "twisting" of the left Achilles tendon, posterosuperior view. The lower schemes represent the transverse cross section through the left Achilles tendon, 1cm above the tuber calcanei. A, anterior; L, lateral; LG, fibers from the lateral head of the gastrocnemius; M, medial; MG, fibers from the medial head of the gastrocnemius; P, posterior; Sol, fibers from the soleus muscle. (copyright obtained from Edama *et al.* [60])

tendon level. As described in the introduction, it was hypothesized that such rotation of the Achilles tendon was used for an equalization of the force-length properties of the Achilles tendon by optimizing the contractile ability of this tendon. Because different subtendons originate from different locations and this difference occurs both distal/proximal and medial/lateral, it is possible that these subtendons undergo deformation in different ways and present different force-bearing properties. According to Edama *et al.* [60], 40% of the examined cadavers presented a rotation of the Achilles tendon as the one represented in Fig. 4.15.

As this figure shows, the Soleus subtendon strongly influences the deformation of the anterior (deep) region of the tendon, in the twisting effects of type I and II. In type II, this role is divided with the lateral gastrocnemius tendon. In type III, which is the anatomical twisting configuration with the lowest prevalence in the tested population, the lateral gastrocnemius is positioned at the most anterior region of the free Achilles tendon while the soleus and the medial gastrocnemius subtendons share the most posterior region of the free Achilles tendon.

Besides the potential effect of this "twisting" and insertion of the different subtendons in different regions of the calcaneus, the non-uniform deformation seen in the free Achilles tendon may also be caused by the different functional roles of the gastrocnemius and soleus muscles. Interestingly, several studies have demonstrated that the medial gastrocnemius and the soleus muscles have a different proportion of fast-twitch fibers, number of in-series sarcomeres in a fast-cycle, and pennation angles [221, 28, 108, 114, 188, 189]. These differences between muscles have then been hypothesized to cause inter-muscle differences in muscle-tendon behavior and muscle activity during stretch-shortening cycles. Discrepancies between the fascicle behavior of medial gastrocnemius and soleus muscle have even been reported during walking by Ishikawa *et al.* [99]. As these reported results demonstrate, gastrocnemius and soleus muscles have different architectures and it is plausible that a greater loading of the soleus would potentially increase the distal stretch at the deep and medial regions of the Achilles tendon.

As the deep (anterior) Achilles tendon portion showed greater displacement than the superficial (posterior) portion in our study, it may be that fascicles derived from the lateral gastrocnemius are less stiff and thus displace less than those of the medial gastrocnemius and soleus during passive ankle motion.

Regarding the obtained differences between the tendon tissue displacements estimated during passive and isometric exercises, larger tissue displacement estimations and larger sliding between layers were obtained during passive exercises. These results are in line with the results reported by Finni *et al.* [72]. These authors investigated the influence of active versus passive muscle contribution to the behavior of muscle shear. This muscle shear is believed to have an influence on the tendon behavior. What they found was that, during passive elongation of the tendon, there is a slack and compliant connection between muscle bellies of the triceps surae, leaving margin for an independent non-uniform behavior. On the other hand, the tensing of these muscle connections can result in a more uniform deformation of the Achilles tendon.

The passive lengthening of the Achilles tendon is a sub-product of the lengthening of the entire muscle-tendon unit. In this case, the lengthening of the muscle-tendon unit is characterized by a simple mechanical model in which the muscle fascicles are arranged in series with the tendon. Here, both muscle fascicles and tendon contribute to the total change of the muscle-tendon unit length and the deformation of each structure occurs proportionally to their compliance [229]. Alternatively, during the isometric contraction, the muscle is activated but the ankle joint is static, meaning that there is no lengthening or shortening of the global muscle-tendon unit. Consequently, the elongation of the Achilles tendon during the passive trials is dependent on the range of motion and flexibility of the volunteer. In isometric movements, on the other hand, the elongation of the Achilles tendon is only caused by the activation of gastrocnemius and soleus.

The functional role of soleus and gastrocnemius is, at larger scale, equivalent and both these muscles are responsible for stabilizing and controlling major bony joints, providing coordination of the foot during the stance phase of gait and contribute to plantar flexion of the foot. However, during isometric contraction, no joint motion exists which may lead to different deformation mechanisms than the ones obtained during passive or eccentric motion, for instance.

Concerning regional tendon strain estimations, the herein presented study is the first to report such feature estimation for the in-vivo characterization of tendons. Due to that, no convergent validity test could be performed for regional tendon strain estimations.

However, surprising results are obtained for the quantification of this biomechanical property. This arises from the apparent illogical relation between lower tendon tissue displacement and larger strain estimations at the superficial region, in comparison with the larger tendon tissue displacement and lower strain estimations at the deeper region. The regional strain estimations performed in this work were described in section 4.2 and, for the calculation of this biomechanical feature, the average tissue displacement estimations are used. In order to clarify and better understand these strain estimations, a practical example of two strain estimations for deep and superficial layers is presented below.

Let's assume a larger tissue displacement at the deeper regions (R2 and R5, top and bottom, respectively) while the regions at the superficial layer (R4 and R7) present lower tendon tissue displacement estimations (as depicted in Fig. 4.16). As a numerical example, we set $\Delta_{R2} = 0.7mm$ and $\Delta_{R5} = 0.8mm$, $\Delta_{R4} = 0.15mm$ and $\Delta_{R7} = 0.35mm$. The central position, along the lateral direction, of regions R2 and R4 is 5mm (from the top left corner of the image), while the central position of regions R5 and R7, along the lateral direction, is 15mm (from the top left corner of the image). In this way, the initial distance (length) between the top (R2 and R4) and bottom (R5 and R7) regions is 10mm. We also know that R2 displaced 0.7mm, thus it moved from position 5mm to 5.7mm and R5 displaced 0.8mm, thus it moved from 15mm to 15.8mm. Thus, the strain which occurred at the deep layer can be computed and corresponds to:

$$L_0 = 10mm \tag{4.6}$$

$$L_1 = 15.8 - 5.7 \Leftrightarrow L_1 = 10.1mm \tag{4.7}$$

$$\varepsilon_{Deep} = \frac{L_1 - L_0}{L0} \times 100 \Leftrightarrow \varepsilon_{Deep} = \frac{10.1 - 10}{10} \times 100 \Leftrightarrow \varepsilon_{Deep} = 1\% \tag{4.8}$$

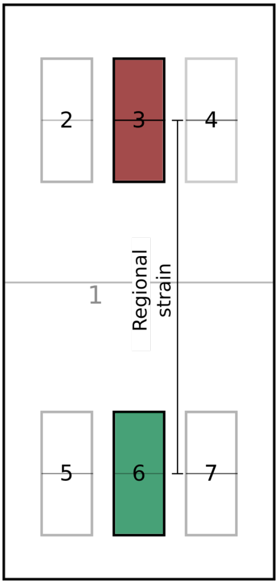

Figure 4.16: Example of two regions, proximal and distal, used for the calculation of regional strain. R2 and R5 correspond to the deep layer while R4 and R7 correspond to the superficial regions.

A similar calculation can then be performed for the superficial strain. In this case, the initial distance between R4 and R7 is also 10mm but, the displacement of region R4 was 0.15mm, meaning that the center of R4 displaced from 5mm to 5.15mm, while the center of R7 moved from 15mm to 15.35mm. The strain for the superficial regions is then:

$$L_0 = 10mm \tag{4.9}$$

$$L_1 = 15.35 - 5.15 \Leftrightarrow L_1 = 10.2mm \tag{4.10}$$

$$\varepsilon_{Sup} = \frac{L_1 - L_0}{L0} \times 100 \Leftrightarrow \varepsilon_{Sup} = \frac{10.2 - 10}{10} \times 100 \Leftrightarrow \varepsilon_{Sup} = 2\% \tag{4.11}$$

As the above calculations demonstrate, a large tissue displacement does not necessarily correspond to a large strain calculation. Alternatively, larger strain estimations are obtained when there is a large relative difference between the displacement of top/bottom regions. Other examples of strain calculations are presented in appendix C.

After understanding the technical details behind the calculation of regional strain, it is important to interpret its physiological meaning. Unfortunately, the high variability obtained in this work for in-vivo strain estimations has also been obtained by others, which prevents its report in peer-reviewed papers. Lyman *et al.* [146] are the only ones who reported in-vivo strain quantifications of the free Achilles tendon. It was demonstrated that, during dorsiflexion movement, the superficial layer of the tendon presented a significant increase of strain, while the anterior (deep) layer did not present any significant difference but rather a trend towards decreasing strain.

However, a large variability was observed for these regional tendon strain estimations. It was then hypothesized that such high variability estimates could be a result of out-of-plane motion. Chapter 5 of this work focuses on the further investigation of this matter.

In summary, the high-correlation for tendon tissue displacement estimations obtained between the results reported in the literature and the estimated results provides enough evidence of convergent validity. Because it was the first time regional Achilles tendon strain estimations were presented, the convergent validity test was not performed.

4.7.3 Discriminant validity test

For the discriminant validity, the assumption of the fundamental differences of the method developed and the methods presented in the literature (RF-based block-matching method [35] and commercial B-mode block-matching speckle tracking method [12]) was assumed. Furthermore, the acquisition system used for this work was also different than the acquisition system used by the others. Both theoretical differences and image acquisition differences of the compared methods allowed to validate the discriminant validity test.

4.7.4 Concurrent validity test

Concerning the discrimination between asymptomatic and symptomatic volunteers, proximal/distal tendon tissue displacement and superficial/medial/deep tendon tissue displacement were found to be good candidates for this task. Significant differences were found between the asymptomatic and the mild and severe cases of tendinopathy. However, these features did not exhibit similar effectiveness discriminating between subjects with light tendinopathy complaints and asymptomatic subjects.

Results reported in the literature for ageing volunteers, demonstrated an increase of tendon tissue displacement of the free Achilles tendon, in comparison with young volunteers. A similar increase of tissue displacement was also obtained in this work but between asymptomatic/mild tendinopathy cases and medium/severe cases. Furthermore, a reduction of the differences of tissue displacements between superficial and deep regions was also observer for the medium/severe cases which is also in line with the results reported in the literature for aged volunteers [209, 76, 75, 77, 195].

The physiological interpretation of these results may reside in an increase of the compliance of aged and symptomatic tendons, which would lead to larger tissue displacements. Concerning the reduction of the differences of tissue displacement between different tendon layers, some biomechanical underlying hypotheses have been proposed such as the proliferation of collagen cross-linking and inter-fascicle adhesion. The increase of these collagen cross-linking and adhesions could then be responsible for the loss of independence between the three different Achilles subtendons which can, in turn, result in a different pattern of deformation and it can also lead to improper strain distribution within the tendon [76, 75]. If this occurs, then the association between aged tendons and symptomatic tendons is even stronger because it seems that the reduction of this sliding effect is the primary stage for the evolution of tendinopathies.

The presented ROC analysis confirmed that the estimated features performed better for the discrimination between asymptomatic and medium to severe tendinopathy cases (C2+C3) rather than between asymptomatic and symptomatic cases (C1+C2+C3).

Regarding the concurrent validation test, *per se*, the obtained results are believed to provide evidence of concurrent validity but with reduced power.

4.7.5 Limitations

The absence of ground-truth prevents the quantitative evaluation of the developed image registration method *per se*. However, qualitative evaluation of the image registration process is possible by visual inspection of the tissue displacement estimations (as presented in Fig. 4.9 and Fig. 4.11, left column). Good quality of tissue displacement estimation was obtained for most of the 2D HST US images acquired in this study. Nevertheless, some factors can impair good image registration results (as shown in Fig. 4.17). First, the selection of a correct *interval of interest* is of primary importance. Fig. 4.17(top-left) shows what should be a movement from 10° plantarflexion to 10° dorsiflexion. As it is evident, the selection of the interval of interest in this image shows very little or limited tissue displacement, contrary to what is expected. Regarding the selection of the *ROI*, similar problems can also occur, as illustrated in Fig. 4.17(bottom-left). In this situation, an ROI miss-aligned with the primary deformation direction of the tendon can yield wrong tissue displacement and regional strain estimations. The third type of problem can arise from low contrast within the tendon area, as illustrated in Fig. 4.17(top-right). In this case, either due to high stiffness of the tendon or low gain setting during the US acquisition, the tendon contains few speckle information, generating, therefore low-quality speckle tracking. The fourth type of registration error is exemplified in Fig. 4.17(bottom-right). In this situation, the region of interest is shrinking in length which is not expected to occur in an asymptomatic tendon. When evaluating the results closer, it becomes apparent that the tracking of the distal part of the region is getting trapped at local minima during optimization. One of the reasons for this to occur is the existence of a region with high speckle decorrelation, which may be caused by incomplete contact between transducer and skin (see Fig. 4.18).

After visual evaluation of the tracking results for symptomatic images, some adaptations of the registration method could have been done to obtain better strain and tissue displacement estimations for some cases (as represented in Fig. 4.11(bottom-left)). Possible adjustments would include a reduction of the regularization coefficient to allow tracking of calcified regions, for instance.

Another limitation, commonly mentioned in the literature as a source of tendon strain estimation errors, is the out-of-plane motion. The acquired 2D HST US data presents some out-of-plane motion (Fig. 4.18), but it is believed that the used acquisition setup is the setup currently available which suffers the least from this type of artifact. Despite that, the acquisition at high-frame rates implies the storage and processing of large quantities of data which can result in a lengthy processing.

4.8 Concluding remarks

The presented chapter described the adaptation of the 2D global strain estimation method into a method for 2D in-vivo local characterization of local tendon biomechanics. This adaptation involved mostly the change in the image transformation model used by the registration method and it was beneficial because of the added value of local tendon biomechanics quantification reported in the literature [225, 146, 191, 33, 112, 12, 137, 209, 196, 24, 76, 75, 77]. Furthermore, as described in Chapter 2, the use of high-spatial and high-temporal resolution images is assumed to be of crucial importance for the estimation of local tendon biomechanics.

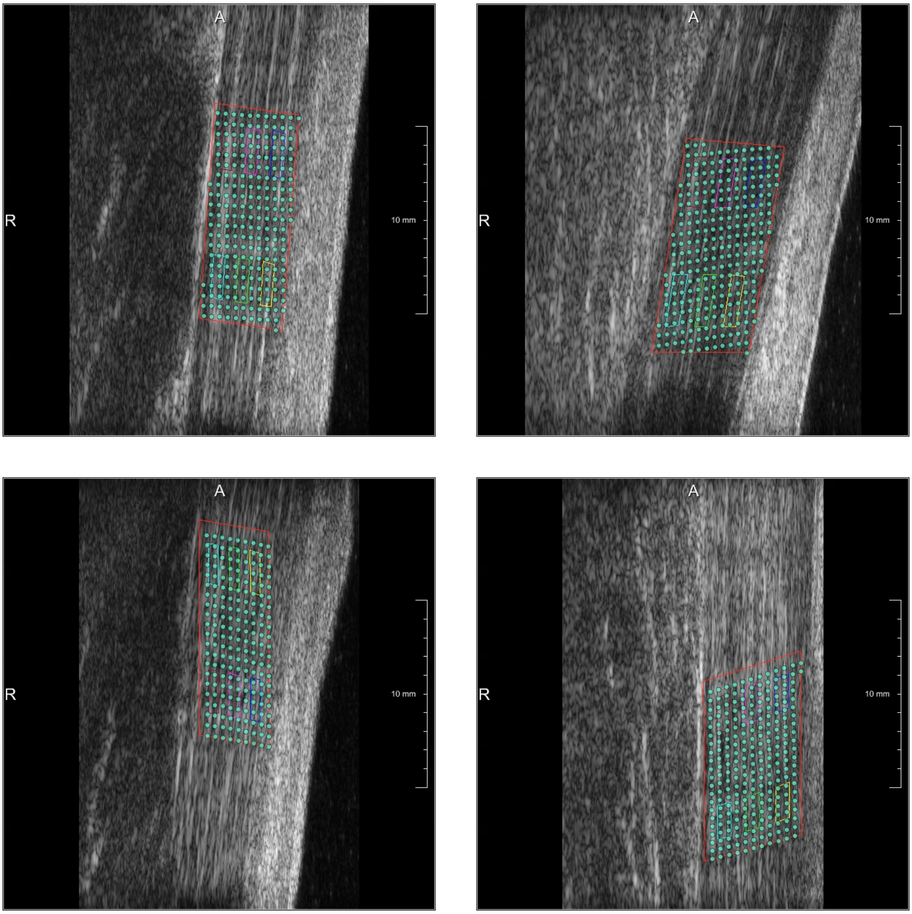

Figure 4.17: Different types of errors for the asymptomatic database. An interval of interest error (top-left) and region of interest selection error (bottom-left). (top-right) shows acquisition errors due to shadowing effects and (bottom-right) represents tendon tissue tracking error. Demo video is available in digital version

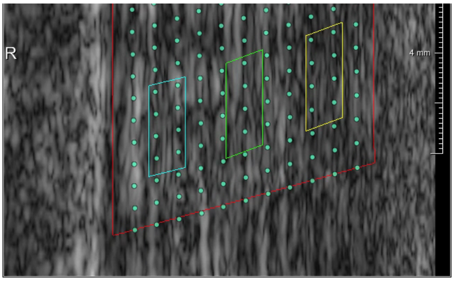

Figure 4.18: Tracking error due to speckle decorrelation. Demo video is available in digital version

Despite the increased interest in the characterization of local tendon biomechanics, there is no valid ground-truth for this type of data. Due to that, a psychometric validation approach was followed. This psychometric approach was divided into four validity tests, being predictive, convergent, discriminant and concurrent. The obtained results provide evidence of the validity of the predictive, convergent and discriminant tests while a reduced but existent power was obtained for the concurrent validity test.

This work presents also, for the first time, in-vivo regional tendon strain estimations. The obtained results showed larger strain estimations at the superficial layer and smaller strain estimations at the deep layer. Besides the novelty of these results, the inverse behavior of tendon strain estimations in comparison with tendon tissue displacement is also interesting and should be further investigated. This work had also the goal of establishing a bridge between the bench and the bedside. To do that bridging of knowledge, the method developed for the in-vivo characterization of local tendon biomechanics was embedded in an easy and intuitive application called KULTeC. Besides the embedding of the image registration process in this application, also the required pre-processing steps and the visualization of the final results are possible using the KULTeC application. It is also believed that the introduction of the KULTeC application in the clinical practice could help in the design of new studies, allow the processing of new images, and provide an intuitive and interactive representation of the obtained results.

To conclude, the datasets used for the characterization of in-vivo local tendon biomechanics are of limited size. Due to that, the obtained results are of exploratory nature and larger datasets should be used to further investigate the results here presented.

Chapter 5

Global tendon strain estimations for investigation of out-of-plane motion using 3D high-spatial resolution ultrasonography

Contents

As described in the previous chapter, out-of-plane motion is a possible source of tendon strain estimation errors [34, 26, 168, 176, 204, 6].

In order to understand the possible implications of out-of-plane motion in tendon strain quantifications, an analogy between cardiac strain quantifications performed using ultrasound images and tendon strain quantifications also performed using ultrasound images is presented below.

Strain quantification is more commonly performed in the cardiology field [95, 93] than in the tendon biomechanics field. Interestingly, both these fields perform strain quantification using US images but, for cardiac US images, strain quantification is quite successful, as opposite toS the high-variability present for strain estimations of the Achilles tendon. This success is apparent from the existence of a speckle tracking block-matching approach (EchoPac™) for cardiac strain estimations which is commercially available. On the other hand, tendon strain quantification has not yet been accomplished with obvious success. Fröberg *et al.* [81] attempted to use the EchoPac™software for isolated tendon strain estimations and obtained strain estimations with very high-variability and much larger values than the values reported in the literature

One of the possible reasons for the different accuracies obtained when estimating cardiac strain or tendon strain may be the intrinsic twisting effect of the Achilles tendon. This twisting effect can then exacerbate out-of-plane motion and lead to inaccurate tendon strain estimations. In fact, *out-of-plane motion has been commonly pointed out as a possible source of tendon strain estimation errors* [34, 26, 168, 176, 204, 6].

This chapter investigates the impact of out-of-plane motion on the accuracy and reproducibility of tendon strain estimations.

In the first section of this chapter, the developed affine image registration method used for quantification of 3D global strain is described. Afterwards, the acquisition of 3D in-silico, 3D in-vitro and 3D isolated tendons data is presented. Lastly, the performance of the developed strain quantification method is evaluated and a discussion concerning the overall obtained results and the encountered limitations is presented.

5.1 3D affine image registration approach for global tendon strain estimations using 3D high-spatial resolution US data

Similarly to the *2D global strain* estimations, *3D global strain* estimations were performed using an *affine image registration* approach. The image registration method applied for the estimation of 3D global strain used in this chapter corresponds to an adaptation of the method developed in chapter 3 for the processing of 3D images.

For the sake of completeness, a short description of the used method is given below.

As explained before, the image registration problem is formulated as an optimization problem in which the transformation between moving and fixed images is optimized to maximize the similarity between those two images. The transformation of the moving image was then performed using an affine transformation such that the sum of squared differences between the moving and fixed image intensities was minimized. The optimization of this transformation was performed using a quasi-Newton limited memory BFGS optimization scheme. This registration method was applied according to a three-level multi-resolution pyramidal scheme and to implement this scheme, a Gaussian pyramid with $\sigma = 4$ and $\sigma = 2$ pixels was used along both the axial and the lateral direction. As for the 2D global strain estimations, a pairwise registration strategy was used for 3D as well and consecutive 3D volumes were registered to each other, as represented in Fig. 5.1 (bottom-axis). Once this pairwise registration was completed, each pairwise transformation was composed with its previous transformation(s) subsequently. This composition process returned a final affine transformation matrix which describes the transformation applied between the moving and the fixed image, as represented in Fig. 5.1 (top-axis). The registration method was implemented using Elastix [120, 193] and the used parameter file can be found in appendix D.

5.2 Data

In this section, a description of the acquisition of 3D high-spatial (HS) US in-silico, in-vitro and isolated tendons data is described.

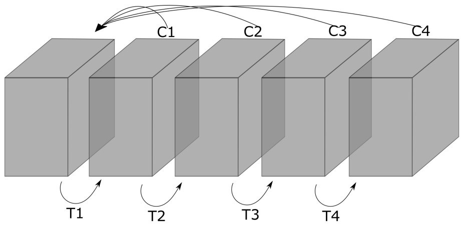

Figure 5.1: Image registration strategy. The bottom axis (T_n) represents the pairwise image registration, and the top axis (C_n) accounts for the composition process to obtain the registration to the first volume.

5.2.1 3D in-silico data

Similar to the case of simulation of 2D in-silico data, also 3D in-silico data was initially simulated due to its low complexity and known ground-truth values. The constructed and consequently deformed 3D model described in section 3.2, was re-used for this experiment. In summary, a simplified 3D model of a tendon, with physiologically plausible dimensions [86], was constructed in Matlab. The tendon components were approximated using cylindrical shapes, and the lowest intensity values were assigned to surrounding soft tissue points, the medium intensity values to the tendon unit and the high-intensity values to the tendon fascicles points. Scatter points mimicking contact gel particles were added to the constructed model at random positions.

Strain was estimated using an elliptic cylinder volume preservation equation $V = \pi * Dsmall * Dlarge * L/4$, where $Dsmall$ and $Dlarge$ correspond to the axis lengths of the base of the ellipse and L corresponds to the height of the cylindrical shape. The presented formula describes an elliptic cylinder shape that can be adapted to the dimensions of the isolated tendons (described in section 5.2.3). For the case of in-silico data, $Dsmall$ was equal to $Dlarge$.

The model was deformed between 0% and 2% strain with incremental intervals of 0.25% strain, resulting in one undeformed and eight deformed models. This deformation was obtained by displacing the scatterers along the strain direction and towards the center of the volume. Contact medium points were randomly positioned for each strain value.

Instead of selecting the central slab of points of the 3D constructed models as in the case of 2D US simulation, for the simulation of 3D HS US images, multiple 2D slabs of points were selected from each of the constructed models. These slabs were separated along the elevation direction by an interval of 0.09 mm (equivalent to the motor's step-size), and each slab had a thickness of 2.8 mm

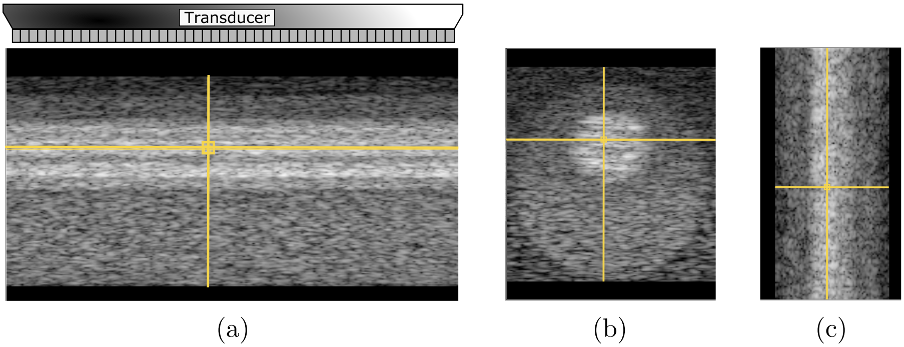

Figure 5.2: Example of 3D US in-silico image. (a) represents the in-plane simulation, (b) the transverse plane and (c) the coronal plane.

(equivalent to the US transducer height). This was done such that the simulated images were acquired similarly to the real 3D HS US acquisition as described in section 2.2.2. Each slab was then used as input to the same US simulation platform (Field II [105, 104]) used for the 2D HS US simulation.

Also in this situation, simulation parameters were chosen to optimally mimic the parameters used by the Vevo 2100 with the 21 MHz central frequency transducer (section 2.2.2). Finally, the simulated 2D US slices were concatenated into a 3D image with a resolution along the elevation direction of 0.09 mm (equivalent to the motor's step-size). This process was repeated for each of the eight different deformed models.

Ground-truth values for strain obtained from the deformation applied to the 3D model.

Figure 5.2(a) illustrates a cross section of the 3D in-silico US image. In these images, the transducer was longitudinally aligned with the height of the cylinder model (Fig. 5.2(a)) and single 2D slices were acquired at each step position. Figure 5.2(b) and Fig. 5.2(c) correspond to the transverse and coronal planes.

5.2.2 3D in-vitro data

Regarding in-vitro data, six agar-based phantoms with amorphous graphite scattering were constructed. The agar solution was poured into a cylindrical mold with diameter and height of 7 cm. Figure 5.3 shows an example of these phantoms.

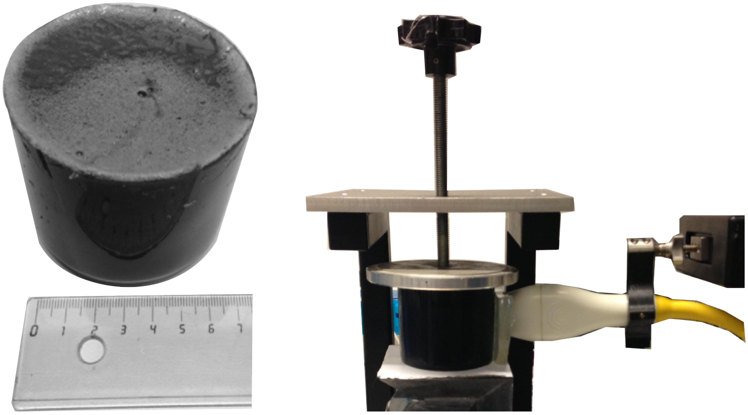

(a) (b)

Figure 5.3: Example of 3D in-vitro data. (a) Example of a constructed agar-based phantom and (b) illustration of the used compression mechanism.

Ground-truth values for in-vitro data were obtained by compressing the phantoms using a custom-built mechanical device containing two parallel plates (Fig. 5.3(b)). These plates compressed the phantom up to a maximum of 2.14% of strain (increment of 0.50%) along the lateral direction corresponding to 1.09% strain along the axial and elevation direction. Incremental strain steps were larger than the ones used for simulated data due to the limited precision of the mechanical device. Eq 5.1 provides the relation between the material compression and strain estimation along the lateral direction ($\varepsilon_{lateral}$), along the axial direction (ε_{axial}) and along the elevation direction ($\varepsilon_{elevation}$)

$$\begin{aligned} \varepsilon_{lateral} &= \left(\frac{L_1}{L_0} - 1\right) \times 100 & assuming,\quad R_{coeff} &= \frac{Rlarge_0}{Rsmall_0} \\ \varepsilon_{axial} &= \left(\frac{Rsmall_1}{Rsmall_0} - 1\right) \times 100 & Rlarge_1 &= \sqrt{\frac{L0 \times {Rlarge_0}^2}{L_1}} \\ \varepsilon_{elevation} &= \left(\frac{Rlarge_1}{Rlarge_0} - 1\right) \times 100 & Rsmall_1 &= \frac{Rlarge_1}{R_{coeff}} \end{aligned} \tag{5.1}$$

where L_0/L_1, $Rsmall_0/Rsmall_1$ and $Rlarge_0/Rlarge_1$ correspond to the initial/final height, radius along axial direction and radius along the elevation direction, respectively. The axial radius obtained after deformation was

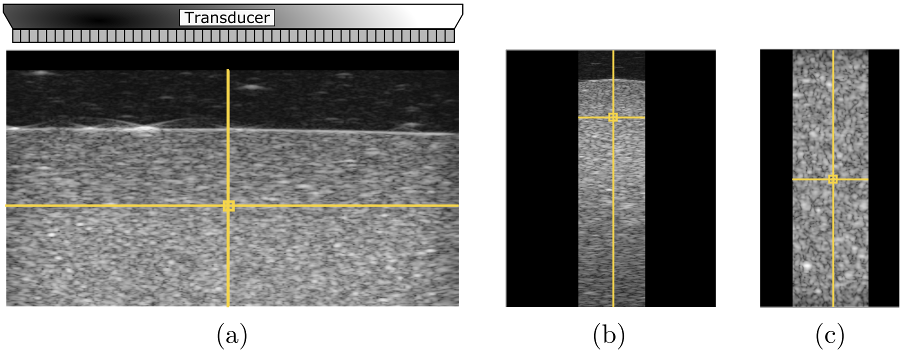

(a) (b) (c)

Figure 5.4: Example of 3D HS US in-vitro image. (a) represents the in-plane acquisition, (b) the transverse plane and (c) the coronal plane.

calculated by assuming a constant coefficient between axial and elevation radius after and before deformation(R_{coeff}). The next step was to estimate $Rlarge_1$ which was obtained assuming there is volume preservation before and after deformation. The final step was then the estimation of $Rsmall_1$ using the previously calculated $Rlarge_1$ and R_{coeff}. The presented formula describes an elliptic cylinder shape that can be adapted to the dimensions of the isolated tendons (described in the following section). However, due to the cylindrical shape of these phantoms, $Rsmall$ was equal to $Rlarge$.

Figure 5.4 shows an example of an agar-phantom 3D HS US image. In these tests, the transducer was longitudinally aligned with the height of the cylinder (Fig. 5.4(a)). Figures 5.4 (b) and (c) correspond to the transverse and coronal planes. 3D US images were acquired with the 3D module of the Vevo 2100, using the 21MHz transducer, as described in section 2.2.2.

Alternative 3D in-vitro data

Besides the construction of agar-based phantoms, also polyvinyl alcohol (PVA) phantoms were constructed. The PVA-based phantom was constructed according to Surry *et al.* [205] with addition of graphite scattering. The solution obtained from the mixture of water with PVA and graphite becomes a cryogel when subjected to freezing and its stiffness and elasticity are dependent of freeze/thaw cycles, freeze temperature and freezing/thawing rate. The more freeze/thaw cycles this solution is subjected to, the stiffer the material becomes. Three freeze-thaw cycles were found to give the desired stiffness and elasticity. Each cycle consisted of a 12 hours freezing cycle, at -20°C, followed by a 12 hours

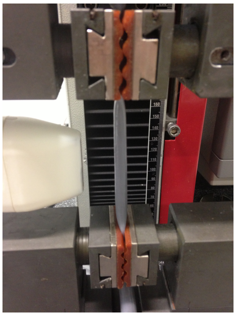

Figure 5.5: Example of 3D PVA data mounted on an uniaxial tensile test device

thawing period at room temperature. The used molds consisted of rubber tubes with length of 20 cm and a diameter of 7 mm, mimicking in this way the structure of human Achilles tendon.

After the freezing/thawing cycle, a strong elastic cylinder is obtained. The advantage of this phantom in comparison to an agar-based phantom is that, due to its shape, it can be mounted in a uniaxial tensile device (ZwickiLine Prüfmaschinen Z0.5 - Zwick-Roell, Ulm, Germany), allowing in this way a stretching behavior closer to the in-vivo conditions. Despite these theoretical advantages, in practice, the clamping mechanism tended to wear and eventually break the tendon with increasing strain. An example of the mounting of these phantoms during an uniaxial tensile test is shown in Fig. 5.5.

Figure 5.6 shows an example of an PVA 3D HS US image. In these tests, the transducer was longitudinally aligned with the height of the tubular structure (as represented in Fig. 5.5).

Figures 5.6 (b) and (c) correspond to the transverse and coronal planes of the acquired 3D images. 3D US images were acquired with the 3D module of the Vevo 2100, using the 21MHz transducer, as described in section 2.2.2. Due to the acquisition and clamping problems above mentioned, the PVA phantoms were not included in further experiments.

5.2.3 3D isolated tendons data

For the acquisition of 3D isolated tendons data, seven superficial digital flexor tendons were harvested from individual sheep (institutional and national guides for the care and use of laboratory animals were followed - P065-2013). These tendons were mounted in the same material-testing device used for the 2D

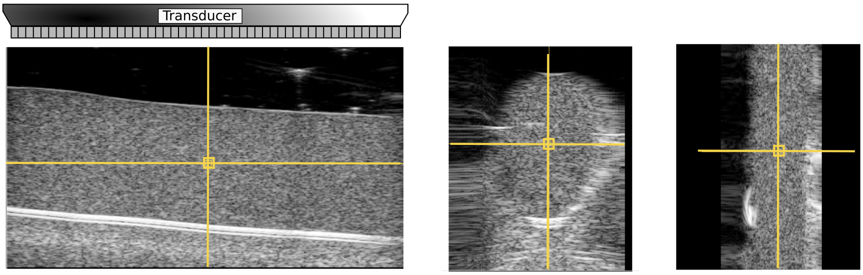

(a) (b) (c)

Figure 5.6: Example of 3D US PVA phantom image. (a) represents the in-plane acquisition, (b) the transverse plane and (c) the coronal plane.

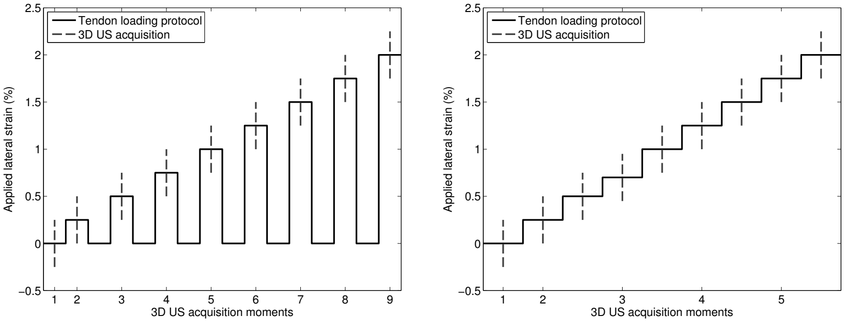

(a) (b)

Figure 5.7: Isolated tendons data loading protocol. (a) corresponds to the loading protocol used in this work, while (b) corresponds to the attempted but not used protocol. The dashed lines correspond to the 3D US acquisition moments.

global strain estimations (ZwickiLine Prüfmaschinen Z0.5-Zwick-Roell, Ulm, Germany). Maximum allowed strains were defined such that all testing was performed in the linear region of a previously reported stress-strain curve [152]. Consequently, applied strain values were limited to 2% strain. Specimens were preconditioned with cyclic stretches at a frequency of 0.5 Hz to 2% strain for ten cycles. Before each test, seven minutes of rest were given to the samples [152, 35, 34].

Afterwards, tendons were loaded according to a semi-dynamic loading protocol consisting of an increment of strain values in steps of 0.25% along the lateral direction followed by US data collection. After that, clamps were repositioned

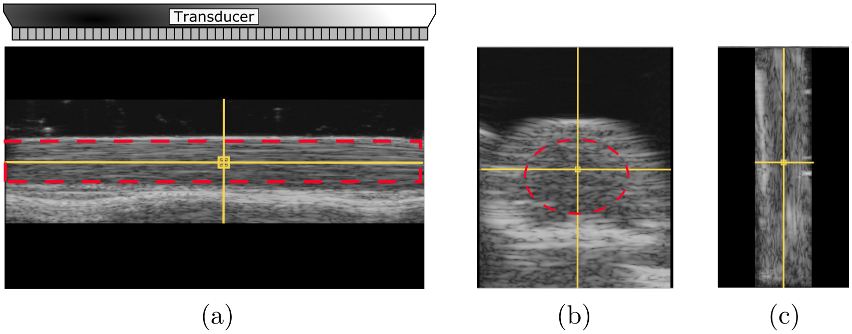

Figure 5.8: Example of 3D HS US isolated tendon image. (a) represents the in-plane acquisition, (b) the transverse plane and (c) the coronal plane.

to a position corresponding to a measured load of 10 N and an increment of 0.25% strain to the previously applied strain was applied. This procedure was repeated up to 2% strain (Fig. 5.7(a)).

Ground-truth strain values along the axial and elevation directions were obtained using eq. 5.1 where $Rsmall$ corresponds to the radius along the axial direction and $Rlarge$ corresponds to the radius along the elevation direction.

3D HS US images were acquired with the transducer aligned longitudinally with the tendon. Gel was applied in abundance to avoid loss of contact. Figure 5.8 shows an example of a 3D HS US image of an isolated tendon. The transducer was aligned with the longitudinal axis of the tendon as depicted in Fig. 5.8(a). Figure 5.8(b) and Fig. 5.8(c) correspond to the transverse and coronal planes, respectively.

Alternative loading protocol of 3D isolated tendons data

Two different loading protocols of the isolated tendons where designed. The first was equivalent to the protocol described above (loading of the tendon and return to the baseline) while the second differed from the first by not returning to the baseline. In other words, in the second loading protocol, the tendon would be loaded with an increment of 0.25% strain, a 3D image would be acquired, and instead of returning to the baseline, the tendon would be loaded 0.25% strain more, as demonstrated in Fig. 5.7(b). This process would be repeated until the 2% strain would be reached. However, when following this loading setup, very small strain values were measured using the 3D global strain estimation method. After investigation, it was hypothesized that the holding time in each step was enough for the tendon to suffer relaxation and the 0.25% strain increment did not start from a pre-loaded tendon, but rather with a relaxed/slack tendon. For these reasons, no further experiments were conducted with this protocol

5.3 Validation of 3D global strain estimations

In this section, the statistical tools used for evaluation of the performance of the developed 3D global strain estimation method and the obtained results are presented.

5.3.1 Analysis

As in the case of 2D global strain estimates, the Pearson correlation coefficient [154, 37, 123, 94, 35, 169] was measured to determine the strength of the relationship between calculated and ground-truth strain values.

Furthermore, the previously described mean absolute error (MAE eq.(3.20)), mean relative error (MAE eq.(3.20)), mean absolute deviation (MAD eq.(3.20)) and normalized squared error (NSE eq.(3.20)) were computed.

Estimated strains were obtained from the affine transformations whereas ground-truth strains were obtained from the deformation mechanisms (i.e. simulation model, compressing mechanism and uniaxial tensile test device).

5.3.2 Results

Because the main goal of the work presented in this chapter is the investigation of the impact of the out-of-plane motion for tendon strain estimations, comparisons (when possible) with the data obtained for 2D global strain estimations are made.

For the sake of this comparison, the relevant 2D global strain estimation plots are here presented once again.

2D and 3D in-silico global strain estimations

3D and 2D strain estimation correlation plots show equal correlation coefficients, but 2D global strain estimations present lower regression slopes (Fig. 5.9 (a-b) when compared to 3D strain estimations (Fig. 5.9 (c-d)). Table 5.1 shows the

MAE, MRE, MAD and NSE analysis for 2D and 3D strain estimations. All of the error estimation measures show better performance for 3D than for 2D strain estimation. MRE for 3D and 2D strain estimations shows clear improvement of results when using 3D data.

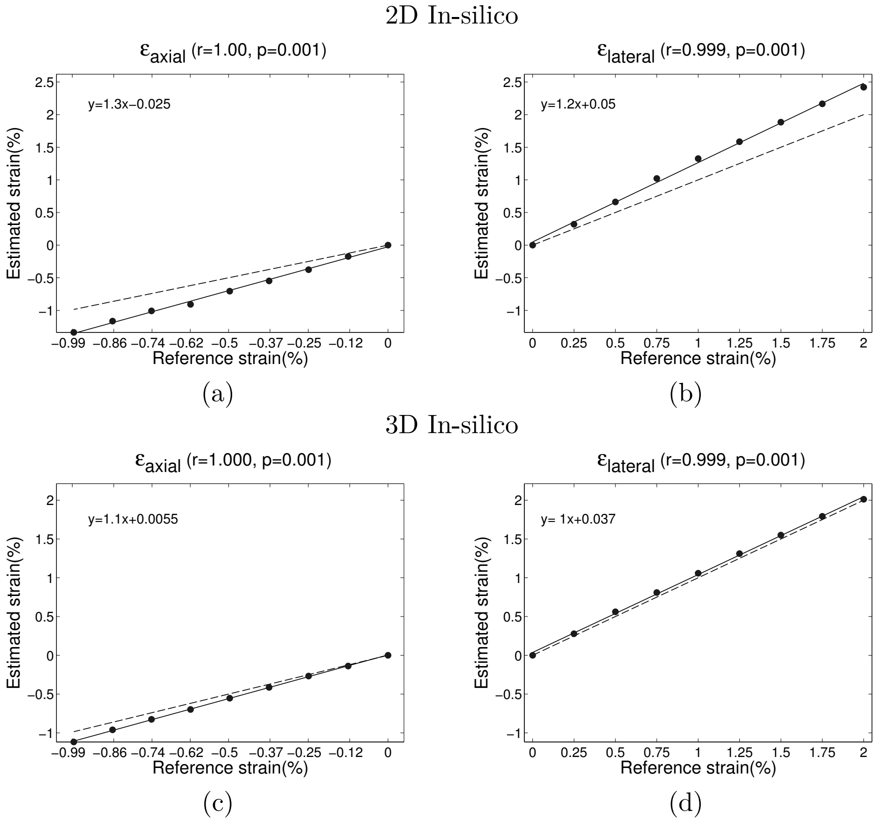

(a) (b)

(c) (d)

Figure 5.9: Scatter plots of 2D and 3D in-silico data. (a-b) represent 2D in-silico data strain estimations along axial (a) and lateral (b) direction. (c-d) represent 3D in-silico data strain estimated along axial (a) and lateral (b) direction. The dashed line represents the line of identity and the solid line represents the linear fitting to the data.

3D in-vitro global strain estimations

Validation based on in-vitro data showed good agreement along the axial and lateral direction with correlation coefficients of 0.89 and 0.92, respectively

Table 5.1: Mean absolute error (MAE), mean relative error (MRE), mean absolute deviation (MAD) and standard deviation normalized squared error (NSE) for 3D in-silico, in-vitro and isolated tendons data. Errors are presented in %.

		In-silico				In-vitro				Isolated tendons			
		MAE	MRE	MAD	NSE	MAE	MRE	MAD	NSE	MAE	MRE	MAD	NSE
3D	$\overrightarrow{axial}$	0.07	11.17	0.27	-0.01	0.17	17.84	0.26	-0.06	0.37	69.77	0.49	-0.42
	$\overrightarrow{lateral}$	0.05	6.08	0.49	0.003	0.38	28.60	0.45	0.14	1.18	102.08	0.23	1.67
	$\overrightarrow{elevation}$	0.27	38.62	0.49	-0.22	1.35	238.75	1.26	-3.59	1.12	189.81	1.45	-1.42
2D	$\overrightarrow{axial}$	0.21	41.49	0.32	-0.09	-	-	-	-	-	-	-	-
	$\overrightarrow{lateral}$	0.29	28.28	0.59	0.08	-	-	-	-	0.32	18.27	1.29	0.075

2D isolated tendons results were re-used from table 5.1. The comparison with the 2D isolated tendons uniaxial tensile test results was preferred due to the higher possibility of errors introduced by the extensometer and due to the lower relative error obtained for the uniaxial tensile test comparison.

(Fig. 5.10 (a-b)). Results obtained along the elevation direction did not present any correlation with the ground-truth values (Fig. 5.10 (c)). For this data, the reported MAE, MRE, MAD and NSE were lower along the axial direction than along the lateral direction (Table 5.1).

Due to the absence of 2D global strain estimations of in-vitro data, the comparison of the performance of 2D vs. 3D estimations was not possible.

3D isolated tendons global strain estimations

Validation based on isolated tendons data showed the lowest correlations (Fig. 5.10 (d-f)) and highest MAE with the exception of the axial direction (Table 5.1). High MRE were obtained for this type of data ranging from 69.77% to 189.81%. The best results for this type of data were obtained along the axial direction.

Comparison between 2D and 3D global strain estimations of isolated tendons data showed that larger errors were obtained for 3D data (Table 5.1).

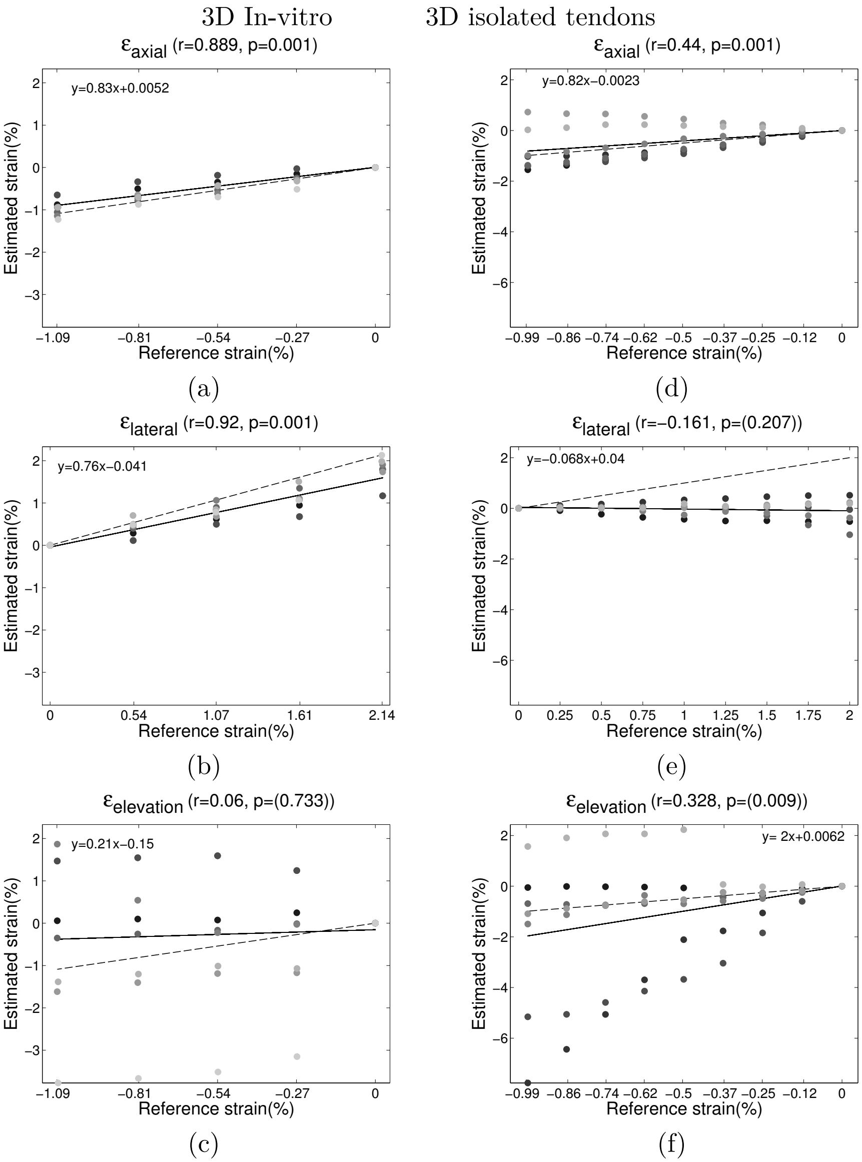

(a) (d)

(b) (e)

(c) (f)

Figure 5.10: Scatter plots of regional strain estimation of 3D in-vitro data (a-c) and 3D isolated tendons data (d-f) along axial, lateral and elevation direction, respectively. Different gray shades represent different experimental samples/subjects. The dashed line on the scatter plots represents the line of identity, and the solid line represents the linear fitting to the data.

5.4 Discussion

In this section, the performance of 3D vs. 2D global strain estimation methods is compared. An initial comparison is performed between 3D and 2D global strain estimations for in-silico data followed by the comparison of 2D and 3D global strain estimations for in-vitro and isolated tendons data. At the end, the main limitations found in this work are presented.

5.4.1 3D performs better than 2D

Results obtained for in-silico 3D strain estimations show a reduction in strain estimations errors of 26% along the axial direction and of 21% along the lateral direction, when compared with the results for 2D data. These results seem to, for the first time, exemplify the impact of the out-of-plane motion on strain estimation as hypothesized in the literature [34, 35, 165].

5.4.2 3D strain estimations for in-vitro and isolated tendons data

Lowest errors for in-vitro data were obtained along the axial direction. These errors increase along the lateral direction and are largest along the elevation direction. The smaller strain estimation errors obtained along the axial direction are likely related to the higher spatial resolution of the US acquisition system along the axial direction.

Larger strain estimation errors were found for isolated tendons data. This increase can be related to the increased data complexity, possible non-uniform deformation, and presence of imaging artifacts. For this type of data, the lateral and elevation directions show the largest relative estimation errors (102.08% and 189.81%, respectively). Best estimations for this type of data are obtained along the axial direction. However, the strain estimation errors obtained along the axial direction for the isolated tendons data were worse than any of the results obtained for in-silico and in-vitro data.

Comparison between previously estimated 2D global strain estimations of isolated tendons data and the 3D global strain estimations show that the performance of the 3D method is worse than the 2D method. However, when comparing these two results, it should be taken into consideration that the acquisition conditions were different for the two tests. 2D global strain was estimated between 0% and 5% strain while the 3D global tendon strain estimations were calculated between 2% and 4%. Moreover, the temporal resolution used for the acquisition of 2D vs. 3D images was substantially different. 2D global strain estimations were performed using 2D+t images, acquired with a frame-rate of 100fps, while the 3D data was acquired using a semi-dynamic loading protocol. These differences in temporal resolution between consecutive pairs of frames/volumes can negatively affect the pairwise image registration and can lead to significant out-of-plane motion, which can as well induce tendon strain estimation errors.

After taking into consideration all of those factors, the worse performance of the 3D method in comparison with the 2D method is still surprising. Moreover, the obtained results also show that the elevation direction presents the highest strain estimation errors for in-vitro and isolated tendons data.

It was then hypothesized that both the worse performance of 3D global strain estimations and the large estimation errors obtained along the elevation direction were indeed influenced by the possible insufficient reproducibility of the 3D HS US acquisition process. It was hypothesized that this insufficient reproducibility was influenced by the friction between the transducer and scanned surface. If this would occur, 3D HS US images could be acquired with skewed or overlapping frames or even frames, which have a distance between each other larger than the distance defined by the step-size. Alternatively, it was also hypothesized that pressure applied to the scanned surface would also deform the scanned surface, which would then change its aspect.

The insufficient reproducibility of the 3D HS US acquisition system was investigated by testing two different acquisition conditions. The first condition described the use of different contact media for the acquisition of 3D HS US images while the second condition evaluated the impact of applying pressure to the surface while acquiring the 3D HS US images (see appendix E). These tests showed that strain estimations along the elevation direction were influenced by changes in the used contact medium and by the pressure applied while acquiring images.

5.4.3 Limitations

The principal limitation for 3D global strain estimation was found when acquiring 3D in-vitro and 3D isolated tendons data. These limitations were mainly due to the insufficient reproducibility of the 3D HS US acquisition process as discussed above.

Another limitation of the 3D HS acquisition system was the low temporal resolution between consequent 3D volumes, which influences negatively the image registration process due to the lower speckle correlation between volumes.

Attempts were made to increase the temporal resolution for the acquisition of 3D US data using the Vevo 2100 by replacing the step-by-step scanning method by a continuous scanning method. After consultation with VisualSonics, we were informed that the speed of the motor could not be increased because that could lead to the motor skipping steps and producing spatially inaccurate images. Another attempt to increase the speed was the reduction of the acquisition time of each 2D frame. After investigation of this issue, an idle time of 5ms was detected for the acquisition of each 2D US frame while the actual acquisition time of a 2D US frame with 220 lines, depth of 21mm and width of 23mm, was approximately 6ms. After consulting with VisualSonics, we were told that such idle time was intended to prevent echoes beyond the depth of interest of interfering with the quality of the data and this could not be changed.

Besides being affected by the acquisition of low-temporal resolution and low-reproducible 3D images, the acquisition, and consequent 3D global tendon strain estimations, of 3D isolated tendons data may also be affected by the stress-relaxation behavior of the tendon. The acquisition of each 3D HS US isolated tendons image takes approximately 3 seconds. For a good acquisition and consequent good registration, the tendon should be stable without undergoing any deformation during these three seconds. However, Duenwal *et al.* [59] showed that tendon relaxation starts as soon as the tendon is held stable while enduring load. Duenwal *et al.* [59] also showed that the larger the applied strain, the faster, and the more significant relaxation occurs. Contextualizing this relaxation in the acquisition of 3D isolated tendons images, it is possible that by acquiring semi-dynamic images of isolated tendons, strain estimation inaccuracies were also being introduced.

Another limitation, which does not affect any of the results here presented but which is important to report, is related to the acquisition of in-vivo 3D HS US images. For the sake of completeness, attempts were made to acquire 3D HS US in-vivo images. The images obtained during this attempt confirmed the same acquisition challenges mentioned for the acquisition of 3D HS US isolated tendons data. Moreover, the relaxation effects demonstrated for the isolated tendons situation would also affect the in-vivo acquisition. This acquisition would even be worsened by the difficulty of a person applying a load to the tendon while staying still completely.

Figure 5.11 shows an example of an in-vivo 3D HS US image where the effect of incomplete immobilization of the volunteer and difficulties keeping the contact are illustrated. Red arrows point out the image acquisition artifacts.

In order to attempt to improve the immobilization of the Achilles tendon for the 3D acquisition of in-vivo images, a prototype of a mechanical device for the elongation of in-vivo Achilles tendon was built. This device allowed the

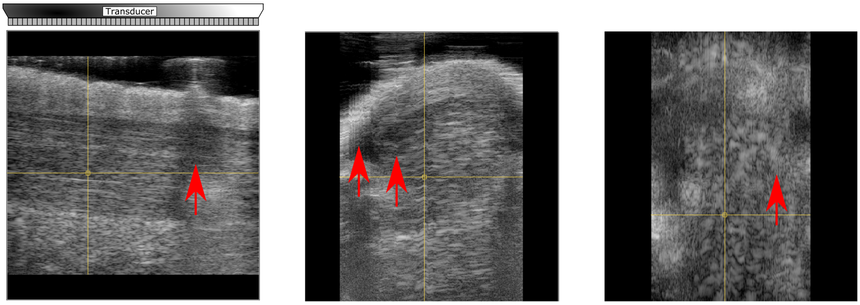

(a) (b) (c)

Figure 5.11: Example of 3D US in-vivo image. (a) represents the in-plane simulation, (b) the transverse plane and (c) the coronal plane. Arrows point out acquisition artifacts present in these images, such as reduced contact visible in (a) and motion artifacts, visible in (b) and (c).

elongation of the tendon by changing the angle of the ankle, as represented in Fig. 5.12. A set of straps was used to limit the displacement and rotation of the foot and leg. However, this system turned out to introduce too much leg motion, due to the complicated process of changing the angles of the device. This motion lead to too much out-of-plane motion, limiting in this way the acquisition of images of good quality.

Due to these acquisition artifacts, the use of this setup was abandoned.

5.5 Concluding remarks

In this part of the work, the impact of out-of-plane motion for tendon strain estimations was investigated.

Results obtained for in-silico data showed that there is an error reduction when estimating tendon strain using 3D HS US images instead of 2D. However, with the increasing complexity of the data and the increasing complexity of the acquisition setup, the acquisition of 3D HS US images becomes very challenging. Furthermore, it is also believed that the use of low-temporal resolution data had an important negative effect on the performance of the image registration method due to speckle decorrelation.

Nevertheless, it is believed that once a 2D high-spatial resolution US transducer array is available, this method could be directly applied to these images for 3D

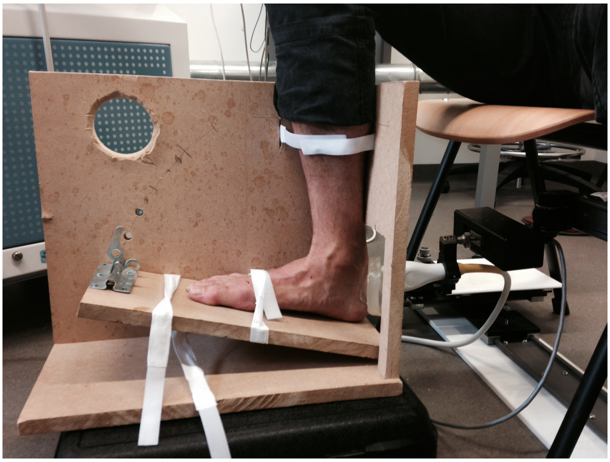

Figure 5.12: In-house built mechanical device for elongation of the Achilles tendon. Range of motion is highlighted by dashed line and the different elongation angles are highlighted by white circles. The transducer is initially aligned with the central axis of the Achilles tendon and the 3D motor is used to acquire 3D US images.

global tendon strain estimations.

Chapter 6

Discussion and conclusion

In this discussion, the three clinical questions raised in the introduction are discussed through the obtained results.

The first clinical question which motivated the work here presented was: "**How can we quantify the biomechanical properties of the Achilles tendon in-vivo?**".

Inter-fiber and inter-fascicle sliding has been reported in literature as one of the most important mechanisms responsible for the straining and elongation of the Achilles tendon. This sliding is represented, macroscopically, by the non-uniform tissue deformation of different layers of the Achilles tendon. Microscopically, sliding has also been reported to occur at the fascicle level.

In order to answer the question raised, an image registration approach was used in this work. This image registration approach is believed to be valid for the estimation of this type of sliding. However, care should be taken when defining the weight of the penalty term used. If a large regularization of the displacement field is done, registration errors could be introduced near shear regions. Interestingly, the parameter sensitivity test that investigated the impact of the choice of different weights for similarity and regularization, demonstrated that the presented image registration method does not strongly depend on the selection of this term. These results allow then hypothesizing that the intrinsic displacement of speckle patterns, acquired with high temporal resolution, leads to intrinsically smooth deformation patterns.

The use of a B-spline transformation was preferred mainly due to its local support and fast computations without invalidating the applicability of other transformation models for the quantification of the biomechanical properties of the Achilles tendon. Among these alternatives, local affine registration could have been applied. However, it was believed that this approach would not yield better results since, in a sense, the use of affine transformations locally would yield information which would be equivalent to the information obtained due to the local support of the B-spline transformation.

The selection of the image registration parameters used for the developed method was performed according to the theoretical differences of each and according their qualitative performance. The absence of ground-truth for the in-vivo data prevented a more in-depth evaluation of the performance of these parameters. Because of this, the performance of the presented method was evaluated visually, by comparison of the obtained speckle tracking results, and by evaluation of the biomechanical properties estimated within each of the selected sub-ROIs. The design of this region of interest was defined together with clinicians, who have diagnosed and evaluated many asymptomatic and symptomatic tendons. Due to this, the design of these sub-ROIs is believed to be clinically relevant and appropriate. The sensitivity test performed regarding the positioning of the ROI along the lateral direction demonstrated no significant differences, be it with a reduced statistical power. Results obtained in the literature have demonstrated larger strain estimations in distal regions of the Achilles tendon, in comparison with more proximal regions. In this way, it would seem logical to obtain statistical differences depending on where the ROI is defined. However, that was not the intention of this work. Due to the very limited field of view of the used transducer, the ROIs were always placed medially, from distal to proximal, to insure that the ROIs would stay within the field of view during the selected interval of interest. Moreover, the transducer was always placed in the same region of the tendon, which insured that the central region of the tendon was always the same. Because the sliding effect reported in the literature occurred from the superficial region of the tendon to the deep region, investigation of changes of the positioning of the ROIs along the axial direction was not attempted.

Regarding the interobserver variability, the low statistical power obtained for this evaluation demonstrates the difficulty of manually tracking speckles which in turn demonstrates the important role of the developed speckle tracking methods.

In conclusion, this work demonstrates that the use of an image registration approach is valid for the quantification of the biomechanical properties of in-vivo Achilles tendons.

Regarding the second clinical question that motivated this work: "**How can we improve the performance of our method, in comparison with**

the state-of-the-art?", a multifactorial approach was followed. Attempts to improve the quality of the estimated biomechanical properties of the Achilles tendon were firstly done at the level of the imaging acquisition system, and secondly at the level of the method developed for the quantification of these biomechanical properties.

In first instance, instead of using conventional ultrasound imaging, high-spatial resolution ultrasound imaging was used for the acquisition of both 2D US images as for the acquisition of 3D US images. As demonstrated during this work, by using a higher-spatial resolution imaging system it is hypothesized that smaller tendon structures can be acquired, in comparison with the larger structures acquired with conventional ultrasound imaging. In this way, the quantification of the displacement of smaller structures is possible, which may lead to the characterization of the tendon biomechanics at finer scales. The acquisition of 2D dynamic images was also performed at higher temporal resolutions, in comparison with the conventional US imaging methods used in the literature. The use of higher-temporal resolution acquisition systems has been reported to lead to lower speckle decorrelation and better performance of the speckle tracking method due to the similarity between speckle patterns in consecutive frames.

The same high-spatial resolution US imaging system used for the acquisition of 2D US images was also used for the acquisition of 3D high-spatial resolution US images. The motivation behind the use of a 3D high-spatial resolution US imaging system for the quantification of the biomechanical properties of the Achilles tendon is the investigation of the impact of out-of-plane motion. This type of artifacts has been shown to strongly affect the quantification of the biomechanical properties of the Achilles tendon when 2D US images are used. The obtained results demonstrated the theoretical improvement of strain quantifications using 3D high-spatial imaging but the use of a semi-3D US acquisition system, rather than a "real" 3D US imaging system prevented good performance of this approach for isolated tendons. Moreover, the acquisition of semi-3D US images also prevented the applicability of this approach for the acquisition of 3D US images in-vivo.

Secondly, improvements to the quality of the quantification of the biomechanical properties of the Achilles tendon were also attempted by using a speckle tracking method different than the methods commonly used in literature. As presented in the introduction, there are several approaches commonly used in literature, which attempt to quantify the biomechanical properties of the Achilles tendon, and the mentioned sliding effect. However, the approach chosen to perform this task was an image registration method. The reason for this lies in the good performance of such methods for similar applications, but the scarce attempts of applying image registration methods for the characterization of the biomechanical properties of the Achilles tendon. Tests performed in isolated tendons demonstrated a better performance of the developed affine image registration method, in comparison with the literature. However, the characterization of the biomechanical properties of the Achilles tendon in-vivo demonstrated an estimation of the tendon deformation pattern equivalent to the one reported in the literature, but with lower absolute values. This difference is hypothesized to be associated with the differences in protocols used for the elongation of the Achilles tendon and for the differences in the used imaging acquisition system. As explained before, the use of a US imaging system with spatial resolution is believed to lead to the tracking of smaller tendon structures, in comparison to the tracking of larger structures when using conventional imaging systems. Due to this, it is possible that by using a higher frequency system, different structures are being tracked; hence different absolute values are estimated.

The developed image registration method is part of a global attempt to improve the quantification of the biomechanical properties of the Achilles tendon in-vivo. In this way, the performance of the image registration method is intricately associated with the use of the high-spatial resolution ultrasound imaging system, which makes the comparison between this method and the methods reported in the literature difficult. Furthermore, the absence of ground-truth makes this comparison even more difficult.

Interesting methods that do not rely on the tracking of speckle patterns for the characterization of the tendon biomechanics have also been presented lately. Elastography is an example of such methods. Despite the interesting results reported by elastography methods, it is believed that such approach for tendon applications is still in an early research phase. In this way, the interpretation of the obtained results is not always straightforward. Furthermore, high inter-observer variability has also been reported for elastography methods. In a different line of research, ultrasonographic tissue characterization (UTC) has also been investigated for application in the diagnosis of tendinopathic tendons with good success. However, besides returning limited biomechanical information, this approach has also not been demonstrated to be useful for the early detection of tendinopathy cases.

In conclusion, the comparison of the performance of the developed method with the methods presented in literature is challenging due to the absence of ground-truth. However, the quantification of the biomechanical properties of the Achilles tendon at finer scales, allowed by the acquisition of higher-spatial resolution images, is believed to be an advantage for the functional description of these tendons. Another conclusion that can be extrapolated from these results is that combining the acquisition of 2D high-spatial and high-temporal resolution US images with the developed B-spline image registration method, allowed physiological meaningful quantifications of regional tendon strain.

Concerning the third clinical question that motivated this work: "**Are the obtained results clinically meaningful and can these be used for tendinopathy diagnosis?**", the following conclusions can be drawn. Firstly, the obtained tendon tissue deformation patterns obtained with the presented work are similar to the results reported by others in literature. Although this does not represent a "true validation", the absence of ground-truth for in-vivo data prevents a better validation. However, as explained above, the absolute tendon tissue displacements obtained with the developed method are smaller than the ones reported in literature. During this work it was also hypothesized that larger speckle patterns represent larger tissue structures while smaller speckles represent smaller tendon structures. In this way, the tissue displacement estimated by other methods represent the displacement of larger structures, while the results obtained by the presented method represent the displacement of smaller structures, such as fascicles and fibers. An example of the scale dependency that occurs at the level of the biomechanical properties of the Achilles tendon is the appliance of a maximum gross strain of 8% and the quantification of a maximum of 1.2% strain at the microscopical level [191]. In this way, larger speckle patterns, hence larger tendon structures, may be representing tendon structures which displace more while smaller speckle patterns, hence smaller tendon structures, may be representing tissue that undergoes smaller displacements.

When evaluating the results obtained for the symptomatic volunteers, a reduction of the sliding effect between the three different layers of the Achilles tendon was seen. This reduction is higher in medium to severe cases of tendinopathy and these results seem to be in line with the results reported for ageing tendons, both at a microscopical level as well as at macroscopical level. In this way, it seems logical to assume that sliding between sub-tendons and between fascicles/fibers represent an important factor for optimal functioning of the Achilles tendon. Interestingly, in the case of surgically repaired tendons, this sliding effect has been reported to be reduced, which demonstrates that these tendons will probably present with impaired biomechanical function. Besides the reduction of tendon sliding, medium and severe tendinopathic tendons also presented with larger tissue displacement estimations. Similarly, large tissue displacement estimations have also been reported in literature and it has been hypothesized that this change would be caused by an increase of the compliance of ageing and symptomatic tendons.

Due to the absence of ground-truth, a psychometric validation was performed and the results obtained for the biomechanical characterization of Achilles tendons in-vivo provided evidence of predictive, convergent and discriminant validity, and a reduced but present discrimination power.

In conclusion, the characterization of the biomechanical properties of Achilles tendon in-vivo presented in this work is believed to bring a new insight into the functional role of the Achilles tendon and its different deformation patterns both in asymptomatic as well as symptomatic tendons.

The last goal of this manuscript was the **development of a user-friendly application**, which would allow a non-technical expert to investigate the biomechanical properties of the Achilles tendon. To address this goal, a modular application was designed and the developed image registration method was embedded into it. A non-technical expert is currently using such an application and its success can be demonstrated by the absence of processing issues/errors during 3 months of usage. The main pitfall of the developed application is the processing time, which could be addressed for instance, by reducing the number of multi-resolution levels used for the image registration process. The only prerequisite of this application is that the input image corresponds to a cine image stored in NIfTI-1 format. Naturally, the quality of the data acquired influences directly the results obtained by the image registration method. A prerequisite for the acquisition of good quality images is the proper fixation of the transducer to the leg is recommended. This fixation is important to insure that the imaged structures remain in-plane during the dynamic movement. Another requirement that should be strongly considered is the selection of relevant intervals of interest and the alignment of the selected ROI with the major deformation direction of the tendon.

Chapter 7

Future Work

As mentioned before, the knowledge of tendon mechanics and the etymology of tendinopathy are not yet completely understood. One of the latest hypotheses [77] is that tendinopathies are associated with the degree of inter-fascicle and inter-fiber sliding.

Inter-fascicle sliding has been firstly reported by Mosler *et al.*, Fratzl *et.al* and Purslow *et.al* [160, 78, 181]. In these studies, it was demonstrated that the tendon deformation in the linear region could occur either through stretching of the collagen components (e.g. collagen triple helices) or stretching of the cross-links between the collagen fibers. The latter implies the occurrence of a side by side gliding between the adjacent components. More recently, Screen *et al.* [191] demonstrated that fiber sliding provides the major mechanism for fascicle extension and this sliding increases directly with the increase of tendon strain. Also, Thorpe *et al.* [209] investigated inter-fiber sliding in equine models and found that the inter-fascicular sliding decreases with aging in energy-storing tendons, such as the Achilles tendon, while no significant difference was found for positional tendons, such as the extensor digitorum tendons in the hand. The same author hypothesized also that the high predisposition to an injury of energy-storing tendons, in comparison to positional tendons, may be likely due to the extremely high strains these tendons experience in vivo.

This chapter is divided into three sections which describe three different tests which would be of interest to be further investigate.

7.1 Investigation of fiber- and fascicle-sliding effect

One of the next steps in the field of the characterization of local tendon mechanics is then the investigation of the correlation between tendon strain and inter-fiber as well as inter-fascicle sliding. A possible strategy for the initial investigation of this inter-fiber and inter-fascicle sliding is described below.

An initial in-silico study was done to demonstrate the concept of fiber sliding. The constructed model had a dimension of [5,20,5]mm along the axial, lateral and elevation direction, respectively. The US settings used for this in-silico study were the same as the ones of the 21 MHz transducer from the Vevo 2100.

The model was then divided, along the axial direction, to accommodate the desired number of parallel structures, which were intended to represent fibers. The sliding and straining effects were achieved by displacing points of adjacent structures with inverse displacement directions. Five models were deformed using strain values between 0-5% strain with incremental steps of 1% strain. The last step was the simulation of 2D HF US images using the five different models.

Figure 7.1 exemplifies the initial results for the tendon structure sliding effect test using 3, 5, 10 and 20 parallel sliding/straining structures [1].

The structures presented in Fig. 7.1(a) have a thickness of 1.6 mm (three times larger than the tendon), in Fig. 7.1(b) a thickness of 0.5 mm (equivalent to tendon dimensions), in Fig. 7.1(c) a thickness of 0.25 mm and in Fig. 7.1(d) a thickness of 0.1 mm, respectively.

The local tendon mechanics characterization method proposed in this dissertation can easily be adapted to investigate the mentioned tendon fiber sliding effect. This adaptation was not performed but it would be a two-step process. Firstly, the B-spline control points should be placed in a highly anisotropic grid where long and thin segments would be aligned with the tendon fiber direction. The second step would be the adaptation and tuning of the regularization penalty term to allow the "sliding" of the segments along the loading direction while penalizing axial deformation.

---

[1] Tracking videos are available in digital version

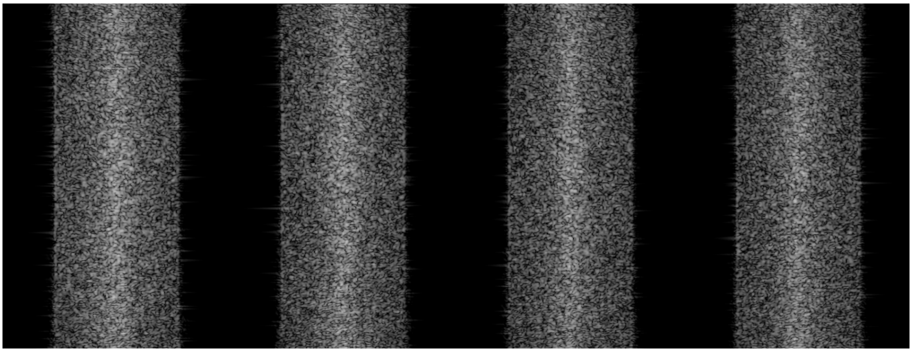

Figure 7.1: Example of tendon structure sliding effect simulated using a 21 MHz transducer. From left to right, the first video shows a model with 3 structures, the second video shows a model with 5 structures, the third video shows a model with 10 structures and the fourth video shows a model with 20 structures. For all these models, the displacement of adjacent structures is inverse. Tracking videos are available in digital version.

7.2 Investigation of influence of different US acquisition systems for the detection of fiber- and fascicle-sliding effect

Another complementary and interesting study would be to demonstrate the influence of the choice of the US acquisition system and US acquisition capability of capturing deformations at different scales, of the different structures of the tendon.

An initial simulation, of the same 3D Matlab model discussed before, with the simulation parameters of a 10 MHz US system is shown in Fig. 7.2 [2].

In this figure, more speckle decorrelation is visible than in Fig. 7.1, and the sliding effect in (c) and (d) is not visible.

---

[2] Videos are available in digital version

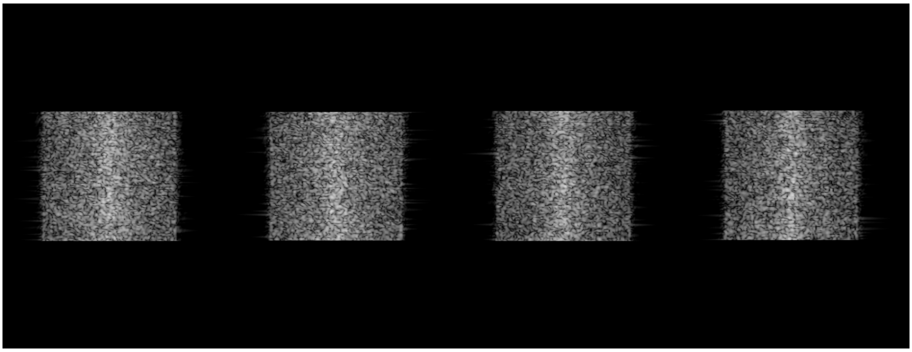

Figure 7.2: Example of tendon structure sliding effect using a 10 MHz transducer. From left to right, the first video shows a model with 3 structures, the second video shows a model with 5 structures, the third video shows a model with 10 structures and the fourth video shows a model with 20 structures. For all these models, the displacement of adjacent structures is inverse. Tracking videos are available in digital version

7.3 Improvement of 3D high-spatial resolution US acquisition

Future work in the area of 3D tendon strain estimation includes the implementation of a 3D HF US image reconstruction strategy along the elevation direction. This reconstruction could be achieved by tracking the movement of the probe and including that information in the image reconstruction process. By doing so, current errors related to the increased friction and uneven step-size of the motor would be ameliorated. However, it is believed that characterization of tendon mechanics using 3D mechanically guided US will always be limited due to the low temporal resolution that can be achieved using this type of systems, and by the stress-relaxation behaviour, which is assumed to affect tendons subject to semi-dynamic loading protocols.

Appendix A

2D Affine parameter file

```
(FixedInternalImagePixelType "float")
(MovingInternalImagePixelType "float")
(UseDirectionCosines "true")
(Registration "MultiResolutionRegistration")
(Interpolator "BSplineInterpolatorFloat")
(ResampleInterpolator "FinalBSplineInterpolatorFloat")
(Resampler "DefaultResampler")
(FixedImagePyramid "FixedRecursiveImagePyramid")
(MovingImagePyramid "MovingRecursiveImagePyramid")
(Optimizer "QuasiNewtonLBFGS")
(Transform "AffineTransform")
(Metric "AdvancedMeanSquares")
(LinearityConditionWeight 10)
(OrthonormalityConditionWeight 1)
(PropernessConditionWeight 100)
(FixedRigidityImageName "")
(MovingRigidityImageName "")
(AutomaticScalesEstimation "true")
(AutomaticTransformInitialization "true")
(AutomaticTransformInitializationMethod "GeometricalCenter")
(HowToCombineTransforms "Compose")
(FinalGridSpacingInPhysicalUnits 16)
(FinalGridSpacingInVoxels 16)
(OutlierDistributionKappa 3)
(Temperature 100)
(UseSpatialConstraints "true")
(NeighborhoodRadius 3)
(NumberOfHistogramBins 32)
(ErodeFixedMask "true")
(ErodeMovingMask "true")
(NumberOfResolutions 3)
(MaximumNumberOfIterations 100)
(MaximumStepLength 1)
```

```
(NumberOfSpatialSamples 10000)
(CheckNumberOfSamples "true")
(NewSamplesEveryIteration "true")
(ImageSampler "Random")
(MaximumNumberOfSamplingAttempts 5)
(BSplineInterpolationOrder "3")
(FinalBSplineInterpolationOrder "3")
(DefaultPixelValue 0)
(WriteResultImage "false")
(ResultImagePixelType "float")
(ResultImageFormat "nii")
(WriteTransformParametersEachIteration "false")
(WriteTransformParametersEachResolution "false")
(WriteResultImageAfterEachResolution "false")
(ShowExactMetricValue "false")
```

Appendix B

B-spline parameter file

```
(FixedInternalImagePixelType "float")
(MovingInternalImagePixelType "float")
(UseDirectionCosines "true")
(Registration "MultiMetricMultiResolutionRegistration")
(Interpolator "BSplineInterpolatorFloat")
(ResampleInterpolator "FinalBSplineInterpolatorFloat")
(Resampler "DefaultResampler")
(FixedImagePyramid "FixedRecursiveImagePyramid")
(MovingImagePyramid "MovingRecursiveImagePyramid")
(Optimizer "QuasiNewtonLBFGS")
(Transform "BSplineTransform")
(Metric "AdvancedMeanSquares" "TransformBendingEnergyPenalty")
(Metric0Weight 0.5)
(Metric1Weight 0.5)
(UseLinearityCondition "false")
(UseOrthonormalityCondition "false")
(UsePropernessCondition "false")
(CalculateLinearityCondition "false")
(CalculateOrthonormalityCondition "false")
(CalculatePropernessCondition "false")
(DilateRigidityImages "false")
(UseFixedRigidityImage "false")
(FixedRigidityImageName "")
(UseMovingRigidityImage "false")
(AutomaticScalesEstimation "true")
(AutomaticTransformInitialization "true")
(AutomaticTransformInitializationMethod "GeometricalCenter")
(HowToCombineTransforms "Compose")
(UseSpatialConstraints "true")
(NeighborhoodRadius 3)
(NumberOfHistogramBins 32)
(ErodeFixedMask "true")
```

```
(ErodeMask "true")
(ErodeMovingMask "true")
(NumberOfResolutions 3)
(MaximumNumberOfIterations 250)
(MaximumStepLength 1)
(NumberOfSpatialSamples 2048)
(CheckNumberOfSamples "true")
(NewSamplesEveryIteration "true")
(ImageSampler "RandomSparseMask")
(MaximumNumberOfSamplingAttempts 10)
(BSplineInterpolationOrder "1")
(FinalBSplineInterpolationOrder "3")
(DefaultPixelValue 0)
(WriteResultImage "true")
(ResultImagePixelType "float")
(ResultImageFormat "nii")
(WriteTransformParametersEachIteration "false")
(WriteTransformParametersEachResolution "false")
(WriteResultImageAfterEachResolution "false")
(ShowExactMetricValue "false")
```

Appendix C

Regional strain calculations

Because of the interest in local strain estimation, each pair of regions (proximal/distal) was used for regional strain calculation as demonstrated in Fig. C.1. The displacement of the top and the bottom part is then estimated and strain is computed using these two values between the initial frame and the consecutive.

L_0 corresponds to the initial distance between the central line of the proximal and distal regions. Equation C.3 gives an example for the calculation of regional strain between a proximal and a distal region:

$$L_{final} = L_0 - (\Delta_{proximal} - \Delta_{distal}) \tag{C.1}$$

$$\mathcal{E} = \frac{L_0 - (\Delta_{proximal} - \Delta_{distal}) - L_0}{L_0} \times 100 \tag{C.2}$$

$$\mathcal{E} = -\frac{(\Delta_{proximal} - \Delta_{distal})}{L_0} \times 100 \tag{C.3}$$

The validity of this formulation is evaluated using different average displacement estimations, for proximal (R3) and distal region (R6), as presented in table C.1:

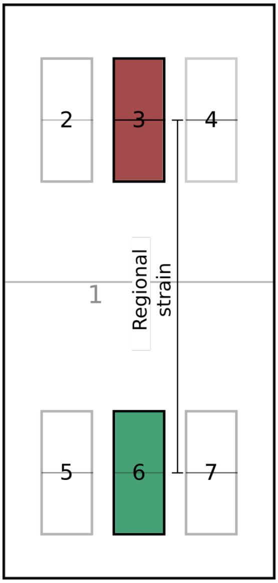

Figure C.1: Example of two regions, proximal and distal, used for the calculation of regional strain.

Table C.1: Regional strain estimation between R3 and R6 for different regional average tissue displacement

Case	Δ_{R3}(mm)	Δ_{R6}(mm)	ε	illustration
1	-2	+2	$\frac{4}{L_0} \times 100$	Fig.C.2(a)
2	+1	-1	$\frac{-2}{L_0} \times 100$	Fig.C.2(b)
3	+6	+2	$\frac{-4}{L_0} \times 100$	Fig.C.2(c)
4	-2	-6	$\frac{-4}{L_0} \times 100$	Fig.C.2(d)
5	-6	-2	$\frac{4}{L_0} \times 100$	Fig.C.2(e)
6	+2	+6	$\frac{4}{L_0} \times 100$	Fig.C.2(f)

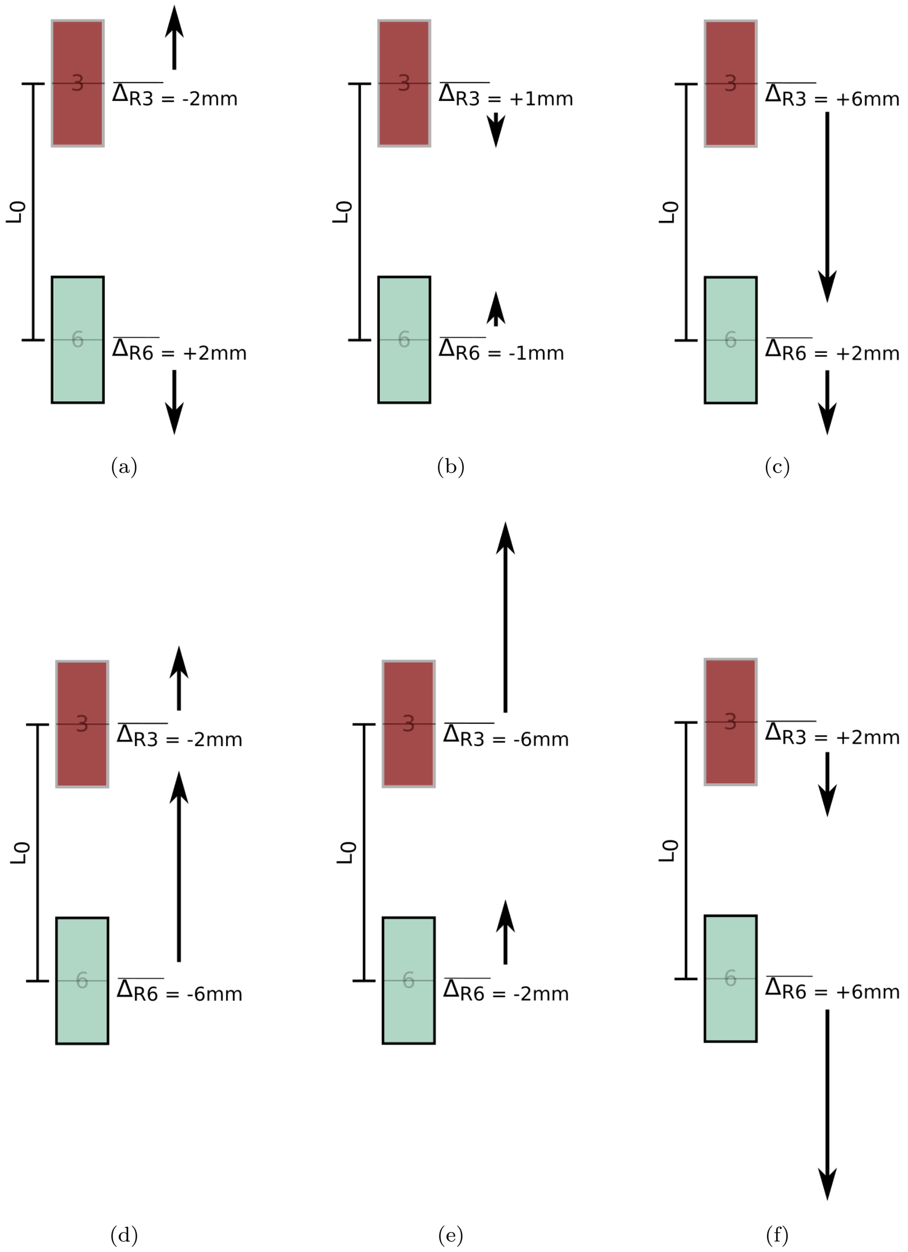

Figure C.2: Strain estimation explanation. Illustration of case 1 (a) to case 6 (f).

Appendix D

3D Affine parameter file

```
(FixedInternalImagePixelType "float")
(MovingInternalImagePixelType "float")
(UseDirectionCosines "true")
(Registration "MultiResolutionRegistration")
(Interpolator "BSplineInterpolatorFloat")
(ResampleInterpolator "FinalBSplineInterpolatorFloat")
(Resampler "DefaultResampler")
(FixedImagePyramid "FixedRecursiveImagePyramid")
(MovingImagePyramid "MovingRecursiveImagePyramid")
(Optimizer "QuasiNewtonLBFGS")
(Transform "AffineTransform")
(Metric "AdvancedMeanSquares")
(LinearityConditionWeight 10)
(OrthonormalityConditionWeight 1)
(PropernessConditionWeight 100)
(FixedRigidityImageName "")
(MovingRigidityImageName "")
(AutomaticScalesEstimation "true")
(AutomaticTransformInitialization "true")
(AutomaticTransformInitializationMethod "GeometricalCenter")
(HowToCombineTransforms "Compose")
(FinalGridSpacingInPhysicalUnits 16)
(FinalGridSpacingInVoxels 16)
(OutlierDistributionKappa 3)
(Temperature 100)
(UseSpatialConstraints "true")
(NeighborhoodRadius 3)
(NumberOfHistogramBins 32)
(ErodeFixedMask "true")
(ErodeMovingMask "true")
(NumberOfResolutions 3)
(MaximumNumberOfIterations 100)
(MaximumStepLength 1)
```

```
(NumberOfSpatialSamples 10000)
(CheckNumberOfSamples "true")
(NewSamplesEveryIteration "true")
(ImageSampler "Random")
(MaximumNumberOfSamplingAttempts 5)
(BSplineInterpolationOrder "3")
(FinalBSplineInterpolationOrder "3")
(DefaultPixelValue 0)
(WriteResultImage "false")
(ResultImagePixelType "float")
(ResultImageFormat "nii")
(WriteTransformParametersEachIteration "false")
(WriteTransformParametersEachResolution "false")
(WriteResultImageAfterEachResolution "false")
(ShowExactMetricValue "false")
```

Appendix E

Contact media

Our hypothesis was that the contact medium used and acquisition conditions influenced the reproducibility of the acquisition system. In order to investigate this hypothesis, a reproducibility test was designed in which an agar-phantom was stabilized and 3D high-spatial US images were acquired using different contact media.

Five images were acquired while using each contact medium and care was taken that the acquisition parameters were unchanged throughout the different repetitions. Each of the four different contact media used to test this hypothesis corresponded to a test. In the first test, the phantom was immersed and stabilized inside a container that was subsequently filled with tap water. In the second test, the water was replaced by gel and the same acquisition procedure was used. In the third test, a gel pad was added to the gel used before. In the fourth test, the transducer was forced to apply pressure to the contact medium. In a clinical setup, this last testing condition is relevant since the movement of the foot or pulling of the muscle may change the pressure between transducer and contact medium. The five 3D images collected from each test condition were registered pairwise among each other and strain estimations deviating from 0% were considered as errors.

For the first and second test conditions, results showed (Fig. E.1 (a-b)) similar errors ranging between -0.15% and 0.1% strain along the three directions. Between the second and third testing conditions, there was an increment of the error along the elevation direction. This error was at its highest when pressure was applied, ranging between -6% and 6% of strain. As this test showed, strain estimations along the elevation direction were influenced by changes in the used contact medium and by the pressure applied while acquiring the images.

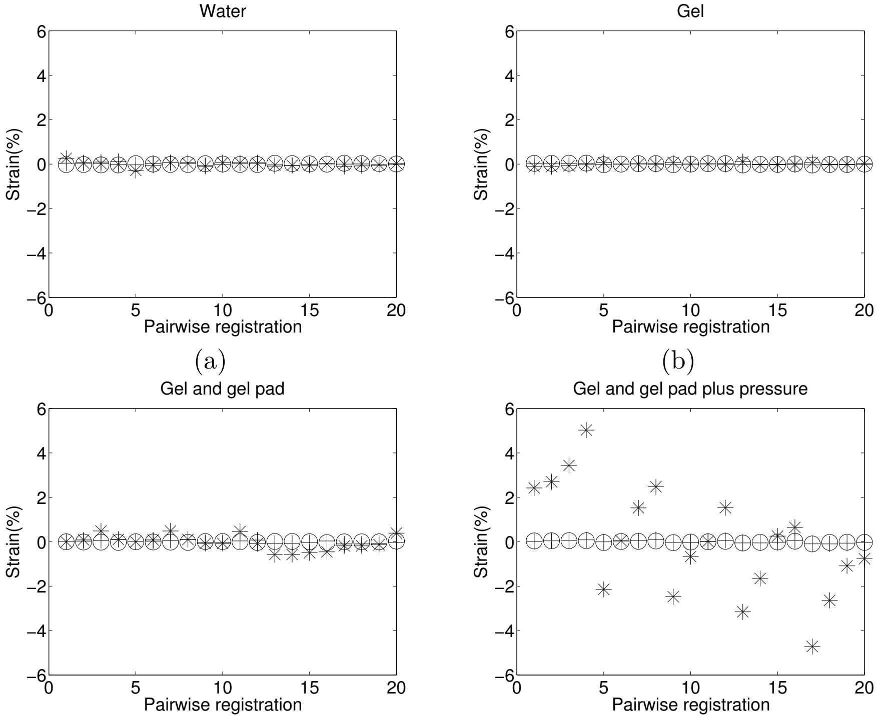

(a) (b)

(c) (d)

Figure E.1: Acquisition errors using different contact media. (a) water, (b) contact gel, (c) contact gel and gel pad, (d) contact gel, gel pad and applied pressure. ε_{axial} is represented by $+$, $\varepsilon_{lateral}$ is represented by $\circ$ and $\varepsilon_{elevation}$ is represented by $*$.

Friction between the transducer and the scanned surface may produce skewed, overlapping or far apart frames. Pressure can also deform the scanned surface changing its aspect.

An example of these acquisition artifacts is demonstrated in Fig. E.2. In this figure, the coronal planes of two consecutively acquired images were overlaid in the RGB color space. In other words, when the two images were identical, the color yellow is obtained. When this did not occur, either green or red was presented.

Extra information is given in Fig. E.3 where the consecutive 3D acquisition time of two phantoms is demonstrated. This plot shows a clear a fluctuation of the acquisition time (between 2.4 and 2.9 seconds) which confirmed the hypothesis

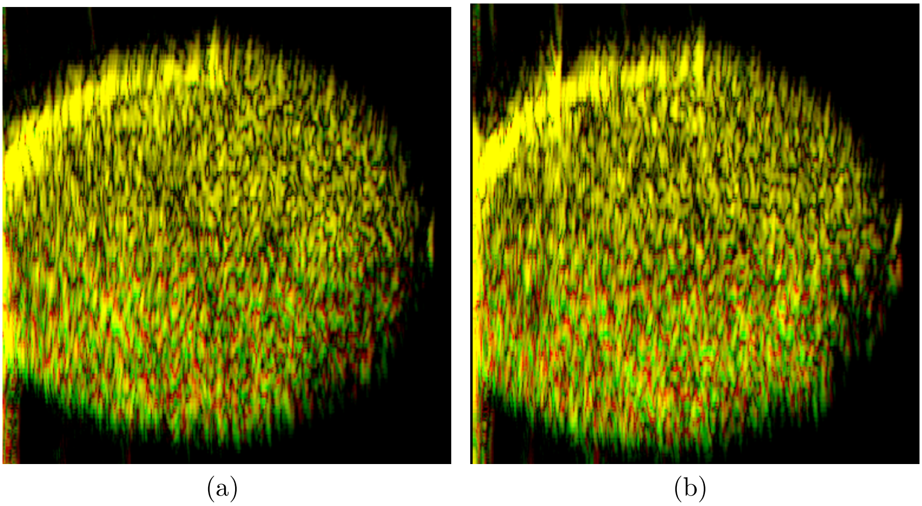
(a) (b)

Figure E.2: Example of two overlays of two consecutively acquired images along the coronal plane. One of the compared images is represented in red, the other in green and the overlap of both images is represented in yellow.

of the occurrence of skipping or overlapping of planes.

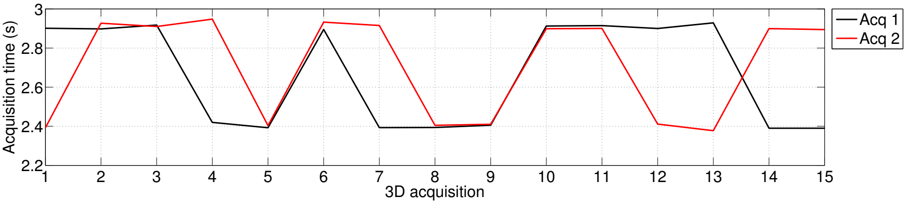

Figure E.3: Example of acquisition time for the 3D US acquisition of two different phantoms. Each phantom was scanned 15 times.

Bibliography

[1] S. Abellaneda, N. Guissard, and J. Duchateau. The relative lengthening of the myotendinous structures in the medial gastrocnemius during passive stretching differs among individuals. *Journal of applied physiology (Bethesda, Md. : 1985)*, 106(1):169–77, oct 2009.

[2] J. E. Aldrich. Basic physics of ultrasound imaging. *Critical care medicine*, 35(5 Suppl):S131–S137, may 2007.

[3] R. M. Alexander. Energy-saving mechanisms in walking and running. *The Journal of experimental biology*, 160(1):55–69, 1991.

[4] R. M. Alexander and H. C. Bennet-Clark. Storage of elastic strain energy in muscle and other tissues. *Nature*, 265(5590):114–117, jan 1977.

[5] M. Ali and R. Parlapalli. Signal processing overview of optical coherence tomography systems for medical imaging. *Texas Instruments, June*, (June):1–22, 2010.

[6] N. Almeida, P. Slagmolen, D. Barbosa, L. Scheys, L. Geukens, S. Fukagawa, K. Peers, J. Bellemans, P. Suetens, and J. D'hooge. Tendon strain imaging using non-rigid image registration: a validation study. In *Proceedings of the SPIE Medical Imaging 2012*, page 10p. SPIE-INT SOC OPTICAL ENGINEERING, apr 2012.

[7] B. H. Amundsen, T. Helle-Valle, T. Edvardsen, H. Torp, J. Crosby, E. Lyseggen, A. Støylen, H. Ihlen, J. A. C. Lima, O. A. Smiseth, and S. A. Slørdahl. Noninvasive myocardial strain measurement by speckle tracking echocardiography: validation against sonomicrometry and tagged magnetic resonance imaging. *Journal of the American College of Cardiology*, 47(4):789–93, feb 2006.

[8] A. Arampatzis, K. Karamanidis, and K. Albracht. Adaptational responses of the human Achilles tendon by modulation of the applied cyclic strain

magnitude. *The Journal of experimental biology*, 210(Pt 15):2743–2753, 2007.

[9] A. Arampatzis, S. Stafilidis, G. DeMonte, K. Karamanidis, G. Morey-Klapsing, and G. P. Brüggemann. Strain and elongation of the human gastrocnemius tendon and aponeurosis during maximal plantarflexion effort. *Journal of Biomechanics*, 38(4):833–41, apr 2005.

[10] J. M. Archambault, J. P. Wiley, R. C. Bray, M. Verhoef, D. A. Wiseman, and P. D. Elliott. Can sonography predict the outcome in patients with achillodynia? *Journal of Clinical Ultrasound*, 26(7):335–339, sep 1998.

[11] W. F. Armstrong and T. Ryan. *Feigenbaum's Echocardiography.* Wolters Kluwer Health/Lippincott Williams & Wilkins, 2012.

[12] A. Arndt, A. S. Bengtsson, M. Peolsson, A. Thorstensson, and T. Movin. Non-uniform displacement within the Achilles tendon during passive ankle joint motion. *Knee Surgery, Sports Traumatology, Arthroscopy*, 20(9):1868–1874, sep 2012.

[13] A. N. Arndt, P. V. Komi, G. P. Brüggemann, and J. Lukkariniemi. Individual muscle contributions to the in vivo achilles tendon force. *Clinical Biomechanics*, 13(7):532–541, oct 1998.

[14] S. P. Arnoczky, M. Lavagnino, and M. Egerbacher. The mechanobiological aetiopathogenesis of tendinopathy: is it the over-stimulation or the under-stimulation of tendon cells? *International Journal of Experimental Pathology*, 88(4):217–226, aug 2007.

[15] S. P. Arnoczky, M. Lavagnino, J. H. Whallon, and A. Hoonjan. In situ cell nucleus deformation in tendons under tensile load; a morphological analysis using confocal laser microscopy. *Journal of Orthopaedic Research*, 20(1):29–35, jan 2002.

[16] S. Arya and K. Kulig. Tendinopathy alters mechanical and material properties of the Achilles tendon. *Journal of Applied Physiology*, 108(3):670–5, mar 2010.

[17] J. Ashburner, J. Ashburner, K. J. Friston, and K. J. Friston. Nonlinear Spatial Normalizatioon Using Basis Functions. *Human Brain Mapping*, 7:254–266, 1999.

[18] S. Aubry, J.-P. Nueffer, M. Tanter, F. Becce, C. Vidal, and F. Michel. Viscoelasticity in Achilles tendonopathy: quantitative assessment by using real-time shear-wave elastography. *Radiology*, 274(3):821–9, mar 2015.

[19] S. Aubry, J.-R. Risson, A. Kastler, B. Barbier-Brion, G. Siliman, M. Runge, and B. Kastler. Biomechanical properties of the calcaneal tendon in vivo assessed by transient shear wave elastography. *Skeletal radiology*, 42(8):1143–50, aug 2013.

[20] M. B. Bennett, R. F. Ker, N. J. Imery, and R. M. Alexander. Mechanical properties of various mammalian tendons. *Journal of Zoology*, 209(4):537–548, aug 1986.

[21] J. Bercoff, M. Tanter, and M. Fink. Supersonic shear imaging: A new technique for soft tissue elasticity mapping. *IEEE Transactions on Ultrasonics, Ferroelectrics, and Frequency Control*, 51(4):396–409, 2004.

[22] J. M. Blackall, D. Rueckert, C. R. Maurer, G. P. Penney, D. L. G. Hill, and D. J. Hawkes. An Image Registration Approach to Automated Calibration for Freehand 3D Ultrasound. In *Medical Image Computing and Computer-Assisted Intervention*, pages 462–471. Springer, Berlin, Heidelberg, 2000.

[23] J. Bojsen-Møller, P. Hansen, P. Aagaard, U. Svantesson, M. Kjaer, S. Peter Magnusson, and U. Svant-esson. Differential displacement of the human soleus and medial gastrocnemius aponeuroses during isometric plantar flexor contractions in vivo. *J Appl Physiol*, 97(5):1908–1914, nov 2004.

[24] J. Bojsen-Møller and S. P. Magnusson. Heterogeneous loading of the human Achilles tendon in vivo, oct 2015.

[25] F. L. Bookstein. Principal Warps: Thin-Plate Splines and the Decomposition of Deformations. *IEEE Transactions on Pattern Analysis and Machine Intelligence*, 11(6):567–585, jun 1989.

[26] P. G. Brown, J. Alsousou, A. Cooper, M. S. Thompson, and J. A. Noble. The AutoQual ultrasound elastography method for quantitative assessment of lateral strain in post-rupture Achilles tendons. *Journal of Biomechanics*, 46(15):2695–700, oct 2013.

[27] C. B. Burckhardt. Speckle in Ultrasound B -Mode Scans. *IEEE Transactions on Sonics and Ultrasonics*, SU-25(1):1–6, 1978.

[28] T. J. Burkholder, B. Fingado, S. Baron, and R. L. Lieber. Relationship between muscle fiber types and sizes and muscle architectural properties in the mouse hindlimb. *Journal of Morphology*, 221(2):177–190, aug 1994.

[29] D. L. Butler, E. S. Grood, F. R. Noyes, and R. F. Zernicke. Biomechanics of ligaments and tendons. *Exercise and sport sciences reviews*, 6(October):125–181, 1978.

[30] R. H. Byrd, P. Lu, J. Nocedal, and C. Zhu. A Limited Memory Algorithm for Bound Constrained Optimization. *SIAM Journal on Scientific Computing*, 16(5):1190–1208, sep 1995.

[31] A. Chang and T. T. Miller. Imaging of tendons. *Sports health*, 1(4):293–300, jul 2009.

[32] L. Chen, G. M. Treece, J. E. Lindop, A. H. Gee, and R. W. Prager. A quality-guided displacement tracking algorithm for ultrasonic elasticity imaging. *Medical image analysis*, 13(2):286–96, apr 2009.

[33] V. W. T. Cheng and H. R. C. Screen. The micro-structural strain response of tendon. *Journal of Materials Science*, 42:8957–8965, 2007.

[34] L. A. Chernak and D. G. Thelen. Tendon motion and strain patterns evaluated with two-dimensional ultrasound elastography. *Journal of Biomechanics*, 45(15):2618–2623, oct 2012.

[35] L. Chernak Slane and D. G. Thelen. The use of 2D ultrasound elastography for measuring tendon motion and strain. *Journal of Biomechanics*, 47(3):750–4, feb 2014.

[36] R. Chhem and E. Cardinal. *Guidelines and gamuts in musculoskeletal ultrasound.* Wiley-Liss, 1999.

[37] S. Child, A. L. Bryant, R. A. Clark, and K. M. Crossley. Mechanical properties of the achilles tendon aponeurosis are altered in athletes with achilles tendinopathy. *The American journal of sports medicine*, 38(9):1885–93, sep 2010.

[38] R. L. Chimenti, M. Bucklin, M. Kelly, J. Ketz, A. S. Flemister, M. S. Richards, and M. R. Buckley. Insertional achilles tendinopathy associated with altered transverse compressive and axial tensile strain during ankle dorsiflexion, jun 2016.

[39] D. V. Cicchetti. Guidelines, criteria, and rules of thumb for evaluating normed and standardized assessment instruments in psychology. *Psychological Assessment*, 6(4):284–290, 1994.

[40] C. A. Coen. Seeking the comparative advantage: The dynamics of individual cooperation in single vs. multiple-team environments. *Organizational Behavior and Human Decision Processes*, 100(2):145–159, jul 2006.

[41] R. E. Cohen, C. J. Hooley, and N. G. McCrum. Viscoelastic creep of collagenous tissue. *Journal of Biomechanics*, 9(4):175–184, jan 1976.

[42] J. Cook, K. Khan, and C. Purdam. Achilles tendinopathy. *Manual Therapy*, 7(3):121–130, nov 2002.

[43] J. L. Cook and C. R. Purdam. Is tendon pathology a continuum? A pathology model to explain the clinical presentation of load-induced tendinopathy. *British journal of sports medicine*, 43(6):409–416, jun 2009.

[44] T. F. Cootes, T. F. Cootes, S. Marsland, S. Marsland, C. J. Twining, C. J. Twining, K. Smith, K. Smith, C. J. Taylor, and C. J. Taylor. Groupwise Diffeomorphic Non-rigid Registration for Automatic Model Building. In *European Conference on Computer Vision*, pages 316–327, 2004.

[45] T. F. Cootes, C. J. Twining, V. Petrovic, R. Schestowitz, and C. J. Taylor. Groupwise construction of appearance models using piece-wise affine deformations. In *British Machine Vision Conference*, number Mdl, pages 879–888, 2005.

[46] N. J. Cronin, J. Avela, T. Finni, and J. Peltonen. Differences in contractile behaviour between the soleus and medial gastrocnemius muscles during human walking. *Journal of Experimental Biology*, 216(5):909–914, 2013.

[47] R. Csapo, V. Malis, J. Hodgson, and S. Sinha. Age-related greater Achilles tendon compliance is not associated with larger plantar flexor muscle fascicle strains in senior women. *Journal of Applied Physiology*, 116(8):961–969, 2014.

[48] W. G. Cuming, R. M. Alexander, and A. S. Jayes. Rebound resilience of tendons in the feet of sheep (Ovis aries). *The Journal of experimental biology*, 74(1):75–81, 1978.

[49] A. H. Curiale, G. Vegas-Sánchez-Ferrero, and S. Aja-Fernández. Influence of ultrasound speckle tracking strategies for motion and strain estimation. *Medical Image Analysis*, 32:184–200, aug 2016.

[50] Y.-H. Dai. A family of hybrid conjugate gradient methods for unconstrained optimization. *Mathematics of Computation*, 72(243):1317–1329, 2003.

[51] M. De Craene, G. Piella, O. Camara, N. Duchateau, E. Silva, A. Doltra, J. D'hooge, J. Brugada, M. Sitges, and A. F. Frangi. Temporal diffeomorphic free-form deformation: application to motion and strain estimation from 3D echocardiography. *Medical image analysis*, 16(2):427–50, feb 2012.

[52] S. de Jonge, C. van den Berg, R. J. de Vos, H. J. L. van der Heide, A. Weir, J. A. N. Verhaar, S. M. A. Bierma-Zeinstra, and J. L. Tol. Incidence

of midportion Achilles tendinopathy in the general population. *British Journal of Sports Medicine*, 45(13):1026–1028, oct 2011.

[53] G. De Monte, A. Arampatzis, C. Stogiannari, and K. Karamanidis. In vivo motion transmission in the inactive gastrocnemius medialis muscle-tendon unit during ankle and knee joint rotation. *Journal of electromyography and kinesiology : official journal of the International Society of Electrophysiological Kinesiology*, 16(5):413–22, oct 2006.

[54] M. N. Dean, E. Azizi, and A. P. Summers. Uniform strain in broad muscles: active and passive effects of the twisted tendon of the spotted ratfish Hydrolagus colliei. *The Journal of experimental biology*, 210(Pt 19):3395–406, 2007.

[55] D. F. W. G. Dfwg. the Nifti-1 Data Format. pages 1–4, 2004.

[56] T. C. Doehring, M. Kahelin, and I. Vesely. Direct measurement of nonuniform large deformations in soft tissues during uniaxial extension. *Journal of biomechanical engineering*, 131(6):061001, jun 2009.

[57] Y.-C. Du, Y.-F. Chen, C.-M. Li, C.-H. Lin, C.-E. Yang, J.-X. Wu, and T. Chen. Quantitative ultrasound method for assessing stress–strain properties and the cross-sectional area of Achilles tendon. *Measurement Science and Technology*, 24(12):125702, dec 2013.

[58] S. M. Dudea and C. Botar-Jid. Ultrasound elastography in thyroid disease, mar 2015.

[59] S. E. Duenwald, R. Vanderby, and R. S. Lakes. Viscoelastic relaxation and recovery of tendon. *Annals of biomedical engineering*, 37(6):1131–40, jun 2009.

[60] M. Edama, M. Kubo, H. Onishi, T. Takabayashi, T. Inai, E. Yokoyama, W. Hiroshi, N. Satoshi, and I. Kageyama. The twisted structure of the human Achilles tendon. *Scandinavian Journal of Medicine and Science in Sports*, 25(5):e497–e503, oct 2015.

[61] A. Elen, H. F. Choi, D. Loeckx, H. Gao, P. Claus, P. Suetens, F. Maes, and J. D'hooge. Three-dimensional cardiac strain estimation using spatio-temporal elastic registration of ultrasound images: a feasibility study. *IEEE transactions on medical imaging*, 27(11):1580–91, nov 2008.

[62] P. Eliasson, A. Fahlgren, B. Pasternak, and P. Aspenberg. Unloaded rat Achilles tendons continue to grow, but lose viscoelasticity. *J Appl Physiol*, 103:459–463, 2007.

[63] D. Elliott. Structure and function of mammalian tendon. *Biological Reviews*, 40(3):392–421, aug 1965.

[64] D. J. Farris, G. Trewartha, and M. P. McGuigan. The effects of a 30-min run on the mechanics of the human Achilles tendon. *European Journal of Applied Physiology*, 112(2):653–660, feb 2012.

[65] D. J. Farris, G. Trewartha, M. P. McGuigan, and G. a. Lichtwark. Differential strain patterns of the human Achilles tendon determined in vivo with freehand three-dimensional ultrasound imaging. *The Journal of experimental biology*, 216(Pt 4):594–600, feb 2013.

[66] D. J. Farris, G. Trewartha, and M. Polly McGuigan. Could intra-tendinous hyperthermia during running explain chronic injury of the human Achilles tendon? *Journal of Biomechanics*, 44(5):822–826, mar 2011.

[67] J. Farron, T. Varghese, and D. G. Thelen. Measurement of tendon strain during muscle twitch contractions using ultrasound elastography. *IEEE transactions on ultrasonics, ferroelectrics, and frequency control*, 56(1):27–35, jan 2009.

[68] J. Farron, T. Varghese, and D. G. Thelen. Measurement of tendon strain during muscle twitch contractions using ultrasound elastography. *IEEE transactions on ultrasonics, ferroelectrics, and frequency control*, 56(1):27–35, jan 2009.

[69] F. Fath, A. J. Blazevich, C. M. Waugh, S. C. Miller, T. Korff, K. An, K. Takahashi, T. Harrigan, E. Chao, R. Donatelli, T. Finni, P. Komi, J. Lukkariniemi, S. Fukashiro, P. Komi, M. Järvinen, M. Miyashita, T. Fukunaga, M. Ito, Y. Ichinose, S. Kuno, Y. Kawakami, S. Fukashiro, D. Grieve, S. Pheasant, P. Cavanagh, B. Hintermann, B. Nigg, C. Sommer, R. Isman, V. Inman, M. Ito, H. Akima, T. Fukunaga, A. Kay, A. Blazevich, P. Klein, S. Mattys, M. Rooze, S. Lee, G. Lewis, S. Piazza, S. Lee, S. Piazza, C. Maganaris, C. Maganaris, C. Maganaris, V. Baltzopoulos, A. Sargeant, C. Maganaris, V. Baltzopoulos, A. Sargeant, C. Maganaris, V. Baltzopoulos, D. Tsaopoulos, C. Maganaris, J. Paul, K. Manal, J. Cowder, T. Buchanan, W. Murray, S. Delp, T. Buchanan, M. Panjabi, V. Goel, S. Walter, M. Panjabi, C. Redl, M. Gfoehler, M. Pandy, F. Reuleaux, S. Rugg, R. Gregor, B. Mandelbaum, L. Chiu, C. Spoor, J. van Leeuwen, C. Meskers, A. Titulaer, A. Huson, A. Storace, B. Wolf, D. Winter, M. Xiao, and J. Higginson. Direct comparison of in vivo Achilles tendon moment arms obtained from ultrasound and MR scans. *Journal of applied physiology (Bethesda, Md. : 1985)*, 109(6):1644–52, dec 2010.

[70] F. Faul, E. Erdfelder, A. Buchner, and A.-G. Lang. Statistical power analyses using G*Power 3.1: tests for correlation and regression analyses. *Behavior research methods*, 41(4):1149–60, nov 2009.

[71] F. Faul, E. Erdfelder, A.-G. Lang, and A. Buchner. GPOWER: A general power analysis program. *Behavior Research Methods*, 39(2):175–191, may 2007.

[72] T. Finni, N. J. Cronin, D. Mayfield, G. A. Lichtwark, and A. G. Cresswell. Effects of muscle activation on shear between human soleus and gastrocnemius muscles, jan 2015.

[73] T. Finni, J. A. Hodgson, A. M. Lai, V. R. Edgerton, and S. Sinha. Nonuniform strain of human soleus aponeurosis-tendon complex during submaximal voluntary contractions in vivo. *Journal of applied physiology (Bethesda, Md. : 1985)*, 95(2):829–37, 2003.

[74] B. Fischer and J. Modersitzki. Ill-posed medicine—an introduction to image registration. *Inverse Problems*, 24(3):034008, 2008.

[75] J. R. Franz, L. C. Slane, K. Rasske, and D. G. Thelen. Non-uniform in vivo deformations of the human Achilles tendon during walking. *Gait and Posture*, 41(1):192–197, 2015.

[76] J. R. Franz and D. G. Thelen. Depth-dependent variations in Achilles tendon deformations with age are associated with reduced plantarflexor performance during walking. *Journal of applied physiology (Bethesda, Md. : 1985)*, 119(3):242–9, 2015.

[77] J. R. Franz and D. G. Thelen. Imaging and simulation of Achilles tendon dynamics: implications for walking performance in the elderly. *Journal of Biomechanics*, 49(9):1403–1410, 2016.

[78] P. Fratzl, K. Misof, I. Zizak, G. Rapp, H. Amenitsch, and S. Bernstorff. Fibrillar structure and mechanical properties of collagen. *Journal of structural biology*, 122(1-2):119–22, 1998.

[79] K. J. Friston, J. Ashburner, C. D. Frith, J. B. Poline, J. D. Heather, and R. S. J. Frackowiak. Spatial registration and normalization of images. *Human Brain Mapping*, 3(3):165–189, 1995.

[80] Å. Fröberg, A.-S. Cissé, M. Larsson, M. Mårtensson, M. Peolsson, T. Movin, and A. Arndt. Altered patterns of displacement within the Achilles tendon following surgical repair. *Knee Surgery, Sports Traumatology, Arthroscopy*, pages 1–9, dec 2016.

[81] Å. Fröberg, M. Mårtensson, M. Larsson, B. Janerot-Sjöberg, J. D'Hooge, and A. Arndt. High variability in strain estimation errors when using a commercial ultrasound speckle tracking algorithm on tendon tissue. *Acta radiologica (Stockholm, Sweden : 1987)*, jan 2016.

[82] A. Goshtasby. Transformation functions for image registration. *Image*, 2003.

[83] W. Grassi, E. Filippucci, and P. Busilacchi. Musculoskeletal ultrasound. *Best practice & research. Clinical rheumatology*, 18(6):813–26, dec 2004.

[84] R. I. Griffiths. Shortening of muscle fibres during stretch of the active cat medial gastrocnemius muscle: the role of tendon compliance. *The Journal of physiology*, 436(1):219–36, may 1991.

[85] G. G. Handsfield, J. M. Inouye, L. C. Slane, D. G. Thelen, G. W. Miller, and S. S. Blemker. A 3D model of the Achilles tendon to determine the mechanisms underlying nonuniform tendon displacements. *Journal of Biomechanics*, 51:17–25, 2016.

[86] G. G. Handsfield, L. C. Slane, and H. R. Screen. Nomenclature of the Tendon Hierarchy: An Overview of Inconsistent Terminology and a Proposed Size-Based Naming Scheme with Terminology for Multi-Muscle Tendons, 2016.

[87] A. Hanley and J. McNeil. The Meaning and Use of the Area under a Receiver Operating Characteristic (ROC) Curve. *Radiology*, 143(1):29–36, apr 1982.

[88] N. Hansen and A. Ostermeier. Completely Derandomized Self-Adaptation in Evolution Strategies. *Evolutionary Computation*, 9(2):159–195, 2001.

[89] N. Hansen and A. Ostermeier. Completely Derandomized Self-Adaptation in Evolution Strategies. *Evolutionary Computation*, 9(2):159–195, 2001.

[90] D. Hawkins, C. Lum, D. Gaydos, and R. Dunning. Dynamic creep and pre-conditioning of the Achilles tendon in-vivo. *Journal of Biomechanics*, 42(16):2813–2817, 2009.

[91] G. W. Hess. Achilles tendon rupture: a review of etiology, population, anatomy, risk factors, and injury prevention. *Foot & ankle specialist*, 3(1):29–32, 2010.

[92] E. Hestenes M.R.and Stiefel. Method of conjugate gradients for solving linear systems. *J. Res. Nat. Bur. Standarts*, 49(6):409–436, 1952.

[93] B. Heyde. *Non-rigid image registration for the assessment of myocardial deformation from 3D echocardiography.* PhD thesis, KU Leuven, 2013.

[94] B. Heyde, S. Bouchez, S. Thieren, M. Vandenheuvel, R. Jasaityte, D. Barbosa, P. Claus, F. Maes, P. Wouters, and J. D'Hooge. Elastic image registration to quantify 3-D regional myocardial deformation from volumetric ultrasound: experimental validation in an animal model. *Ultrasound in medicine & biology*, 39(9):1688–97, sep 2013.

[95] B. Heyde, R. Jasaityte, D. Barbosa, V. Robesyn, S. Bouchez, P. Wouters, F. Maes, P. Claus, and J. D'hooge. Elastic image registration versus speckle tracking for 2-D myocardial motion estimation: a direct comparison in vivo. *IEEE transactions on medical imaging*, 32(2):449–59, feb 2013.

[96] D. L. Hill, P. G. Batchelor, M. Holden, and D. J. Hawkes. Medical image registration. *Physics in Medicine and Biology*, 46(3):R1–R45, mar 2001.

[97] C. J. Hooley, N. G. McCrum, and R. E. Cohen. The viscoelastic deformation of tendon. *Journal of Biomechanics*, 13(6):521–528, 1980.

[98] W. Huizinga, D. H. J. Poot, J. M. Guyader, H. Smit, M. Van Kranenburg, R. J. M. Van Geuns, A. Uitterdijk, H. M. M. Van Beusekom, B. F. Coolen, A. Leemans, W. J. Niessen, and S. Klein. Non-rigid groupwise image registration for motion compensation in quantitative MRI. In *Lecture Notes in Computer Science (including subseries Lecture Notes in Artificial Intelligence and Lecture Notes in Bioinformatics)*, volume 8545 LNCS, pages 184–193, 2014.

[99] M. Ishikawa, P. V. Komi, M. J. Grey, V. Lepola, and G.-P. Bruggemann. Muscle-tendon interaction and elastic energy usage in human walking. *Journal of applied physiology (Bethesda, Md. : 1985)*, 99(2):603–608, aug 2005.

[100] S. Iwanuma, R. Akagi, T. Kurihara, S. Ikegawa, H. Kanehisa, T. Fukunaga, and Y. Kawakami. Longitudinal and transverse deformation of human Achilles tendon induced by isometric plantar flexion at different intensities. *Journal of Applied Physiology*, 110(6):1615–1621, jun 2011.

[101] J. J. E. Dennis and J. J. Moré. Quasi-newton methods, motivation and theory*. *SIAM Review*, 19(1):46–89, 1977.

[102] B. Jahne, H. Haustecker, and P. Geistler. *Handbook of Computer Vision and Applications Volume 2: Signal Processing and Pattern Recognition.* Academic Press, 1999.

[103] T. A. H. Järvinen, P. Kannus, N. Maffulli, and K. M. Khan. Achilles tendon disorders: etiology and epidemiology. *Foot and ankle clinics*, 10(2):255–66, jul 2005.

[104] J. A. Jensen. FIELD: A Program for Simulating Ultrasound Systems. In *10th Nordic-Baltic Conference on Biomedical Imaging Published in Medical & Biological Engineering & Computing*, pages 351–353, 1996.

[105] J. A. Jensen and N. B. Svendsen. Calculation of pressure fields from arbitrarily shaped, apodized, and excited ultrasound transducers. *IEEE transactions on ultrasonics, ferroelectrics, and frequency control*, 39(2):262–7, jan 1992.

[106] S. Jeong, D. Y. Lee, D. S. Choi, and H. D. Lee. Acute effect of heel-drop exercise with varying ranges of motion on the gastrocnemius aponeurosis-tendon's mechanical properties. *Journal of Electromyography and Kinesiology*, 24(3):375–379, 2014.

[107] F. E. Johannsen and A. N. Gam. [Achillodynia is not just a sports injury]. *Ugeskrift for laeger*, 172(48):3325–9, nov 2010.

[108] M. A. Johnson, J. Polgar, D. Weightman, and D. Appleton. Data on the distribution of fibre types in thirty-six human muscles. An autopsy study. *Journal of the Neurological Sciences*, 18(1):111–129, jan 1973.

[109] H. Jonely, D. J. Jayaseelan, and M. Rieke. Tendinopathy and Aging A Review of Literature and Considerations for Older Adult Athletes. *Topics in geriatric rehabilitation*, 32(1):E1–E12, 2016.

[110] L. Józsa, M. Lehto, M. Kvist, J. B. Bálint, and A. Reffy. Alterations in dry mass content of collagen fibers in degenerative tendinopathy and tendon-rupture. *Matrix*, 9(2):140–6, mar 1989.

[111] L. G. Józsa and P. Kannus. *Human Tendons: Anatomy, Physiology, and Pathology*. Human Kinetics Publishers, 1 edition edition, 1997.

[112] C. J. F. Kahn, X. Wang, and R. Rahouadj. Nonlinear model for viscoelastic behavior of Achilles tendon. *Journal of biomechanical engineering*, 132(11):111002, nov 2010.

[113] J. Kastelic, A. Galeski, and E. Baer. The multicomposite structure of tendon. *Connective tissue research*, 6(1):11–23, jan 1978.

[114] Y. Kawakami, Y. Ichinose, and T. Fukunaga. Architectural and functional features of human triceps surae muscles during contraction. *Journal of applied physiology (Bethesda, Md. : 1985)*, 85(2):398–404, aug 1998.

[115] Y. Kawakami, H. Kanehisa, and T. Fukunaga. The Relationship Between Passive Ankle Plantar Flexion Joint Torque and Gastrocnemius Muscle and Achilles Tendon Stiffness: Implications for Flexibility. *The Journal of orthopaedic and sports physical therapy*, 38(5):269–76, may 2008.

[116] R. F. KER, R. M. ALEXANDER, and M. B. BENNETT. Why are mammalian tendons so thick? *Journal of Zoology*, 216(2):309–324, 1988.

[117] K. M. Khan, J. L. Cook, F. Bonar, P. Harcourt, and M. Åstrom. Histopathology of common tendinopathies: Update and implications for clinical management. *Sports Medicine*, 27(6):393–408, jun 1999.

[118] K. M. Khan and N. Maffulli. Tendinopathy: an Achilles' heel for athletes and clinicians., jul 1998.

[119] S. Klein and M. Staring. Elastix 4.7 - Manual. page 62, 2014.

[120] S. Klein, M. Staring, K. Murphy, M. A. Viergever, and J. P. W. Pluim. elastix: a toolbox for intensity-based medical image registration. *IEEE transactions on medical imaging*, 29(1):196–205, jan 2010.

[121] S. Klein, M. Staring, and J. P. W. Pluim. Evaluation of optimization methods for nonrigid medical image registration using mutual information and B-splines. *IEEE Trans. Image Process.*, 16(12):2879–2890, 2007.

[122] P. V. Komi. Relevance of in vivo force measurements to human biomechanics. *Journal of Biomechanics*, 23(SUPPL. 1):23–34, 1990.

[123] M. Kongsgaard, C. H. Nielsen, S. Hegnsvad, P. Aagaard, and S. P. Magnusson. Mechanical properties of the human Achilles tendon, in vivo. *Clinical biomechanics (Bristol, Avon)*, 26(7):772–7, aug 2011.

[124] E. Konofagou and J. Ophir. A new elastographic method for estimation and imaging of lateral displacements, lateral strains, corrected axial strains and Poisson's ratios in tissues. *Ultrasound in Medicine and Biology*, 24(8):1183–1199, oct 1998.

[125] J.-W. H. Korstanje, R. W. Selles, H. J. Stam, S. E. R. Hovius, and J. G. Bosch. Development and validation of ultrasound speckle tracking to quantify tendon displacement. *Journal of Biomechanics*, 43(7):1373–9, may 2010.

[126] J. F. Krücker, G. L. LeCarpentier, J. B. Fowlkes, and P. L. Carson. Rapid elastic image registration for 3-D ultrasound, nov 2002.

[127] K. Kubo, M. Morimoto, T. Komuro, N. Tsunoda, H. Kanehisa, and T. Fukunaga. Age-related differences in the properties of the plantar flexor muscles and tendons. *Medicine and Science in Sports and Exercise*, 39(3):541–547, mar 2007.

[128] U. M. Kujala, S. Sarna, and J. Kaprio. Cumulative incidence of achilles tendon rupture and tendinopathy in male former elite athletes. *Clinical journal of sport medicine : official journal of the Canadian Academy of Sport Medicine*, 15(3):133–135, may 2005.

[129] H. Langberg, D. Skovgaard, L. J. Petersen, J. Bulow, and M. Kjaer. Type I collagen synthesis and degradation in peritendinous tissue after exercise determined by microdialysis in humans. *The Journal of physiology*, 521 Pt 1(Pt 3):299–306, nov 1999.

[130] M. Larsson, F. Kremer, P. Claus, T. Kuznetsova, L. A. Brodin, and J. D'Hooge. Ultrasound-based radial and longitudinal strain estimation of the carotid artery: A feasibility study. *IEEE Transactions on Ultrasonics, Ferroelectrics, and Frequency Control*, 58(10):2244–2251, oct 2011.

[131] M. Laurie. On the Morphology of the Pedipalpi. *Journal of the Linnean Society of London, Zoology*, 25(158):20–48, jul 1894.

[132] M. Laurie. On the Morphology of the Pedipalpi. *Journal of the Linnean Society of London, Zoology*, 25(158):20–48, jul 1894.

[133] J. P. Lawrence. Physics and instrumentation of ultrasound. *Critical care medicine*, 35(8 Suppl):S314–S322, aug 2007.

[134] H.-D. Lee, T. Finni, J. A. Hodgson, A. M. Lai, V. R. Edgerton, and S. Sinha. Soleus aponeurosis strain distribution following chronic unloading in humans: an in vivo MR phase-contrast study. *Journal of applied physiology (Bethesda, Md. : 1985)*, 100(6):2004–2011, jan 2006.

[135] S. Lee, G. Wolberg, and S. Y. Shin. Scattered data interpolation with multilevel b-splines. *IEEE Transactions on Visualization and Computer Graphics*, 3(3):228–244, 1997.

[136] R. L. Lenhart, C. A. Francis, A. L. Lenz, and D. G. Thelen. Empirical evaluation of gastrocnemius and soleus function during walking. *Journal of Biomechanics*, 47(12):2969–2974, sep 2014.

[137] C. Lersch, A. Grötsch, B. Segesser, J. Koebke, G.-P. Brüggemann, and W. Potthast. Influence of calcaneus angle and muscle forces on strain distribution in the human Achilles tendon. *Clinical biomechanics (Bristol, Avon)*, 27(9):955–61, nov 2012.

[138] J. Lewis. Fast Normalized Cross-Correlation, Vision Interface. *Industrial Light & Magic*, 1995.

[139] T. Liang, L. Yung, and W. Yu. On feature motion decorrelation in ultrasound speckle tracking. *IEEE Transactions on Medical Imaging*, 32(2):435–448, feb 2013.

[140] G. A. Lichtwark, A. G. Cresswell, and R. J. Newsham-West. Effects of running on human Achilles tendon length-tension properties in the free and gastrocnemius components. *The Journal of experimental biology*, 216(Pt 23):4388–94, 2013.

[141] G. A. Lichtwark and A. M. Wilson. In vivo mechanical properties of the human Achilles tendon during one-legged hopping. *The Journal of experimental biology*, 208(Pt 24):4715–4725, dec 2005.

[142] G. A. Lichtwark and A. M. Wilson. Interactions between the human gastrocnemius muscle and the Achilles tendon during incline, level and decline locomotion. *The Journal of experimental biology*, 209(21):4379–4388, 2006.

[143] M. J. Lindstrom and D. M. Bates. Newton — Raphson and EM Algorithms for Linear Mixed- Newton-Raphson and E M Algorithms for Linear Mixed-Effects Models for Repeated-Measures Data. *Journal of the American Statistical Association*, 83(404):1014–1022, dec 1988.

[144] R. G. P. Lopata, M. M. Nillesen, J. M. Thijssen, L. Kapusta, and C. L. de Korte. Three-dimensional cardiac strain imaging in healthy children using RF-data. *Ultrasound in medicine & biology*, 37(9):1399–408, sep 2011.

[145] M. A. Lubinski, S. Y. Emelianov, and M. O'Donnell. Speckle tracking methods for ultrasonic elasticity imaging using short-time correlation. *IEEE transactions on ultrasonics, ferroelectrics, and frequency control*, 46(1):82–96, jan 1999.

[146] J. Lyman. Strain Behavior of the Distal Achilles Tendon: Implications for Insertional Achilles Tendinopathy. *American Journal of Sports Medicine*, 32(2):457–461, mar 2004.

[147] J. Lysholm and J. Wiklander. Injuries in runners. *The American Journal of Sports Medicine*, 15(2):168–171, mar 1987.

[148] B. Ma, R. Narayanan, H. Park, A. O. Hero, P. H. Bland, and C. R. Meyer. Comparing pairwise and simultaneous joint registrations of decorrelating interval exams using entropic graphs. *Inf Process Med Imaging*, 20:270–282, 2007.

[149] D. Maffulli, Nicola; Kader. Tendinopathy of tendo Achillis. *The Journal of bone and joint surgery. British volume*, 84-B(1):1–8, 2003.

[150] C. N. Maganaris. Tendon conditioning: artefact or property? *Proceedings of the Royal Society of London: Biological Sciences*, 270 Suppl:S39–S42, 2003.

[151] C. N. Maganaris, V. Baltzopoulos, and A. J. Sargeant. Repeated contractions alter the geometry of human skeletal muscle. *Journal of applied physiology (Bethesda, Md. : 1985)*, 93(6):2089–2094, 2002.

[152] C. N. Maganaris, M. V. Narici, and N. Maffulli. Biomechanics of the Achilles tendon. *Disability and rehabilitation*, 30(20-22):1542–7, jan 2008.

[153] C. N. Maganaris and J. P. Paul. In vivo human tendon mechanical properties. *J Physiol*, 521 Pt 1(1):307–13, nov 1999.

[154] S. P. Magnusson, P. Aagaard, P. Dyhre-Poulsen, and M. Kjaer. Load-displacement properties of the human triceps surae aponeurosis in vivo. *The Journal of physiology*, 531(Pt 1):277–88, mar 2001.

[155] S. P. Magnusson, P. Hansen, P. Aagaard, J. Brønd, P. Dyhre-Poulsen, J. Bojsen-Moller, and M. Kjaer. Differential strain patterns of the human gastrocnemius aponeurosis and free tendon, in vivo. *Acta Physiologica Scandinavica*, 177(2):185–195, feb 2003.

[156] A. Manbachi and R. S. C. Cobbold. Development and application of piezoelectric materials for ultrasound generation and detection. *Ultrasound*, 19(4):187–196, nov 2011.

[157] L. S. Matthews and D. Ellis. Viscoelastic properties of cat tendon: Effects of time after death and preservation by freezing. *Journal of Biomechanics*, 1(2):65–71, jul 1968.

[158] R. L. McGough, R. E. Debski, E. Taskiran, F. H. Fu, and S. L. Woo. Mechanical properties of the long head of the biceps tendon. *Knee surgery, sports traumatology, arthroscopy : official journal of the ESSKA*, 3(4):226–9, 1996.

[159] B. F. Miller, J. L. Olesen, M. Hansen, S. Døssing, R. M. Crameri, R. J. Welling, H. Langberg, A. Flyvbjerg, M. Kjaer, J. A. Babraj, K. Smith, and M. J. Rennie. Coordinated collagen and muscle protein synthesis in human patella tendon and quadriceps muscle after exercise. *J Physiol*, 567(3):1021–1033, sep 2005.

[160] E. Mosler, W. Folkhard, E. Knörzer, H. Nemetschek-Gansler, T. Nemetschek, and M. H. J. Koch. Stress-induced molecular rearrangement in tendon collagen. *Journal of Molecular Biology*, 182(4):589–596, apr 1985.

[161] T. Muramatsu, T. Muraoka, D. Takeshita, Y. Kawakami, Y. Hirano, and T. Fukunaga. Mechanical properties of tendon and aponeurosis of human gastrocnemius muscle in vivo. *Journal of applied physiology (Bethesda, Md. : 1985)*, 90(5):1671–1678, may 2001.

[162] M. V. Narici, N. Maffulli, and C. N. Maganaris. Ageing of human muscles and tendons. *Disability and rehabilitation*, 30(20-22):1548–1554, jan 2008.

[163] S. Nocedal, Jorge, Wright. *Numerical Optimization.* Number 1. Springer-Verlag New York, Inc., New York, 1999.

[164] S. J. Obst, R. Newsham-West, and R. S. Barrett. In vivo measurement of human achilles tendon morphology using freehand 3-D ultrasound. *Ultrasound in medicine & biology*, 40(1):62–70, jan 2014.

[165] S. J. Obst, J.-B. Renault, R. Newsham-West, and R. S. Barrett. Three-dimensional deformation and transverse rotation of the human free Achilles tendon in vivo during isometric plantarflexion contraction. *Journal of applied physiology (Bethesda, Md. : 1985)*, 116(4):376–84, feb 2014.

[166] G. Okotie, S. Duenwald-Kuehl, H. Kobayashi, M.-J. Wu, and R. Vanderby. Tendon strain measurements with dynamic ultrasound images: evaluation of digital image correlation. *Journal of biomechanical engineering*, 134(2):024504, feb 2012.

[167] L. Oliveira, C. Peixinho, G. Silva, and L. Menegaldo. In vivo passive mechanical properties estimation of Achilles tendon using ultrasound. *Journal of Biomechanics*, nov 2015.

[168] C. C. Ooi, P. Malliaras, M. E. Schneider, and D. a. Connell. "Soft, hard, or just right?" Applications and limitations of axial-strain sonoelastography and shear-wave elastography in the assessment of tendon injuries. *Skeletal radiology*, 43(1):1–12, jan 2014.

[169] C. C. Ooi, M. E. Schneider, P. Malliaras, M. Chadwick, and D. A. Connell. Diagnostic performance of axial-strain sonoelastography in confirming clinically diagnosed Achilles tendinopathy: comparison with B-mode ultrasound and color Doppler imaging. *Ultrasound in medicine & biology*, 41(1):15–25, jan 2015.

[170] J. Ophir. Elastography: A quantitative method for imaging the elasticity of biological tissues. *Ultrasonic Imaging*, 13(2):111–134, apr 1991.

[171] J. P. R. O. Orgel, T. C. Irving, A. Miller, and T. J. Wess. Microfibrillar structure of type I collagen in situ. *Proceedings of the National Academy of Sciences of the United States of America*, 103(24):9001, jun 2006.

[172] C. Otto and A. Pearlman. *Textbook of Clinical Echocardiography.* Elsevier/Saunders, 1995.

[173] D. S. P Magnusson, H. Langberg, M. Kjaer, S. Peter Magnusson, H. Langberg, and M. Kjaer. The pathogenesis of tendinopathy: balancing the response to loading. *Nature Publishing Group*, 6(10):262–26843, may 2010.

[174] D. Y. Park, J. Rubenson, A. Carr, J. Mattson, T. Besier, and L. B. Chou. Influence of stretching and warm-up on Achilles tendon material properties. *Foot & ankle international / American Orthopaedic Foot and Ankle Society [and] Swiss Foot and Ankle Society*, 32(4):407–413, apr 2011.

[175] F. R. Partington and G. C. Wood. The role of non-collagen components in the mechanical behaviour of tendon fibres. *Biochimica et biophysica acta*, 69:485–495, 1963.

[176] S. J. Pearson, T. Ritchings, and A. S. A. Mohamed. The use of normalized cross-correlation analysis for automatic tendon excursion measurement in dynamic ultrasound imaging. *Journal of Applied Biomechanics*, 29(2):165–173, apr 2013.

[177] J. Peltonen, N. J. Cronin, L. Stenroth, T. Finni, and J. Avela. Viscoelastic properties of the Achilles tendon in vivo. *SpringerPlus*, 2(1):212, dec 2013.

[178] G. Piella, M. De Craene, C. Butakoff, V. Grau, C. Yao, S. Nedjati-Gilani, G. P. Penney, and A. F. Frangi. Multiview diffeomorphic registration: application to motion and strain estimation from 3D echocardiography. *Medical image analysis*, 17(3):348–64, apr 2013.

[179] C. Podilchuk, M. Bajor, W. Stoddart, L. Barinov, W. Hulbert, A. Jairaj, and R. Mammone. Speckle reduction using stepped-frequency continuous wave ultrasound. In *2012 IEEE Signal Processing in Medicine and Biology Symposium (SPMB)*, pages 1–4. IEEE, dec 2012.

[180] C. M. Pollock and R. E. Shadwick. Relationship between body mass and biomechanical properties of limb tendons in adult mammals. *The American journal of physiology*, 266(3 Pt 2):R1016–R1021, mar 1994.

[181] P. P. Purslow, T. J. Wess, and D. W. Hukins. Collagen orientation and molecular spacing during creep and stress-relaxation in soft connective tissues. *The Journal of experimental biology*, 201(Pt 1):135–42, jan 1998.

[182] T. Raykov and G. A. Marcoulides. *Introduction to psychometric theory*. Routledge, 2011.

[183] J. D. Rees, A. M. Wilson, and R. L. Wolman. Current concepts in the management of tendon disorders. *Rheumatology*, 45(5):508–21, may 2006.

[184] J. Revell, M. Mirmehdi, and D. McNally. Computer vision elastography: speckle adaptive motion estimation for elastography using ultrasound sequences. *IEEE transactions on medical imaging*, 24(6):755–66, jun 2005.

[185] D. J. Riemersma and H. C. Schamhardt. In vitro mechanical properties of equine tendons in relation to cross-sectional area and collagen content. *Research in veterinary science*, 39(3):263–270, nov 1985.

[186] J. M. Robinson, J. L. Cook, C. Purdam, P. J. Visentini, J. Ross, N. Maffulli, J. E. Taunton, and K. M. Khan. The VISA-A questionnaire: a valid and reliable index of the clinical severity of Achilles tendinopathy. *British journal of sports medicine*, 35(5):335–41, oct 2001.

[187] D. Rueckert, L. I. Sonoda, C. Hayes, D. L. Hill, M. O. Leach, and D. J. Hawkes. Nonrigid registration using free-form deformations: application to breast MR images. *IEEE Transactions on Medical Imaging*, 18(8):712–21, aug 1999.

[188] R. D. Sacks and R. R. Roy. Architecture of the hind limb muscles of cats: Functional significance. *Journal of Morphology*, 173(2):185–195, aug 1982.

[189] B. Saltin and P. Gollnick. Skeletal muscle adaptability: significance for metabolism and performance. *Handbook of Physiology - Skeletal muscle*, (176):555–631, jan 1983.

[190] K. Sasaki and R. R. Neptune. Muscle mechanical work and elastic energy utilization during walking and running near the preferred gait transition speed. *Gait and Posture*, 23(3):383–390, 2006.

[191] H. R. C. Screen, D. L. Bader, D. A. Lee, and J. C. Shelton. Local strain measurement within tendon. *Strain*, 40(4):157–163, nov 2004.

[192] R. E. Shadwick. Elastic energy storage in tendons: mechanical differences related to function and age. *Journal of applied physiology (Bethesda, Md. : 1985)*, 68(3):1033–1040, mar 1990.

[193] D. P. Shamonin, E. E. Bron, B. P. F. Lelieveldt, M. Smits, S. Klein, and M. Staring. Fast parallel image registration on CPU and GPU for diagnostic classification of Alzheimer's disease. *Frontiers in neuroinformatics*, 7:50, jan 2013.

[194] S. Sinha and R. Kinugasa. Imaging Studies of the Mechanical and Architectural Characteristics of the Human Achilles Tendon in Normal, Unloaded and Rehabilitating Conditions. *Achilles Tendon*, pages 3–22, jan 2012.

[195] L. C. Slane, R. DeWall, J. Martin, K. Lee, and D. G. Thelen. Middle-aged adults exhibit altered spatial variations in Achilles tendon wave speed. *Physiological measurement*, 36(7):1485–96, jul 2015.

[196] L. C. Slane and D. G. Thelen. Non-uniform displacements within the Achilles tendon observed during passive and eccentric loading. *Journal of Biomechanics*, 47(12):2831–5, sep 2014.

[197] L. C. Slane and D. G. Thelen. Achilles tendon displacement patterns during passive stretch and eccentric loading are altered in middle-aged adults. *Medical Engineering and Physics*, 37(7):712–716, jul 2015.

[198] C. Smith, I. Young, and J. Kearney. Mechanical properties of tendons: changes with sterilization and preservation. *Journal of Biomechanical Engineering*, 118(1):56–61, feb 1996.

[199] A. Sotiras, C. Davatzikos, and N. Paragios. Deformable medical image registration: a survey. *IEEE transactions on medical imaging*, 32(7):1153–90, jul 2013.

[200] S. Srinivasan, T. Krouskop, and J. Ophir. Comparing elastographic strain images with modulus images obtained using nanoindentation: Preliminary results using phantoms and tissue samples. *Ultrasound in Medicine and Biology*, 30(3):329–343, 2004.

[201] S. Srinivasan and J. Ophir. A zero-crossing strain estimator for elastography. *Ultrasound in Medicine and Biology*, 29(2):227–238, jul 2003.

[202] M. E. Stadnick. MRI Web Clinic — January 2017 Achilles Tendon Pathology, 2008.

[203] S. Stafilidis and A. Arampatzis. Muscle - tendon unit mechanical and morphological properties and sprint performance. *Journal of sports sciences*, 25(9):1035–1046, jul 2007.

[204] K. J. Stegman, S. Djurickovic, and N. Dechev. InVivo Estimation of Flexor Digitorum Superficialis Tendon Displacement with Speckle Tracking on 2-D Ultrasound Images Using Laplacian, Gaussian and Rayleigh Techniques. *Ultrasound in Medicine and Biology*, 40(3):568–582, 2014.

[205] K. J. M. Surry, H. J. B. Austin, a. Fenster, and T. M. Peters. Poly(vinyl alcohol) cryogel phantoms for use in ultrasound and MR imaging. *Physics in Medicine and Biology*, 49(24):5529–5546, dec 2004.

[206] M. Sutton, W. Wolters, W. Peters, W. Ranson, and S. McNeill. Determination of displacements using an improved digital correlation method. *Image and Vision Computing*, 1(3):133–139, 1983.

[207] P. Szaro, G. Witkowski, R. Śmigielski, P. Krajewski, and B. Ciszek. Fascicles of the adult human Achilles tendon - An anatomical study. *Annals of Anatomy*, 191(6):586–593, nov 2009.

[208] S. E. Szczesny and D. M. Elliott. Interfibrillar shear stress is the loading mechanism of collagen fibrils in tendon. *Acta biomaterialia*, 10(6):2582–90, jun 2014.

[209] C. T. Thorpe, C. Klemt, G. P. Riley, H. L. Birch, P. D. Clegg, and H. R. C. Screen. Helical sub-structures in energy-storing tendons provide a possible mechanism for efficient energy storage and return. *Acta Biomaterialia*, 9(8):7948–7956, 2013.

[210] C. T. Thorpe, C. P. Udeze, H. L. Birch, P. D. Clegg, and H. R. C. Screen. Capacity for sliding between tendon fascicles decreases with ageing in injury prone equine tendons: A possible mechanism for age-related tendinopathy? *European Cells and Materials*, 25:48–60, jan 2012.

[211] C. T. Thorpe, C. P. Udeze, H. L. Birch, P. D. Clegg, and H. R. C. Screen. Specialization of tendon mechanical properties results from interfascicular differences. *Journal of The Royal Society Interface*, 9(July):3108–3117, 2012.

[212] M. Torriani and S. V. Kattapuram. Musculoskeletal ultrasound: an alternative imaging modality for sports-related injuries. *Topics in magnetic resonance imaging : TMRI*, 14(1):103–11, feb 2003.

[213] G. M. Treece, A. H. Gee, R. W. Prager, C. J. C. Cash, and L. H. Berman. High-definition freehand 3-D ultrasound. *Ultrasound in Medicine and Biology*, 29(4):529–546, 2003.

[214] W. Trochim, J. Donnelly, and K. Arora. *Research Methods: The Essential Knowledge Base.* Cengage Learning, 2015.

[215] M. Van Middelkoop, J. Kolkman, J. Van Ochten, S. M. A. Bierma-Zeinstra, and B. Koes. Prevalence and incidence of lower extremity injuries in male marathon runners. *Scandinavian journal of medicine & science in sports*, 18(2):140–4, apr 2008.

[216] H. T. M. van Schie, R. J. de Vos, S. de Jonge, E. M. Bakker, M. P. Heijboer, J. A. N. Verhaar, J. L. Tol, and H. Weinans. Ultrasonographic tissue characterisation of human Achilles tendons: quantification of tendon structure through a novel non-invasive approach. *British journal of sports medicine*, 44(16):1153–1159, 2010.

[217] T. Varghese, J. Ophir, and I. Céspedes. Noise reduction in elastograms using temporal stretching with multicompression averaging. *Ultrasound in Medicine and Biology*, 22(8):1043–1052, 1996.

[218] F. Viola, R. L. Coe, K. Owen, D. A. Guenther, and W. F. Walker. MUlti-Dimensional Spline-Based Estimator (MUSE) for Motion Estimation: Algorithm Development and Initial Results. *Annals of Biomedical Engineering*, 36(12):1942–1960, sep 2008.

[219] H. K. Wang, K. H. Lin, S. C. Su, T. T. F. Shih, and Y. C. Huang. Effects of tendon viscoelasticity in Achilles tendinosis on explosive performance and clinical severity in athletes. *Scandinavian Journal of Medicine and Science in Sports*, 22(6):e147–e155, dec 2012.

[220] X. T. Wang, R. F. Ker, and R. M. Alexander. Fatigue rupture of wallaby tail tendons. *The Journal of Experimental Biology*, 198(Pt 3):847–852, mar 1995.

[221] T. L. Wickiewicz, R. R. Roy, P. L. Powell, and V. R. Edgerton. Muscle architecture of the human lower limb. *Clinical orthopaedics and related research*, (179):275–83, 1983.

[222] S. L. Y. Woo. Mechanical properties of tendons and ligaments. I. Quasi-static and nonlinear viscoelastic properties. *Biorheology*, 19(3):385–396, 1982.

[223] R. P. Woods, S. T. Grafton, C. J. Holmes, S. R. Cherry, and J. C. Mazziotta. Automated image registration: I. General methods and intrasubject, intramodality validation. *Journal of computer assisted tomography*, 22(February 1998):139–152, 1998.

[224] R. P. Woods, S. T. Grafton, J. D. Watson, N. L. Sicotte, and J. C. Mazziotta. Automated image registration: Intersubject validation of linear and nonlinear models. *Journal of computer assisted tomography*, 22(1):153–165, 1998.

[225] T. a. Wren, S. a. Yerby, G. S. Beaupré, and D. R. Carter. Mechanical properties of the human achilles tendon. *Clinical biomechanics (Bristol, Avon)*, 16(3):245–51, mar 2001.

[226] E. K. Yen and R. G. Johnston. The Ineffectiveness of the Correlation Coefficient for Image Comparisons * The Ineffectiveness of the Correlation Coefficient for Image Comparisons. pages 1–14, 1996.

[227] F. Yeung, S. F. Levinson, D. Fu, and K. J. Parker. Feature-adaptive motion tracking of ultrasound image sequences using a deformable mesh. *IEEE transactions on medical imaging*, 17(6):945–956, dec 1998.

[228] F. Yeung, S. F. Levinson, and K. J. Parker. Multilevel and motion model-based ultrasonic speckle tracking algorithms. *Ultrasound in medicine & biology*, 24(3):427–41, mar 1998.

[229] F. E. Zajac. Muscle and tendon: properties, models, scaling, and application to biomechanics and motor control. *Critical reviews in biomedical engineering*, 17(4):359–411, 1989.

[230] B. Zitov and J. Flusser. Image registration methods: A survey, 2003.

List of publications

International Journal

Stijn Bogaerts, **C. de Brito Carvalho**, Lennart Scheys, Kaat Desloovere, Jan D'hooge, Frederik Maes, Paul Suetens, Koen Peers, *Evaluation of tissue displacement and regional strain in the Achilles tendon using quantitative high-frequency ultrasound*, Plos One, February 2017 (submitted) (joint-first authorship)

Catarina Carvalho, Pieter Slagmolen, Stijn Bogaerts, Lennart Scheys, Jan D'hooge, Koen Peers, Frederik Maes, Paul Suetens, *3D tendon strain estimation using high-frequency volumetric ultrasound images. A feasibility study.*, Ultrasonic Imaging , December 2016 (under-revision),

International Conference: published in proceedings

C. de Brito Carvalho, S. Bogaerts, L. Scheys, J. D'hooge, K. Peers, P. Suetens, *3D tendon strain estimation on high-frequency 3D ultrasound images. A simulation and phantom study*, 13th IEEE international symposium on biomedical imaging - ISBI 2016, April 13-16, 2016, Prague, Czech Republic

International Conference: abstract or not published

C. de Brito Carvalho, P. Slagmolen, J. D'hooge, L. Scheys, K. Peers, S. Bogaerts, P. Suetens, Interactive exploration of local strain on ultrasound images - A step closer towards clinical implementation, 21st congress of the

European Society of Biomechanics - ESB 2015, July 5-8, 2015, Prague, Czech Republic

C. de Brito Carvalho, S. Bogaerts, P. Slagmolen, J. D'hooge, L. Scheys, K. Peers, P. Suetens, *An interactive tool to estimate Achilles tendon local strain using high-frequency ultrasound: preliminary results*, Advances in tendon research: From bench to bedside, September 7-8, 2015, London, UK

International Conference: invited speaker

C. de Brito Carvalho, Image Registration For Speckle Tracking, Invited Speaker, Symposium: Tendon Mechanics And Ultrasound, *Ultrasound-Based Measurement Of Healthy And Pathological Tendon Mechanics*, June 16, 2016, Groot Begijnhof, Leuven, Belgium

FACULTY OF ENGINEERING SCIENCE
DEPARTMENT OF ELECTRICAL ENGINEERING
ESAT-PSI
Herestraat 49 box 7003, B-3000
B-3001 Leuven